Technische Universität München
Fakultät für Chemie

Fifth-Order Ultrafast Spectroscopy for Probing Non-Linear Exciton Dynamics and Spectral Fluctuations

Constantin Heshmatpour

Vollständiger Abdruck der von der Fakultät für Chemie der Technischen Universität München zur Erlangung des akademischen Grades eines

Doktors der Naturwissenschaften (Dr. rer. nat.)

genehmigten Dissertation.

Vorsitzender: Prof. Dr. Ulrich K. Heiz
Prüfer der Dissertation:

1. Prof. Dr. Jürgen Hauer
2. Prof. Dr. Maxim Gelin

Die Dissertation wurde am 25.04.2022 bei der Technischen Universität München eingereicht und durch die Fakultät für Chemie am 13.06.2022 angenommen.

Collected Works

The following scientific work was conducted from February 2019 until February 2022 at the Technical University Munich and the Charles University in Prague.

First-author Publications

1. C. Heshmatpour, J. Hauer, and F. Šanda. Interplay of exciton annihilation and transport in fifth order electronic spectroscopy. *Chem. Phys.*, 528:110433, 2020

2. C. Heshmatpour, P. Malevich, F. Plasser, M. Menger, C. Lambert, F. Šanda, and J. Hauer. Annihilation dynamics of molecular excitons measured at a single perturbative excitation energy. *J. Phys. Chem. Lett.*, 11(18):7776–7781, 2020

3. [‡] L. Wolz, C. Heshmatpour, A. Perri, D. Polli, G. Cerullo, J. J. Finley, E. Thyrhaug, J. Hauer, and A. V. Stier. Time-domain photocurrent spectroscopy based on a common-path birefringent interferometer. *Rev. Sci. Instrum.*, 91(12):123101, 2020

4. C. Heshmatpour, J. Hauer, and F. Šanda. Correlated spectral fluctuations quantified by line shape analysis of fifth-order two-dimensional electronic spectra. *J. Chem. Phys.*, 156(8):084114, 2022

Co-author Publications

1. P. Malevich, C. Heshmatpour, H. Ceymann, M. H. Schreck, and J. Hauer. Molecular annihilation dynamics measured in the perturbative regime of excitation. *The 22nd International Conference on Ultrafast Phenomena 2020*, page Th2A.2, 2020

[‡]L.W and C.H. contributed equally to this work.

Contributions to conferences and workshops

1. Poster (first-author): Exciton annihilation and transport in fifth order electronic spectroscopy, *European Conference on the Spectroscopy of Biological Molecules 2019*, Dublin, 2019

2. Poster (co-author): Interferometric Photocurrent Micro-Spectroscopy of Biased GaAs, *e-conversion Conference Venice 2019*, Venice, 2019

3. Talk: Exciton-exciton annihilation probed by fifth order coherent spectroscopy, *e-conversion: Workshop on Chemical and Energy Conversion at Interfaces*, Munich, 2020

Preface

This publication based thesis focuses on the following scientific work

1. C. Heshmatpour, J. Hauer, and F. Šanda. Interplay of exciton annihilation and transport in fifth order electronic spectroscopy. *Chem. Phys.*, 528:110433, 2020

2. C. Heshmatpour, P. Malevich, F. Plasser, M. Menger, C. Lambert, F. Šanda, and J. Hauer. Annihilation dynamics of molecular excitons measured at a single perturbative excitation energy. *J. Phys. Chem. Lett.*, 11(18):7776–7781, 2020

3. C. Heshmatpour, J. Hauer, and F. Šanda. Correlated spectral fluctuations quantified by line shape analysis of fifth-order two-dimensional electronic spectra. *J. Chem. Phys.*, 156(8):084114, 2022

to stay within a single research topic, namely fifth-order two-dimensional electronic spectroscopy.

Acknowledgements

The completion of this thesis would not have been possible without the help of many people, and I would like to express my sincere gratitude and appreciation to everyone involved before presenting any results.

While many PhD students are kept on their toes by one supervisor, I had the pleasure to be supervised by two excellent researchers: Jürgen Hauer and František Šanda. I am indebted to thank the both of you for the exceptional scientific and very personal supervision, which I do not take for granted. Thank you for the overall support throughout the whole time of my thesis, always encouraging me to get the best out of my research.

I am grateful to the Deutsche Forschungsgemeinschaft (DFG) for funding my research through TUM International Graduate School of Science and Engineering (IGSSE), GSC 81.

Additionally, I must express my gratitude to both Pavel Malevich and Lars Mewes for their assistance in the lab and general cheerful attitude.

I am also indebted to thank Craig Lincoln for teaching me the importance of attention to detail, back in the days at TU Wien.

Furthermore, I want to thank Andreas Stier and Lukas Wolz for all the helpful academic discussions and sharing their knowledge on photocurrent detection.

I am particularly grateful for all the valuable and helpful academic discussions with Erling Thyrhaug.

Special thanks also to my fellow PhD students and co-workers - Ajeet, Erika, Yang, Yi, Max, Hongxing, Annett, Vaclav, Matthias, Peter, Sabine K. and Sabine F. - for providing a comfortable and positive work environment where everyone helps everyone.

I am deeply grateful to Lysanne for her encouraging and loving nature which was a great support especially in the last phases of this work.

I would like to end with a big thank you to my parents - Fariborz and Ingeborg - and my brothers - Christoph and Christian - without your loving and active support I would never have gotten to where I am now. Thank you!

Abstract

Our understanding of exciton relaxation processes inside molecular aggregates is inevitable connected to the capability of scientific tools at hand to resolve them. A large repertoire of time-resolved spectroscopic methods has been developed to investigate transport of excitation energy inside excitonic systems on timescales ranging from femto- to picoseconds and substantially shaped our current understanding of this process.

Multi-exciton processes, such as exciton-exciton annihilation (EEA), are ubiquitous phenomena in excitonic systems but are far less studied as the commonly employed tools of time-resolved spectroscopy solely allow to study EEA as an intensity dependent perturbation to the signal, which intertwines transport with annihilation dynamics. Fifth-order two-dimensional electronic spectroscopy (R^5-2D) solves this spectroscopic problem most elegantly as it allows to directly and exclusively measure annihilation dynamics in aligned molecular homoaggregates *via* spectral integration of the R^5-2D signal. In this thesis we formally prove the latter by means of a theoretical analysis of the R^5-2D signal based on a developed master equation model. In a joint experimental and theoretical study of the R^5-2D signal we extend its applicability to non-aligned structures. In particular, we analysed the R^5-2D signal of a bent molecular homotrimer and identified a well isolated peak as reporter for EEA. We thus show that R^5-2D allows for the unique opportunity to study EEA in molecular aggregates without the need to study non-linear signals in their intensity dependence, *i.e.* at a single perturbative excitation density.

Besides the ability of R^5-2D to track annihilation dynamics we develop and apply lineshape analysis to this signal and show, in a theoretical study, that R^5-2D lineshape dynamics contain valuable information about fluctuation characteristics of molecular site and bi-exciton binding energies, such as possible correlation between site energy fluctuations. The latter are difficult to unambiguously identify in common third-order time-resolved experiments and these results thus display an important, yet different, application of R^5-2D.

Kurzfassung

Unser Verständnis von Exzitonen-Relaxationsprozessen innerhalb molekularer Aggregate ist unausweichlich mit der Leistungsfähigkeit der verfügbaren wissenschaftlichen Werkzeuge verbunden diese aufzulösen. Ein großes Repertoire an zeitaufgelösten spektroskopischen Methoden wurde entwickelt um den Transport von Anregungsenergie in exzitonischen Systemen auf Zeitskalen von Femto- bis Pikosekunden zu untersuchen und hat unser aktuelles Verständnis dieses Prozesses wesentlich geprägt.

Multi-Exziton-Prozesse, wie die Exziton-Exziton-Annihilation (EEA), sind allgegenwärtige Phänomene in exzitonischen Systemen, werden jedoch weit weniger untersucht, da die üblicherweise verwendeten Werkzeuge der zeitaufgelösten Spektroskopie es nur ermöglichen EEA als eine intensitätsabhängige Störung des Signals zu untersuchen die Transport- mit Annihilationdynamik verwebt. Zweidimensionale elektronische Spektroskopie fünfter Ordnung (R^5-2D) löst diese spektroskopische Fragestellung am elegantesten, da sie es ermöglicht direkt und ausschließlich die Annihilationsdynamik in ausgerichteten molekularen Aggregaten über spektrale Integration des R^5-2D-Signals zu messen. In dieser Arbeit beweisen wir letzteres formal durch eine theoretische Analyse des R^5-2D-Signals anhand eines entwickelten Mastergleichungsmodells. In einer sowohl experimentellen als auch theoretischen Untersuchung des R^5-2D-Signals erweitern wir die Anwendbarkeit von R^5-2D auf nicht ausgerichtete Strukturen. Im Speziellen haben wir das R^5-2D Signal eines geknickten molekularen Homotrimer untersucht und einen gut isolierten Peaks als Reporter für EEA identifiziert. Wir zeigen damit, dass R^5-2D die einzigartige Möglichkeit bietet, EEA innerhalb molekularer Aggregate zu untersuchen, ohne dass nichtlineare Signale in ihrer Intensitätsabhängigkeit untersucht werden müssen, das heißt bei einer einzigen perturbativen Anregungsdichte.

Neben der Fähigkeit von R^5-2D, die Annihilationdynamik zu verfolgen, entwickeln und wenden wir Linienformanalyse auf dieses Signal an und zeigen in einer theoretischen Studie, dass die R^5-2D Linienformdynamik wertvolle Informationen über Fluktuationseigenschaften von Monomerenergien und Bi-Exziton-Bindungsenergien enthält, wie zum Beispiel eine mögliche Korrelation zwischen Monomerenergiefluktuationen. Let-

ztere sind in üblichen zeitaufgelösten Experimenten dritter Ordnung schwer eindeutig zu identifizieren und diese Ergebnisse zeigen daher einen wichtigen, aber anderen Anwendungsfall, von R^5-2D.

Contents

1. Introduction

Experimental methods developed in the field of optical spectroscopy are the primary scientific tool for unravelling steady-state and dynamic properties of atoms, molecules and molecular aggregates. Absorption spectroscopy is the natural starting point for such studies as it provides the most essential information about the investigated system:[6] Steady-state properties such as energetic positions and transition dipole moment strengths of optically allowed transitions from ground to higher lying states are, respectively, represented in observed peak positions and areas. Additionally, absorption spectra already provide first but indirect information about dynamical properties of the investigated system, as their lineshapes are influenced by the type of system-bath (molecule-solvent) interaction and the homogenous linewidth encodes lifetimes of excited states embedded in the total dephasing timescale of optical coherences.[7,8]

Despite the fact that we can observe signatures of such dynamic effects already on the level of steady-state absorption spectroscopy, it is not possible to extract them unambiguously. To determine transport rates between excited states, time-resolved optical spectra have to be measured and analysed. Such experiments employ a specific sequence of time-delayed ultrashort laser pulses to both prepare an optical excitation inside the molecular aggregate, known as exciton (see chapter 2), and to track its relaxation subsequent to photoexcitation by monitoring changes in the absorption spectrum. We provide an overview of time-resolved methods to study exciton transport in section 2.1.

Besides exciton transport dynamics, interactions between excitons are also important. The process of excitation energy quenching by fusion of two neighbouring excitons followed by nonradiative relaxation, known as exciton-exciton annihilation[9,10] (EEA), sets an upper limit for the exciton density[11] and thereby hampers the efficient conversion from light into usable energy in *e.g.* organic solar cells.[12,13]. Intensity-dependent measurements have become the standard approach to study EEA[14,15] despite the fact that it is prone to experimental artefacts,[16] and furthermore intertwines transport and annihilation signal contributions which complicates data analysis. We discuss recent approaches to measure interactions between excitons in section 2.2, with an emphasis

on the spectroscopic technique at the heart of this thesis: fifth order two-dimensional electronic spectroscopy (R^5-2D).

Briefly, R^5-2D is a modern coherent two-dimensional time-resolved spectroscopic technique detected along $\vec{K}_{R5-R,R5-NR} = \mp 2\vec{K}_1 \pm 2\vec{K}_2 + \vec{K}_3$ phase matching directions, and tailored for investigating the interaction between two excitons.[17,18] The alluring feature of R^5-2D is that EEA dynamics directly determine the spectroscopic signal and does not have to be extracted by model-based analysis of intensity-dependent measurements. Early applications of R^5-2D[18,19] employed the method to study the diffusion limited annihilation process inside large molecular aggregates occurring on a picosecond timescale. The main goal of this thesis is to employ R^5-2D to measure the femtosecond annihilation timescale inside small molecular aggregates, as they allow for a detailed theoretical description which aids to interpret the rather complex fifth-order spectra. To this end we first investigated the signal theoretically, based on a developed master equation description tailored for small aggregates in

1. C. Heshmatpour, J. Hauer, and F. Šanda. Interplay of exciton annihilation and transport in fifth order electronic spectroscopy. *Chem. Phys.*, 528:110433, 2020.

We formally proved that the annihilation time constant in homoaggregates with aligned transition dipoles can be determined by a frequency-integrated R^5-2D signal. This is possible at a single, perturbative excitation energy and alleviates the need for cumbersome and potentially artefactual intensity dependent studies. The latter point was exemplified in the combined experimental and theoretical study

2. C. Heshmatpour, P. Malevich, F. Plasser, M. Menger, C. Lambert, F. Šanda, and J. Hauer. Annihilation dynamics of molecular excitons measured at a single perturbative excitation energy. *J. Phys. Chem. Lett.*, 11(18):7776–7781, 2020

where we demonstrated that the ultrafast annihilation rate inside a non-aligned molecular trimer can also be obtained from R^5-2D by following the temporal evolution of a specific peak. Specifically, we extracted a 30 fs annihilation rate from the R^5-2D signal.

Inspired from the experimentally observed peak tilt in R^5-2D lineshapes we developed and applied the concept of lineshape analysis to R^5-2D in

3. C. Heshmatpour, J. Hauer, and F. Šanda. Correlated spectral fluctuations quantified by line shape analysis of fifth-order two-dimensional electronic spectra. *J. Chem. Phys.*, 156(8):084114, 2022.

We established, using numerical simulations and analytical treatments of the underlying fluctuation statistics, a connection between the lineshape tilt of R^5-2D homodimer spectra and the spectral fluctuation characteristics of molecular on-site and bi-exciton binding energies. This study thus demonstrates a different application of R^5-2D besides its ability to track annihilation dynamics.

The results of the above articles 1.-3. are, respectively, summarized in more detail in sections 3.1-3.3, and reprints of the published manuscripts are provided in Appendix A-C.

These three research articles form the basis of this publication based thesis and provide rigorous explanations of the employed theoretical formalism but expect the reader to be familiar with the concept of molecular excitons and time-resolved methods of optical spectroscopy, in particular multi-dimensional electronic spectroscopy. We thus broadly review these topics in the next chapter and elaborate the need of adding R^5-2D, as a tailored probe for exciton interactions such as EEA, to the arsenal of ultrafast spectroscopy in the final section 2.2 of the next chapter.

2. Optical spectroscopy of molecular excitons

The concept of molecular excitons as an electronic excitation shared by many chromophores in a molecular crystal [20] or by more than one pigment in molecular aggregates, such as *e.g.* in photosynthetic pigment-protein complexes, [21] was originally developed by Frenkel [22,23] in 1931. To understand the formation of these delocalized molecular excitons we will start by considering a molecular aggregate consisting of N chromophores where each site n possesses two electronic levels: a ground state $|g_n\rangle$ and an excited state $|e_n\rangle$, separated by site energy E_n. The joint Hilbert space of such an aggregate reads

$$\mathcal{S} = \{|g_1\rangle, |e_1\rangle\} \otimes \{|g_2\rangle, |e_2\rangle\} \cdots \otimes \{|g_{N-1}\rangle, |e_{N-1}\rangle\} \otimes \{|g_N\rangle, |e_N\rangle\}. \tag{2.1}$$

Grouping the many-body states according to the number of excitations one can rearrange the above set to read

$$\mathcal{S} = \{\mathcal{M}_0, \mathcal{M}_1 \ldots, \mathcal{M}_{N-1}, \mathcal{M}_N\}, \tag{2.2}$$

where subset $\mathcal{M}_0$ contains the many-body state with zero excitations, *i.e.* the total ground state $|0\rangle \equiv \prod_{n=1}^{N} \otimes |g_n\rangle$. Subset $\mathcal{M}_1$ is composed of N many-body states $|n\rangle \equiv |e_n\rangle \prod_{k=1;k\neq n}^{N} \otimes |g_k\rangle$ where one site is excited, $\mathcal{M}_2$ accommodates all $\frac{N(N-1)}{2}$ many-body states $|nm\rangle \equiv |e_n e_m\rangle \prod_{k=1;k\neq n,k\neq m}^{N} \otimes |g_k\rangle$ with two excitations and so forth.

We can switch to a proper many-body formalism by introducing operators

$$\hat{B}_n^\dagger \equiv \underbrace{\mathbb{1} \otimes \mathbb{1} \cdots \otimes \mathbb{1}}_{n-1 \text{ terms}} \otimes |e_n\rangle \langle g_n| \otimes \underbrace{\mathbb{1} \cdots \otimes \mathbb{1}}_{N-n \text{ terms}} \tag{2.3}$$

and

$$\hat{B}_n \equiv \underbrace{\mathbb{1} \otimes \mathbb{1} \cdots \otimes \mathbb{1}}_{n-1 \text{ terms}} \otimes |g_n\rangle \langle e_n| \otimes \underbrace{\mathbb{1} \cdots \otimes \mathbb{1}}_{N-n \text{ terms}}, \tag{2.4}$$

where $\mathbb{1}$ is the single-particle identity matrix. These operators, respectively, create and

annihilate an excitation at site n and obey the Pauli commutation relation

$$\left[\hat{B}_n, \hat{B}_m^\dagger\right] \equiv \delta_{nm}(1 - 2\hat{B}_n^\dagger \hat{B}_n). \tag{2.5}$$

All many-body (site basis) states contained in $\mathcal{S}$, *i.e.* all local states of an aggregate, can thus be constructed from the total ground state $|0\rangle$ by acting with the creation operator $\hat{B}^\dagger$ from the left, assigning it the meaning of a vacuum state. States with one or two excitations are *e.g.* obtained by

$$\begin{aligned} \hat{B}_n^\dagger |0\rangle &= |n\rangle \\ \hat{B}_m^\dagger \hat{B}_n^\dagger |0\rangle &= |nm\rangle\,, \end{aligned} \tag{2.6}$$

respectively. The action of the annihilation operator on the total ground state gives zero, *i.e.*

$$\hat{B}_n |0\rangle = 0. \tag{2.7}$$

With the aid of the above creation and annihilation operators one can formulate the electronic energy level structure and dynamics inside the aggregate by introducing the Frenkel exciton Hamiltonian.[23] In the simplest form sufficient to describe transport dynamics it reads[1]

$$\hat{H} = \sum_{n=1}^{N} E_n \hat{B}_n^\dagger \hat{B}_n + \sum_{\substack{n,m=1 \\ n \neq m}}^{N} J_{nm} \hat{B}_n^\dagger \hat{B}_m, \tag{2.8}$$

and has been successfully applied to describe optical spectra of molecular aggregates, such as photosynthetic systems[24] or J-aggregates.[25] The occurring intermolecular Coulomb interactions J_{nm} between chromophores n and m represent off-diagonal elements and are responsible for the formation of excitons as collective excited states delocalized over several chromophores.

To exemplify the above statement and to get further into the implications of the Frenkel exciton model we will in the following discuss the example of a homotrimer

[1] To adequately capture bi-exciton spectral features in Ref. [4] we have accounted for bi-exciton binding energy Δ_{nm} by adding the term $1/2 \sum_{\substack{n,m=1 \\ n \neq m}}^{N} \Delta_{nm} \hat{B}_n^\dagger \hat{B}_m^\dagger \hat{B}_n \hat{B}_m$ to Eq. (2.8)

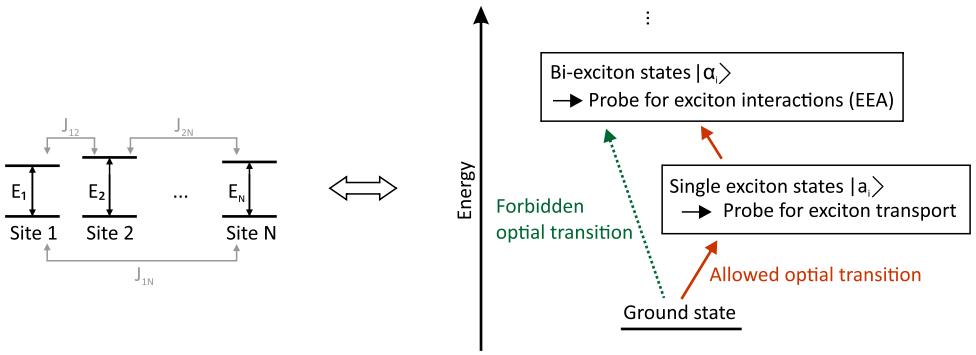

Figure 2.1.: Electronic level structure of a molecular aggregate consisting of N two-level chromophores. The excitonic coupling J leads to the formation of bands, where states inside each band contain the same amount of excitations. The selective excitation of single excitons states $|a_i\rangle$ (bi-exciton states $|\alpha_i\rangle$) allows to study exciton transport (interactions). Excitation of bi-exciton states can, however, be difficult as optical transitions from ground to bi-exciton states are forbidden.

($N = 3$, $E_1 = E_2 = E_3 = E$), where Hamiltonian (2.8) assumes the form

$$H_{Homotrimer} = \begin{pmatrix} H_0 & 0 & 0 & 0 \\ 0 & H_1 & 0 & 0 \\ 0 & 0 & H_2 & 0 \\ 0 & 0 & 0 & H_3 \end{pmatrix}, \tag{2.9}$$

when expanded in its local ($J = 0$ in Eq. (2.8)) eigenstates. The individual blocks read

$$H_0 = 0, \tag{2.10}$$

$$H_1 = \begin{pmatrix} E & J_{12} & J_{13} \\ J_{21} & E & J_{23} \\ J_{31} & J_{32} & E \end{pmatrix}, \tag{2.11}$$

$$H_2 = \begin{pmatrix} 2E & J_{23} & J_{13} \\ J_{32} & 2E & J_{12} \\ J_{31} & J_{21} & 2E \end{pmatrix}, \tag{2.12}$$

and

$$H_3 = 3E, \tag{2.13}$$

employing the ordering $\{|0\rangle, |1\rangle, |2\rangle, |3\rangle, |12\rangle, |13\rangle, |23\rangle, |123\rangle\}$ of local excitonic states.

The obtained matrix representation (2.9) is block diagonal and local states with the same number of excitations are mixed inside each block. This observed structure is a general property of Hamiltonian (2.8) and the blocks, referred to as manifolds, can be diagonalized separately: in the case of the homotrimer - assuming nearest neighbour coupling $J_{13} = J_{31} = 0$ and $J_{12} = J_{23} = J$ - one obtains one ground state $|0\rangle$ with energy $E_g = 0$, three states

$$\begin{aligned} |a_1\rangle &= \frac{1}{2}(|1\rangle - \sqrt{2}\,|2\rangle + |3\rangle) \\ |a_2\rangle &= \frac{1}{\sqrt{2}}(|1\rangle - |3\rangle) \\ |a_3\rangle &= \frac{1}{2}(|1\rangle + \sqrt{2}\,|2\rangle + |3\rangle) \end{aligned} \tag{2.14}$$

containing one excitation positioned at energies $E_{a_1} = E - \sqrt{2}J$, $E_{a_2} = E$ and $E_{a_3} = E + \sqrt{2}J$; three states

$$\begin{aligned} |\alpha_1\rangle &= \frac{1}{2}(|12\rangle - \sqrt{2}\,|13\rangle + |23\rangle) \\ |\alpha_2\rangle &= \frac{1}{\sqrt{2}}(|12\rangle - |23\rangle) \\ |\alpha_3\rangle &= \frac{1}{2}(|12\rangle + \sqrt{2}\,|13\rangle + |23\rangle) \end{aligned} \tag{2.15}$$

containing two excitations situated at $E_{\alpha_1} = 2E - \sqrt{2}J$, $E_{\alpha_2} = 2E$ and $E_{\alpha_3} = 2E + \sqrt{2}J$; and one state $|f\rangle = |123\rangle$ containing three excitations with energy $E_f = 3E$. The introduction of J thus leads to delocalized states of the homotrimer in first (Eq. (2.14)) and second (Eq. (2.15)) manifold which are split by $\sqrt{2}J$ around E and $2E$, respectively. The optical transition strength between excitonic states $|i\rangle$ and $|j\rangle$ of the homotrimer is defined as

$$\vec{\mu}_{ij} \equiv \vec{d}\,\langle i|\,(\hat{B}_1^\dagger + \hat{B}_2^\dagger + \hat{B}_3^\dagger)\,|j\rangle\,, \tag{2.16}$$

where $\vec{d}$ is the transition dipole moment of the monomer. Optical transitions are thus solely possible between manifolds differing in one quantum of excitation.

The excitonic states of the aggregate comprised of a superposition between local one/two/three/... exciton states are referred to as (electronic) single-/bi-/tri-/... exciton states, respectively. The selective excitation of these states allows to study various transport and relaxation phenomena inside molecular aggregates as depicted in Fig. 2.1. A probe for exciton transport can be defined in terms of dynamics of single exciton states which are accessible from the ground state (see Eq. (2.16)) by weak field excitation

($\propto \mathcal{E}^2(t)$, where $\mathcal{E}(t)$ is the electric field). The various spectroscopic methods developed to study exciton transport are reviewed in section 2.1. Studying the dynamics of multi-excitonic states calls for their selective excitation. This is however a difficult task as optical transitions from ground to bi-exciton states are forbidden (see Eq. (2.16)). Spectroscopic methods overcoming this obstacle are discussed in section 2.2.

2.1. Exciton transport

The efficient transport of excitation energy is defined by processes occurring immediately after photo excitation and is of crucial importance for the function of natural[26] or artificial[27] light harvesting systems. A detailed understanding of these initial ultrafast transport processes is therefore crucial for the development of optoelectronic devices, such as organic solar cells,[28] as the absorbed excitation energy must be guided through the appropriate relaxation pathways for efficient photocurrent generation. Natural light harvesting complexes have already an remarkably high conversion efficiency - 9 out of 10 photons create a charge separated state[26] - and exciton transport has thus been investigated intensively in these systems.[29,30,31]

Due to the importance of transport processes a large ensemble of spectroscopic techniques has been developed for their investigation. They are reviewed in this section grouped into coherent (section 2.1.1) and action detected methods (section 2.1.2).

2.1.1. Coherent methods

The conceptually simplest experimental method to study exciton transport is pump-probe (PP) spectroscopy.[33] Its general concept is depicted in Fig. 2.2 (A): PP involves two ultrashort pulses, referred to as pump and probe, arranged in a non-collinear geometry with a controllable time delay t_2 between the two pulses. The pump is used to excite the sample and thereby resulting absorption changes $\Delta A(t_2, \Omega_3)$ are measured by spectrally resolving the probe pulse in detection frequency Ω_3 after a specific time delay t_2. The PP signal is then obtained by referencing the spectrum of the transmitted probe pulse with ($\tilde{I}_{pump-on}(t_2, \Omega_3)$) and without ($\tilde{I}_{pump-off}(\Omega_3)$) an initial pump pulse, according to

$$\Delta A(t_2, \Omega_3) = \log\left(\frac{\tilde{I}_{pump-off}(t_2, \Omega_3)}{\tilde{I}_{pump-on}(\Omega_3)}\right). \tag{2.17}$$

Interpreting PP as two consecutive absorption events, we can disentangle the signal into three contributions: the so-called ground state bleach (GSB) contribution originates

(A) Pump probe:

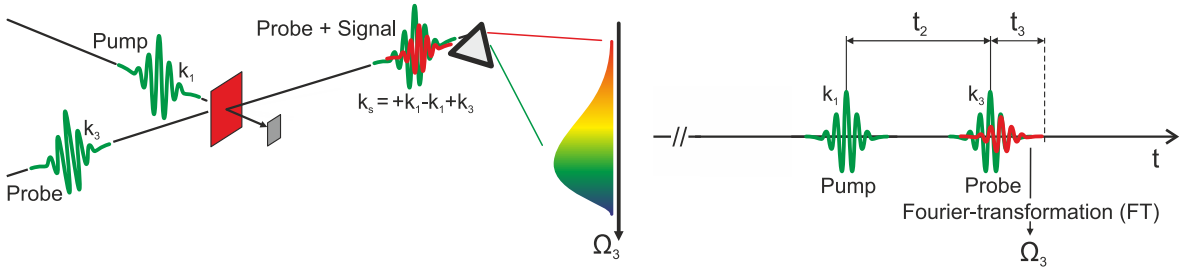

(B) Double sided Feynman diagrams contributing to pump probe spectroscopy:

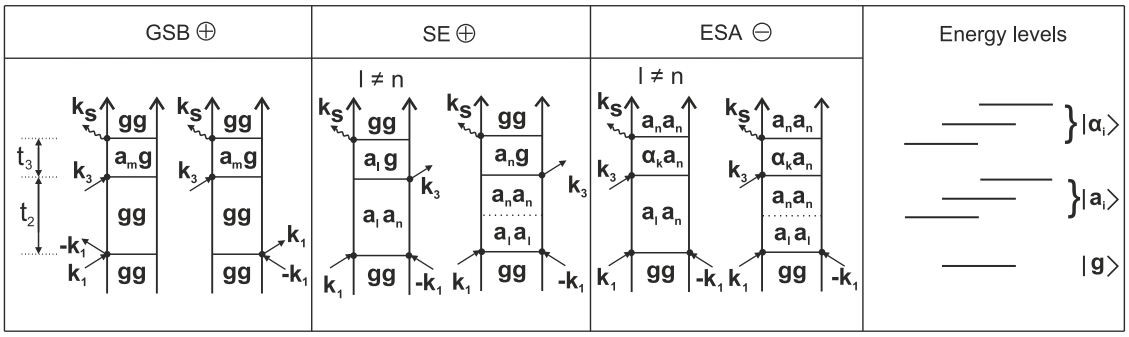

(C) Two-dimensional electronic spectroscopy (R^3-2D) in pump probe geometry:

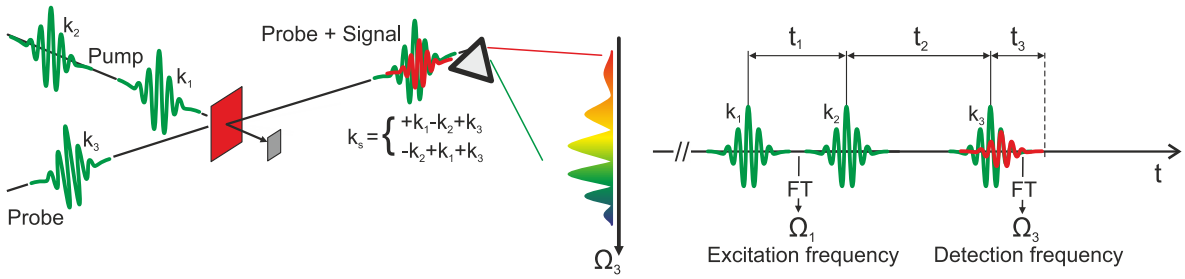

Figure 2.2.: (A) Experimental configuration of a pump probe experiment: the pump pulse excites the sample (red square). Thereby induced transient absorption changes are measured after a delay time t_2 by spectrally resolving the probe pulse, intersecting the pump pulse at the sample position. (B) Double-sided Feynman diagrams for pump probe spectroscopy. Ground, single and bi-exciton states are denoted with $|g\rangle$, $|a_i\rangle$ and $|\alpha_i\rangle$, respectively. (C) Experimental configuration of a two-dimensional electronic spectroscopy (R^3-2D) experiment in pump probe geometry: the pump pulse is split into two replicas with variable delay t_1. A Fourier-transform of the measured data along t_1 allows to display the signal as a two-dimensional map of excitation and detection frequencies; (A) and (C) adapted from Ref. [32]

from the fact that a fraction of the molecules in the sample is already excited by the pump such that the absorption of the probe is reduced (bleached). Hence, more light reaches the spectrometer and we assign this contribution a positive value. Stimulated emission (SE) from already excited molecules, triggered by the probe pulse, also leads to more light and thus to a positive signal contribution. An increase in absorption occurs via excited state absorption (ESA): after the pump pulse populates single exciton states, transitions to higher lying bi-exciton states are possible. This pump-induced absorption contribution leads to less light on the spectrometer as compared to a scenario where the pump pulse is blocked. Hence, ESA is attributed a negative sign.

While this heuristic approach is helpful to understand the basics of PP, it quickly reaches its limits when trying to understand more evolved time-resolved methods involving more than two pulses. The response function formalism[34] in combination with the density matrix formalism[35] as described by Mukamel[7] provides the ideal theoretical framework to disentangle the PP signal, and in fact any time-resolved signal, into its individual contributions and an extensive literature exists reviewing this topic.[36,37] In terms of Mukamel's formalism, we understand the PP signal of the sample to originate from a third-order non-linear polarization, calculated by means of a perturbative expansion of the density matrix up to the third-order in the electric field, and generated by two light-matter interactions of the pump pulse and one from the probe pulse. The measured signal is phase-matched along $\vec{K}_{PP} = +\vec{K}_1 - \vec{K}_1 + \vec{K}_3$, where $\vec{K}_1$ ($\vec{K}_3$) is the wave vector of the pump (probe) pulse. Hence, the non-linear and time-dependent signal of interest co-propagates with the probe pulse.

The individual signal contributions are, within Mukamel's formalism, most conveniently represented pictorially by so-called double-sided Feynman diagrams.[7] The diagrams for PP are depicted in Fig. 2.2(B): time is increasing from bottom to top and the vertical lines represent the ket and bra of the density matrix. Interactions with the electric field are denoted with straight arrows where an (outward) inward pointing arrow represents (de-)excitation. The last wavy arrow represents the signal. Transport between excitonic states is described *via* transfer between populations (diagonal density matrix elements) during t_2, and is denoted by dotted vertical lines.

Similar to the heuristic analysis sketched above, one gets three different classes of diagrams (contributions) called GSB, ESA and SE. From the diagrams depicted in Fig. 2.2(B), we can understand that the PP technique probes exciton transport dynamics between single exciton states $|a\rangle$, encoded in the dynamics of ESA and SE contributions, as the system's density matrix may evolve between single exciton populations during the

waiting time t_2. The t_2 evolution of the PP signal might also be affected by dynamics of coherences (off-diagonal density matrix elements) leading to beating features in t_2. In coherence interval t_3, the frequency of the probed coherence defines the spectral position at which the individual PP diagrams contribute along detection frequency Ω_3. Typical pump probe experiments thus involve a narrow-band pump to excite a specific single exciton state $|a\rangle$. Transport dynamics subsequent to photoexcitation are monitored with a broadband probe pulse covering a multitude of optical transitions to extract the maximum amount of information. The temporal resolution of the PP method is thus determined by the temporal cross correlation of pump and probe pulses and is in the range of 150 fs in standard experiments.[38] The spectral bandwidth and resolution are determined by the white light generating mechanism[39] for the probe pulse and the resolution of the employed spectrometer, respectively.

Despite the success of PP to understand photoinduced transport dynamics, it suffers from two fundamental limitations: first, the selective excitation of a single exciton state comes at the expense of sacrificing temporal resolution in the experiment as a narrow-band pump pulse in frequency domain is inherently long in time domain; second, GSB/SE and ESA contributions (see Fig. 2.2(B)) can overlap and partially cancel, rendering the interpretation of the data difficult, which is one of the reasons why global analysis approaches are widely applied for PP data interpretation.[40]

Both of these problems can be overcome if the pump pulse is split into two phase-stable replicas with precisely controllable time delay t_1, as depicted in Fig. 2.2(C). The first two interactions in PP diagrams of Fig. 2.2(B) are in this way experimentally distinguishable and it becomes possible to measure an additional coherence interval t_1, from which the so-called excitation frequency Ω_1 can be obtained via a Fourier transformation. By utilizing a broadband pump it thus possible to simultaneously optimize time and frequency resolution of the technique.[41] The measured signal at a given population time t_2 transformed into the mixed time-frequency domain $\tilde{R}^3(\Omega_1, t_2, \Omega_3)$ represents a two-dimensional map, where contributions overlapping in PP are separated, at least partially. This method is thus called two-dimensional electronic spectroscopy (R^3-2D).[42] In terms of the response function formalism, we understand it as a coherent third-order signal emitted into $\vec{K}_{R3-R,R3-NR} = \mp\vec{K}_1 \pm \vec{K}_2 + \vec{K}_3$ phase matching directions. The diagrams for R^3-2D are depicted in Fig. 2.3. As compared to PP, R^3-2D has the richer information content as it fully resolves all coherences (along both t_1 and t_3), while PP integrates over excitation frequency Ω_1, which is equivalent to setting $t_1 = 0$ fs.[1] PP and R^3-2D are thus different representations of the same third-order non-linear signal. The additional

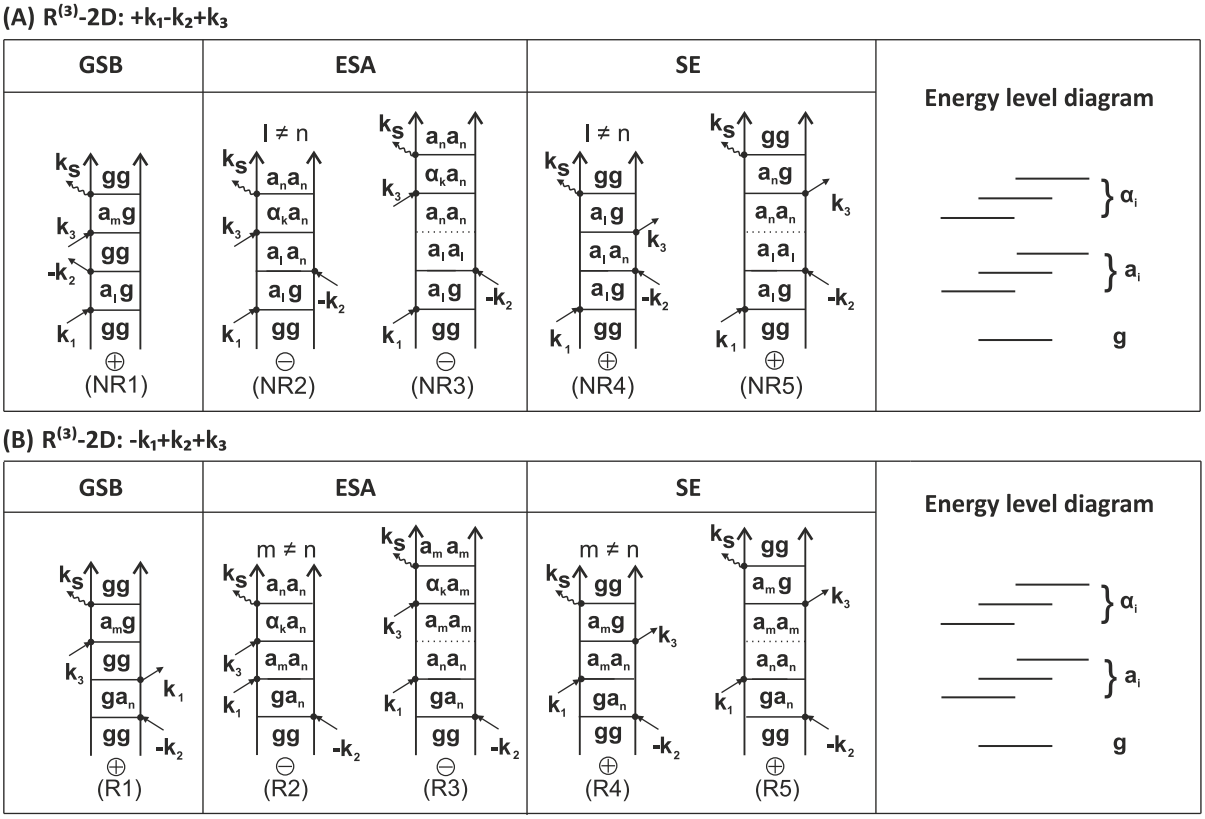

Figure 2.3.: Double-sided Feynman diagrams for non-rephasing (A) rephasing (B) R^3-2D. Ground, single and bi- exciton states are denoted with $|g\rangle$, $|a_i\rangle$ and $|\alpha_i\rangle$, respectively. Reprinted from [2]

dimension of R^3-2D brings, however, many advantages as discussed in the following.

An intuitive way of interpreting the obtained maps is to view them as correlation plots between excitation and detection frequencies of the system: Diagonal peaks appear if the molecule absorbs and emits light at the same frequency, whereas off-diagonal features appear if the molecule emits at a frequency different to its excitation frequency. Off-diagonal (cross) peaks are thus a clear indication for couplings between electronic states and following their temporal evolution allows to directly track transport between them.[42] Cross peaks are thus assigned an essential role in R^3-2D and cross-peak-specific R^3-2D has been developed to minimize spectral overlap between off-diagonal and broad diagonal features.[43] However, diagonal peaks are not entirely undesirable and also carry useful information: at $t_2 = 0$ fs they allow to disentangle homogeneous from inhomogeneous broadening and their lineshape changes as a function of t_2 allow to determine the system's frequency correlation function.[44] R^3-2D is thus a versatile experimental tool and has *e.g.* been applied to study exciton transport in light harvesting complexes,[45,46]

semiconducting single-walled carbon nanotubes,[47,48] or two-dimensional materials.[49]

The experimental implementation of R^3-2D depicted in Fig. 2.2(C) is called 2D in pump-probe geometry and is the conceptually simplest approach to step from PP spectroscopy to multi-dimensional techniques.[50] However, it comes with its limitations as the desired signal manifests itself as small modulations on an intense background, namely the probe pulse. This is a disadvantage for weak signals.[51] Additionally, 2D in PP-geometry ($\vec{K}_1 = \vec{K}_2$) merges the diagrams of signals $\vec{K}_{R3-R,R3-NR}$, unless phase cycling routines including pulse shaping devices are employed.[52] These so-called (non-)rephasing R^3-2D spectra are, however, instrumental to analyse and identify the origin of observed oscillatory beatings via so-called oscillation maps.[53] To measure these two signals separately, non-collinear ($\vec{K}_1 \neq \vec{K}_2$) variants of R^3-2D have been developed, where the two signals are either spatially separated[54] or distinguished by pulse timing sequences.[55] The most prominent implementation of a fully non-collinear phase matching geometry is the so-called folded boxcar geometry as depicted in Fig. 2.4. This experimental realization involves four laser pulses. The three pump pulses $\vec{K}_{1-3}$ create the third-order signal, which is usually mixed with an additional pulse called the local oscillator (LO) to characterize the signal in both magnitude and phase (or the real and imaginary signal component) in a procedure called phasing.[42] In the latter, the mentioned equality between PP and excitation frequency integrated R^3-2D is exploited to yield the absorptive part of the R^3-2D signal. The main advantage of non-collinear 2D is thus a background-free detection and the facile separate detection of rephasing and non-rephasing spectra. The main disadvantage is the necessity to phase, *i.e.* the need to determine the absorptive part of the signal. The fact that the probe pulse in PP-geometry 2D serves as both the third excitation pulse and the local oscillator leads to the direct detection of absorptive signals.[56]

PP and R^3-2D - in their various experimental realizations - are robust and mature coherent methods to track exciton transport dynamics. As depicted in the experimental schemes in Figs. 2.2 and 2.4, they generally rely on transmissive samples with an optical density of hundreds of milli-OD (optical density) for appreciable signal strengths in typical experiments. If the analyte concentration is lower, down to the single molecule regime, incoherent detection methods are called for. Such incoherent or action-detected techniques rely on a background-free signals as reporters for excited state population. A typical example is fluorescence, with a large body of work for single molecule detection[57], but also photocurrent[58,59], photoelectrons[60] or photoions[61] have been suggested. In the next chapter we provide an overview of action-detected multidimensional

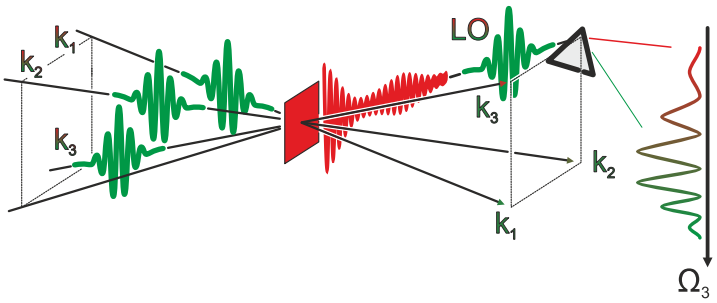

Figure 2.4.: Sketch of a R^3-2D experiment in boxcar geometry. The non-linear signal is created in $\vec{K}_{R3-R} = -\vec{K}_1 + \vec{K}_2 + \vec{K}_3$ phase matching direction and interferes with a local oscillator (LO) on the spectrometer such that the spectral phase can be obtained (see main text); adapted from Ref. [32]

spectroscopy.

2.1.2. Action detected methods

The two-dimensional implementation of action-detected techniques employ four (often collinear) ultrashort laser pulses as both coherence times t_1 (between pulse 1-2) and t_3 (between pulse 3-4) need to be scanned to obtain the Ω_1 and Ω_3 axes via a numerical Fourier transformation (see Fig. 2.5(A)). The single exciton dynamics are obtained by scanning the waiting time t_2 (between Pulse 2-3). To disentangle the specific action signal of interest from all detected signal components, either phase modulation of the pulses in combination with lock-in detection[63,64] or phase cycling[65] is employed. It is thus common practice to write the signal "direction" in terms of the spectral phase Φ and the action detected variants of R^3-2D and PP are detected along $\Phi_{2D} = \mp\Phi_1 \pm \Phi_2 + \Phi_3 - \Phi_4$ and $\Phi_{PP} = \Phi_1 - \Phi_1 + \Phi_3 - \Phi_4$, respectively. Despite the fact that the PP version of the experiment requires only three pulses (the first two interactions are again from pulse 1) and is thus much simpler to realize experimentally - compared to the four pulse sequence required for the two-dimensional variant - it has so far only been realized for fluorescence detection.[66]

The double-sided Feynman diagrams contributing to action detected 2D (AD-2D) are depicted in Fig. 2.5(B): four field interactions are used to create an excited-state population which incoherently and spontaneously emits the signal field, denoted by two wavy arrows, in contrast to the coherently emitted signal field of R^3-2D (see Fig. 2.2 (B)). In the following analysis of AD-2D we avoid a detailed theoretical description of detection and consider each diagram at $t_4 = 0$ fs and weighted by the quantum yield of the emitting

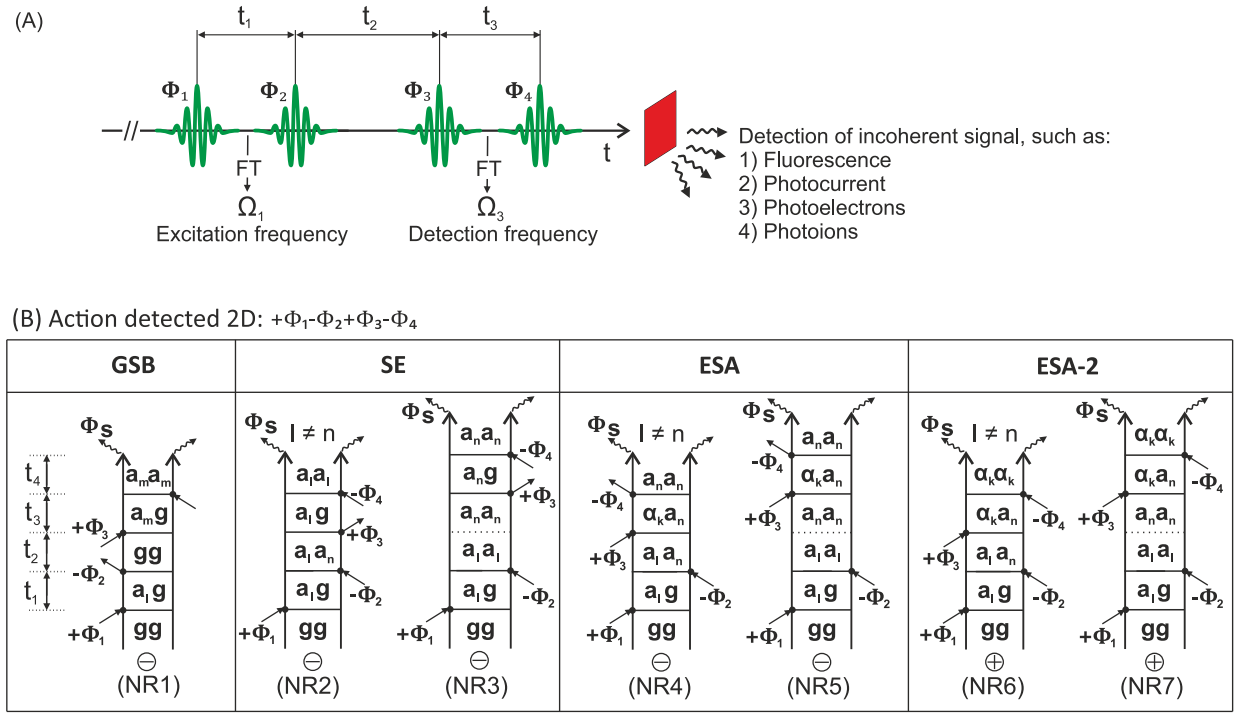

Figure 2.5.: (A) Experimental configuration of an AD-2D experiment with an all-collinear pulse sequence. Adapted from Ref. [32]. (B) Non-rephasing double-sided Feynman diagrams for action detected 2D. Signal emission is depicted with two wavy arrows, in contrast to the coherent diagrams depicted in Fig.2.4. The rephasing diagrams can be found in Ref. [62]. Ground, single and bi- exciton states are denoted with $|g\rangle$, $|a_i\rangle$ and $|\alpha_i\rangle$, respectively.

state.[67] Similar to coherent R^3-2D, AD-2D probes single exciton transport dynamics between states $|a\rangle$ during the waiting time t_2 (SE, ESA and ESA-2 diagrams in Fig. 2.5). However, AD-2D has besides the GSB, SE and ESA contributions an additional set of diagrams referred to as ESA-2 (see Fig.2.5(B)), which is the only pathway ending in the bi-exciton manifold. This additional set of diagrams leads to a different structure of the measured signal, especially at the cross-peak region; *e.g.* in fluorescence detected 2D (FL-2D) measurements performed on the light harvesting complex 2 (LH2)[68,69] strong cross peaks at early waiting times were found, which are absent in coherent R^3-2D data.[70,71] This finding seems rather inconsistent at first sight as it is commonly agreed upon that cross peaks in R^3-2D represent coupling between excited states. However, despite many similarities of the two techniques such an interpretation of cross peaks can not be directly applied to the signal structure of FL-2D.[72,67] The strong cross peaks in FL-2D of LH2 are attributed to an ESA free signal as complete annihilation of the

created bi-excitons in the t_4 interval of the ESA-2 pathways, *i.e.* before signal emission, leads to an identical quantum yield of the ESA and ESA-2 diagrams such that they cancel identically.[73]

In principle, any coherent signal has its action detected counterpart but their signal structure should not be interpreted on a common footing, as demonstrated by the example of FL-2D on LH2. An in depth comparison between coherent and action detected techniques can be found in Ref. [62].

2.2. Exciton interactions

Interactions between excitons, *i.e.* non-linear exciton dynamics, are far less studied as compared to simple exciton transport. This is due to the experimentally challenging observation of exciton-exciton interaction, given the methods introduced in section 2.1. Nevertheless, exciton-exciton interaction is fundamentally important. EEA, referring to the process of excitation energy quenching by fusion of two neighbouring excitons followed by non-radiative relaxation,[10,9] presents a prominent example of non-linear exciton dynamics. It can be viewed as a fundamental process defining an upper limit for the exciton density inside the material under study.[11] Efficient EEA thus represents a limiting factor for lasers based on organic thin films[74] and hampers the conversion from light into usable energy in organic solar cells.[12,13] EEA can also be utilized in technological applications, as it explains the unconventional photocurrent generation efficiency of van der Waals heterostructure through the creation of hot holes,[75] and plays an important role in the photoprotection of natural light harvesting complexes by efficiently removing excess energy.[76,77,78,79] From the point of view of basic research, EEA can be used to determine exciton diffusion constants[80,81] as excitons need to migrate to adjacent sites to annihilate. Time-resolving annihilation dynamics thus provides information to identify undesirable loss channels, but also provides insights into general properties of the material under study, such as their energy level structure.[82,83,84] The following paragraphs will give an overview on the time-resolved methods capable of quantifying the timescales associated with EEA.

The time-resolved methods described in section 2.1 are inherently designed for the study of excitation energy transport during the waiting time t_2 as dynamics of multi-exciton populations do not enter their perturbative analysis (see Fig. 2.4(B), Fig. 2.5, Fig. 2.7(B)). Such methods are often referred to as single quantum (1Q) techniques. In coherent 1Q-methods, effects of the interaction between two excitons are limited

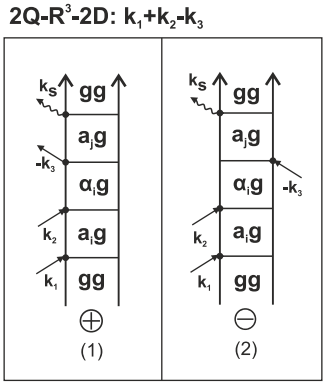

Figure 2.6.: Double-sided Feynman diagrams for 2Q-R^3-2D. Ground, single and bi- exciton states are denoted with $|g\rangle$, $|a_i\rangle$ and $|\alpha_i\rangle$, respectively.

to additional broadening of the ESA transitions (see Fig. 2.2(B) and Fig. 2.5) along the Ω_3 axis, which does not allow for a quantitative extraction of annihilation rates. In action detected 1Q-methods, exciton interactions have a profound implication on the signal structure as explained in section 2.1.2. For fluorescence detection it has been suggested from theoretical simulations that gating the emitted florescence with an additional pulse, thus resolving the t_4 interval, provides insight into the annihilation process itself.[67,73] However, such an approach cannot be straightforwardly expanded to other action detected methods such as *e.g.* photocurrent.

A more broadly applicable and direct extension to 2Q-coherences is provided by the so-called double quantum or 2Q-R^3-2D method, measured along $\vec{K}_{2Q-R3-2D} = \vec{K}_1 + \vec{K}_2 - \vec{K}_3$ phase matching direction.[2] It has been applied to study electron correlation and quantum mechanical exchange effects in molecules[86] and exciton-exciton correlation in semiconductors.[87] The double-sided Feynman diagrams contributing to the signal are depicted in Fig. 2.6 from which we can see that the system evolves in a 2Q-coherence, between ground state $|g\rangle$ and bi-exciton state $|\alpha\rangle$, in the t_2 interval. To correlate this 2Q-coherence with a 1Q-coherence the 2Q-R^3-2D signal is displayed as a two-dimensional map by applying a Fourier transform along t_2 and t_3 for a fixed value of t_1, commonly $t_1 = 0$ fs. An experimental realization of the method thus requires phase stability to a 2Q-coherence in the t_2 interval, which is a major challenge as many experimental implementation of 2D provide solely phase stability in t_1 and t_3 intervals; experimental schemes overcoming this obstacle have, however, been developed.[88] Pulse related

[2]Note that we describe 2Q-R^3-2D as its own type of spectroscopy in the main text. However, the signal is also considered an artefact distorting PP or R^3-2D signals in the pule overlap region due to "incorrect" pulse ordering, as described in detail in Ref. [85].

artefacts[16] are an additional challenge of the method, but can be reduced employing action detection as has been shown for fluorescence.[65] More importantly in the context of studying exciton interactions 2Q-R^3-2D has - contrary to the so far discussed methods - no population time and does not allow to track bi-exciton relaxation dynamics.

To observe decay dynamics in bi-exciton states, they need to be populated during a time window which tracks the system's relaxation dynamics, such as *e.g.* t_2 in PP. This is usually achieved by employing laser pulses at elevated power levels.[77,14,15] In this way additional field interactions, *e.g.* $\vec{K}_1 - \vec{K}_1$, arise along $\vec{K}_{PP} = +\vec{K}_1 - \vec{K}_1 + \vec{K}_3$ phase matching directions and these power dependent perturbations contain information about multi-exciton states. However, they are intertwined with pathways sensitive to transport, which renders the study of exciton interaction difficult. Furthermore, such an approach can trigger many unwanted processes such as photobleaching or multi-photon transitions which also complicates data analysis.

Fifth-order two-dimensional electronic spectroscopy (R^5-2D), initially suggested by Brüggemann *et al*,[17] is a modern experimental technique that avoids all of the above shortcomings as bi-exciton relaxation dynamics, such as EEA, contribute to the signal already at perturbative pump powers. The coherent signal field is detected along the $\vec{K}_{R5-R,R5-NR} = \mp 2\vec{K}_1 \pm 2\vec{K}_2 + \vec{K}_3$ phase matching directions such that the first/second pulse interacts twice with the sample and the third pulse once. This method thus probes the rather specific fifth-order response function $R^5(0, t_1, 0, t_2, t_3)$ and the signal is displayed similar to R^3-2D as a two dimensional map ($t_{1,3} \rightarrow \Omega_{1,3}$) in mixed time-frequency domain $\tilde{R}^5(\Omega_1, t_2, \Omega_3)$. The double-sided Feynman diagrams contributing to the signal are depicted in Fig. 2.7: The signal evolves, contrary to 2Q-R^3-2D, in a 2Q-coherence already in the t_1 interval representing an experimental advantage, as previously discussed. The double interaction with the second pulse leads to the system being in a ground, single- or bi-exciton population/coherence during t_2. We thus additionally classified the pathways depicted in Fig. 2.7 in contributions related to single and bi-exciton dynamics. The last interaction creates a coherence which acts as a source term for the emitted signal. Thus even in fifth-order both single and bi-exciton transport contribute to the signal, which at a first glance may appear as a downside of the technique, somewhat analogously to the obstacles discussed when employing intense laser pulses. However, there are several ways to identify bi-exciton dynamics depending on context, as we will discuss in the following.

Dostál *et al.*[18] were the first to experimentally implement R^5-2D in PP geometry. They used R^5-2D spectra of perylene based J-aggregates to correct for annihilation-

(a)

$2k_1$-$2k_2$+k_3:	GSB	ESA		SE		SE ESA
t_2 dynamics	/	Coherence l≠m	Transport m→n	Coherence i≠j	Transport l→m	Exciton Exciton Annihilation
bi-exciton dynamics	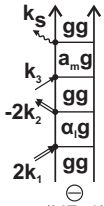 (NR 1)	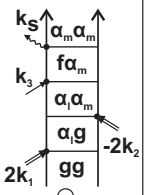 (NR 2)	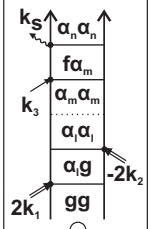 (NR 3)	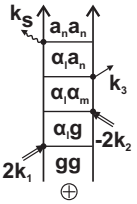 (NR 4)	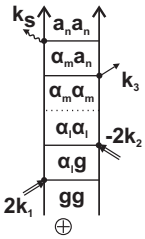 (NR 5)	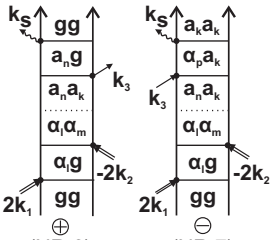 (NR 6) (NR 7)
single-exciton dynamics		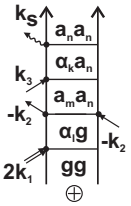 (NR 8)	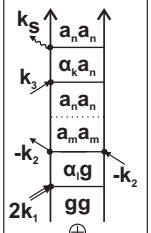 (NR 9)	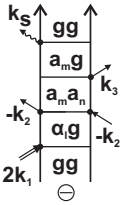 (NR 10)	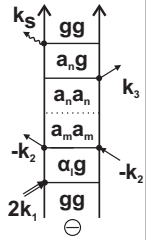 (NR 11)	Energy level diagram 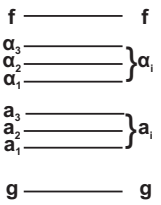

(b)

$-2k_1$+$2k_2$+k_3:	GSB	ESA		SE		SE ESA
t_2 dynamics	/	Coherence l≠m	Transport l→m	Coherence l≠m	Transport l→m	Exciton Exciton Annihilation
bi-exciton dynamics	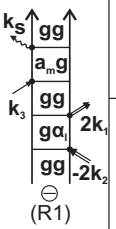 (R1)	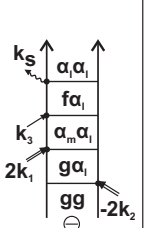 (R2)	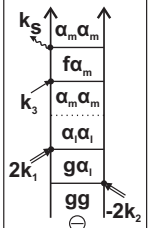 (R3)	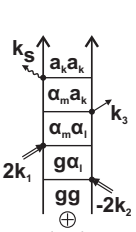 (R4)	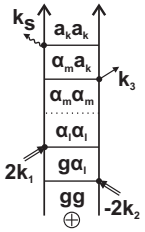 (R5)	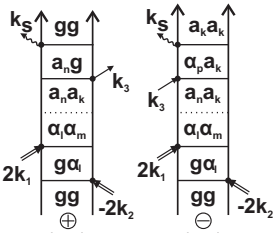 (R6) (R7)
single-exciton dynamics		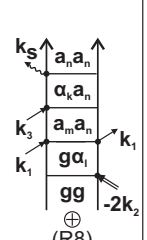 (R8)	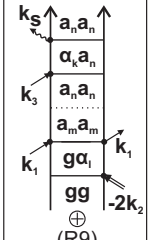 (R9)	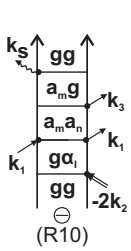 (R10)	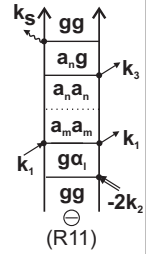 (R11)	Energy level diagram 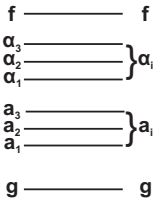

Figure 2.7.: Double-sided Feynman diagrams for non-rephasing (a) and rephasing (b) R^5-2D. Ground, single, bi-, tri-exciton states are denoted with $|g\rangle$, $|a_i\rangle$, $|\alpha_i\rangle$ and $|f\rangle$, respectively. Reprinted from [1].

related contributions in - with elevated pump powers measured - R^3-2D spectra of the same system. Their procedure led to a better signal-to-noise ratio of the proper annihilation-free third-order signal. Furthermore, Dostál *et al.* were the first to argue that integrating the R^5-2D map over both Ω_1 and Ω_3 frequencies allows to directly and exclusively track annihilation dynamics without the need to study the intensity dependence of the signal. In their study they employed the spectrally integrated R^5-2D signal to investigate diffusion limited annihilation dynamics and retrieved exciton diffusion constants by describing the signal with a diffusion equation. While Dostál *et al.* argued for a general applicability of the integrated signal to exclusively study annihilation dynamics, we formally proved in Ref. [1] that pathways sensitive to exciton transport (see Fig. 2.7) identically vanish from the integrated signal if the studied molecular aggregate has aligned transition dipoles with identical magnitude, independent of the transport regime (Förster[89] or Redfield[90]).

Our analysis is based on a developed dynamical model[1] of R^5-2D which includes both exciton transport and annihilation *via* a master equation formalism. The model employs two-level chromophores and omits details of EEA such as the separate processes of exciton fusion and internal conversion. Inclusion of the latter two would require to model an additional transient state after fusion at each chromophore - as discussed *e.g.* by May[9] - and to develop a proper description of internal conversion. Instead we use a phenomenological rate for the entire annihilation kinetics, and several advantages come from such a simplification. First, we have been able to construct analytically tractable heterodimer models based on the two-level chromophore description; with an additional third level on each chromophore heterodimer dynamics are not reasonably tractable analytically. Due to the novelty of the R^5-2D signal, lean analytical expressions greatly facilitate the interpretation of the obtained results and allow for an in depth understanding of the simulations and the signal itself. Second, the transient state is often dark and without direct spectroscopic signatures.[84] Its inclusion therefore does not alter the main conclusions of paper [1], *i.e.* the derived theorem that the spectrally integrated R^5-2D signal of aligned molecular aggregates is constant for exciton conserving dynamics. The integrated signal thus provides a robust methodology to study EEA in these systems. In terms of possible extensions of the model, the additional transient state can be straightforwardly included along with other spectroscopic features, such as *e.g.* vibronic progressions.

We applied the model to analyse the R^5-2D signal of a non-aligned squaraine homotrimer, measured with a developed fully non-collinear R^5-2D setup.[2] From analysing

the signal structure we identified a single peak as a reporter on EEA inside the bent squaraine homotrimer and extend the applicability of R^5-2D to study annihilation in non-aligned molecular aggregates. In particular, we extracted an ultrafast annihilation rate of 30 fs. The measured lineshapes of the trimer additionally displayed interesting details such as a clearly recognizable nodal line tilt and signs of dynamic disorder. The latter two were, however, beyond the Markovian master equation model[1] employed to analyse the signal. In subsequent work[4] we thus developed and applied lineshape analysis to R^5-2D and showed that R^5-2D lineshapes contain essential information about the coordination of spectral fluctuations of nearby molecules such as the sign and amount of inter-site correlations and the strength of bi-exciton binding energy fluctuations. These results illustrate an important application of R^5-2D as a large body of work in R^5-2D focused on the extraction of annihilation dynamics but omitted a detailed lineshape analysis.

In parallel to our work, Malý *et al.*[19] developed a master equation approach to R^5-2D, based on three-level chromophores, to describe the dynamics of the spectrally integrated R^5-2D signal of squaraine copolymers and argued that exciton transport through such systems occurs *via* sub-diffusive motion. They additionally employed their model to show, in a theoretical study, that a measurement of anisotropy in the integrated signal allows to obtain information about the structure of the studied molecule.[91] Besides the herein discussed coherent method they also realized incoherently detected R^5-2D along $\Phi_{R5-2D} = \mp 2\Phi_1 \pm 2\Phi_2 + \Phi_3 - \Phi_4$ (diagrams can be found in Ref. [92]) for fluorescence.[92] We will revisit the action detected variant of R^5-2D in section 4 when we describe an experimental setup currently build at TUM which allows to incoherently detect R^5-2D employing photocurrent detection.

3. Publications

All research articles serving as the basis for this publication-based thesis are summarized in this chapter. The individual contributions of each author are clearly stated. Reprints of the original articles and supporting informations are provided in the Appendix, with permission of the respective journal.

3.1. Interplay of Exciton Annihilation and Transport in Fifth Order Electronic Spectroscopy

C. Heshmatpour, J. Hauer, and F. Šanda
Chemical Physics, 528:110433, 2020.
DOI: 10.1016/j.chemphys.2019.110433

3.1.1. Summary and Classification within the Thesis

Fifth order multidimensional electronic spectroscopy (R^5-2D), detected along $\mp 2\vec{K}_1 \pm 2\vec{K}_2 + \vec{K}_3$ phase matching directions, was found sensitive to bi-exciton dynamics[17,18] in particular to the process of EEA.[8] The general temporal evolution of the signal is, however, comprised of a non-trivial interference between transport and annihilation contributions. In this publication we investigate this interference in spectra of small molecular aggregates by employing a master equation approach to both EEA and exciton transport. The signal is additionally discussed in the limit of both strong[90] and weak[89] exciton coupling by applying the related transport theories.

We specifically apply the developed model to predict lineshapes and peak volume dynamics of coupled molecular dimers and trimers with aligned transition dipoles. In the dimer case, analytical solutions are obtained for both lineshapes and peak volume dynamics. Whereas heterodimers display a complicated interference in lineshape and peak volume dynamics, the situation becomes more transparent for homodimers: in particular, we show that the spectral integration of homodimer R^5-2D signals over both excitation and emission frequencies eliminates the dependence on single exciton transport rates and results in a direct measurement of the annihilation rate, independent of the transport regime. We discuss possible extension of this result on larger aggregates and formally proof that this statement holds for aligned homoaggregates of arbitrary length, such that the integrated signal represents a general methodology to study annihilation under weak excitation conditions in such systems.

To exemplify the above point we analyse aligned molecular homotrimers: for weak coupling, *i.e.* incoherent transport, we predict a clear bi-exponential decay separating diffusion limited from ultrafast annihilation dynamics. In the strong coupling regime exciton delocalization blocks this separation and the integrated signal decays single-exponentially dominated by the ultrafast annihilation component.

The model developed in this work provides the basis for the following publications.

Individual Contributions

The presented model was developed and numerically implemented by C. Heshmatpour under the guidance of F. Šanda. The simulations were analysed by C. Heshmatpour in close collaboration with F. Šanda. C. Heshmatpour derived all analytical results with the exception of the results presented in Appendix C which where derived by F. Šanda. The manuscript was written by C. Heshmatpour and edited by F. Šanda and J. Hauer. All figures were created by C. Heshmatpour.

3.2. Annihilation Dynamics of Molecular Excitons Measured at a Single Perturbative Excitation Energy

C. Heshmatpour, P. Malevich, F. Plasser, M. Menger, C. Lambert, F. Šanda, and J. Hauer

The Journal of Physical Chemistry Letters, 11(18):7776–7781, 2020.
DOI: 10.1021/acs.jpclett.0c02141

3.2.1. Summary and Classification within the Thesis

We apply the modern spectroscopic tool of R^5-2D to determine exciton-exciton annihilation (EEA) dynamics in a squaraine homotrimer. We chose the latter as a test system of tractable size to be described by the model developed in Ref. [1]. EEA is an essential many-body process found in a wide range of excitonic systems. Regardless of its importance, the accurate determination of EEA still poses a spectroscopic problem. Conventionally, EEA is measured as a deviation from linearity in the intensity dependence of photoluminescence or transient absorption signals. This means that other high-intensity effects such as photobleaching or the onset of multiphoton transitions will drastically complicate a thorough data analysis.

In this joint experimental and theoretical work, we show that R^5-2D avoids these problems elegantly by selective excitation of bi-exciton states. In previous works,[18,19,1] the attention was focused on the spectrally integrated signal to study annihilation dynamics in aligned aggregates. We describe the more general case of non-aligned structures and simulate the complete lineshapes. Based on an analysis employing double-sided Feynman diagrams and explicit simulations we identify a well-isolated peak in the R^5-2D homotrimer spectrum as a direct and background-free reporter on EEA. The respective peak shows an ultrafast rise from which we extract an annihilation timescale of 30 fs in the trimer under investigation. This means that R^5-2D allows for an unambiguous determination of EEA timescales at a single, perturbative excitation density.

Individual Contributions

The presented experimental data was recorded and processed by P. Malevich under the guidance of J. Hauer. The processed data was analysed and modelled by C. Heshmatpour under the guidance of F. Šanda and J. Hauer. C. Heshmatpour derived all analytical

results. The molecular structure was calculated by F. Plasser. The excitonic couplings and transition dipole moment directions were calculated by M. Menger. The sample was provided by C. Lambert. The manuscript and supporting information were written by C. Heshmatpour and edited by P. Malevich, F. Šanda and J. Hauer. All figures were created by C. Heshmatpour, except Fig. S1 which was created by P. Malevich.

3.3. Correlated spectral fluctuations quantified by lineshape analysis of fifth order two-dimensional electronic spectra

C. Heshmatpour, J. Hauer, and F. Šanda
The Journal of Chemical Physics, 156(8):084114 (2022)
DOI: 10.1063/5.0081053

3.3.1. Summary and Classification within the Thesis

The analysis of two-dimensional lineshapes dynamics in third-order spectroscopies (R^3-2D) allows for the characterization of disorder and relaxation dynamics in molecules and condensed matter. R^5-2D is a modern and highly specialized variant of multidimensional electronic spectroscopy which was recently established as a feasible tool for probing bi-exciton dynamics in molecular aggregates. In this contribution we expand the capabilities of the method primarily designed to study exciton annihilation toward spectral fluctuation dynamics in molecular aggregates by developing and applying lineshape analysis in R^5-2D.

We noticed tilted nodal lines in peaks of R^5-2D spectra of squaraine trimers in Ref.[2] but had to omit their detailed analysis as it went beyond the applied master equation model. In this work we thus extend the model of Ref.[1] to include lineshape dynamics in R^5-2D signals of small molecular aggregates *via* slow spectral fluctuations, approximated by a classical stochastic Gaussian modulation. We provide an extensive analysis of predicted R^5-2D homodimer lineshapes and demonstrate, by an analytical treatment of the underlying fluctuation statistics, that they contain essential information about the coordination between spectral fluctuations of the two monomers. In particular we find the peak tilt to be a witness to both the amount of inter-site correlation and the strength of bi-exciton binding energy fluctuations. Possible coordination of close chromophores and its role in excitation transport through the complexes of chlorophylls is a debated topic in the light-harvesting community;[53] similarly, it was shown that the inclusion of fluctuations in bi-exciton binding energies is essential for the correct description of nonlinear lineshapes of photosynthetic reaction centers at low temperatures.[93] However, bi-exciton binding energy fluctuations are neglected in standard treatments to reduce the number of independent model parameter for fluctuations in the second manifold. In this contribution we show that they have a clear spectral signature, namely a strong

peak tilt in the homodimer spectrum. This means that R^5-2D lineshapes are perfectly fitting tools to describe fluctuations of single- and bi-exciton manifolds.

Individual Contributions

The presented model was developed and numerically implemented by C. Heshmatpour under the guidance of F. Šanda. The simulations were analysed by C. Heshmatpour in close collaboration with F. Šanda. C. Heshmatpour derived all analytical results. The manuscript was written by C. Heshmatpour and edited by F. Šanda and J. Hauer. All figures were created by C. Heshmatpour.

4. Conclusion and Outlook

EEA is an essential many-body process found in a wide range of excitonic systems. Despite its importance, an accurate parametrization of annihilation poses a spectroscopic problem. In 1Q-methods such as *e.g.* PP the annihilation rates are only measurable indirectly, as an intensity dependent perturbation intertwined with exciton transport dynamics. R^5-2D is a recent spectroscopic method filling the void left behind by common time-resolved techniques as bi-exciton states are addressed directly, providing background-free insights into their relaxation dynamics.

In this dissertation we contributed to the field of R^5-2D spectroscopy by the following:

1. We developed and numerically implemented a theoretical description of R^5-2D signals of small non-aligned molecular aggregates. The model includes all relevant relaxation mechanisms (intraband relaxation and EEA), and additionally allows to simulate non-trivial lineshapes and their dynamics. The latter makes our model unique in the context of models developed for R^5-2D spectroscopy.

2. We provided an extensive analysis of the peak structure and peak volume dynamics of R^5-2D dimer and trimer signals.

3. For aligned homoaggregates of arbitrary length, we formally proofed that annihilation dynamics exclusively determine their spectrally integrated R^5-2D signal. This explains why R^5-2D is a perfectly suited method for the description of ultrafast annihilation timescales.

4. We measured and modelled the ultrafast initial annihilation rate of 30 fs in a bent squaraine trimer.

5. To go beyond the ability of R^5-2D to track annihilation dynamics, we developed and applied R^5-2D lineshape analysis. We demonstrated that such lineshapes contain valuable information about fluctuation dynamics on both single- and bi-exciton manifolds. This is a new application for R^5-2D spectroscopy with results of general importance, specifically for the study of photosynthetic excitons. Steady

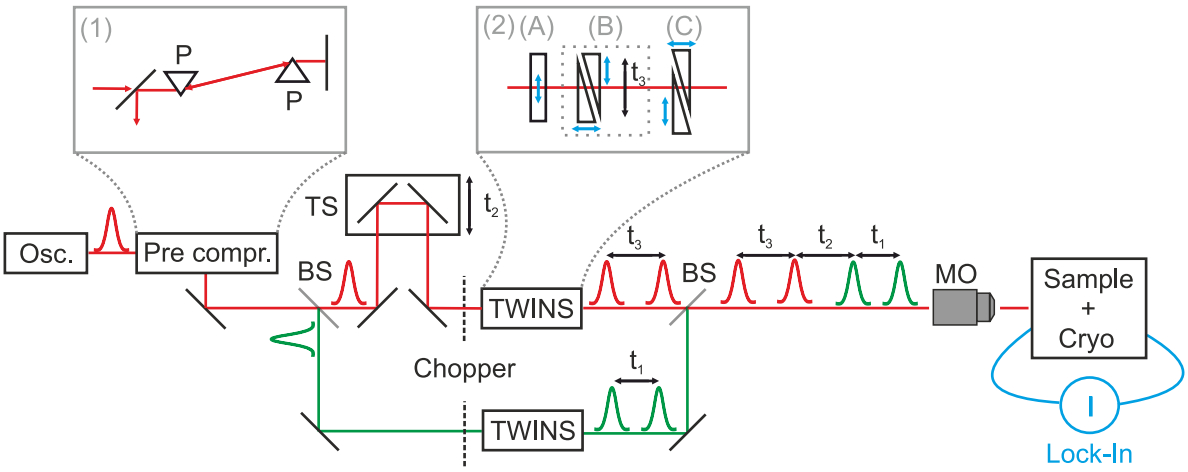

Figure 4.1.: Schematic of the proposed optical setup to measure time-resolved photocurrent excitation spectra. A detailed description is presented in the text. P: Prism, BS: Beam splitter, TS: Translation stage, MO: Microscope objective

state or third-order time-resolved methods deliver only indirect information about said fluctuation dynamics.

In future work we plan to measure and analyse R^5-2D spectra of two-dimensional materials, as EEA is a key process defining the efficiency of optoelectronic devices.[94] Contrary to the herein discussed coherent R^5-2D method we plan to build an incoherent R^5-2D experiment based on photocurrent (PC) detection, for which we already received funding from *e*-conversion. The PC detection provides the advantage that the optoelectronic devices can be tested directly under working conditions. Contrary to so far published time-resolved PC experiments our implementation of time-resolved PC spectroscopy will rest on the Translating-Wedge-based Identical pulse eNcoding System[95] (TWINS) as its interferometer instead of nested Mach-Zehnder interferometers.[58] A sketch of the prosed experimental setup is depicted in Fig. 4.1. The output of a laser source (preliminary tests performed with Ti:sapphire oscillator; repetition rate: 80 MHz, 800 nm central wavelength, 12 fs pulse duration) is pre-compressed by a standard prism compressor, consisting of two identical fused silica prisms (P) arranged as shown in inset (1) of Fig. 4.1: The incident pulse hits the prisms at Brewster angle and gets dispersed. A mirror which is slightly tilted downwards reflects the pulse back through both prisms, and it finally gets picked off by a mirror which is slightly below the incident beam. The prism compressor compensates for the group velocity dispersion introduced by the optical components in the beam path. The pulse is subsequently split by a 50:50 beamsplitter (BS) into a pump (green) and probe (red) arm. The probe pulse is delayed

by a time t_2 with respect to the pump pulse by a computer controlled linear motorized translation stage (TS). The two TWINS, subsequently create a phase locked pulse pair delayed by t_1 and t_3. TWINS exploits birefringence to generate these two pulse replicas with exceptionally high phase stability. The working principle is depicted in inset (2): a birefringent block (A) splits an input pulse with polarization set to 45°, with respect to the ordinary and extraordinary (indicated by blue arrows) axes of the crystal, into two perpendicularly polarized pulses delayed in time. The time delay is defined by its thickness. The second block (B) consists of one wedge with extraordinary axis rotated by 90° with respect to block (A), and one wedge identically orientated to block (A). This block can be moved as complete unit, and can thus reverse the time delay introduced by block (A). The pulses are slightly front tilted and non-collinear after passing through block (B), which is corrected by block (C). More details can be found in Ref. [95]. The small footprint of the TWINS allows the setup to be rather compact, and moreover we have additionally shown that the TWINS are ideally suited to record PC excitation spectra over a broad wavelength range.[3] The proposed setup allows to record both R^3-2D and R^5-2D photocurrent spectra. The latter is measured by scanning the t_1 delay sufficiently far and with the appropriate step size such that the 2Q- coherences can be resolved.

The work presented in thesis established that R^5-2D is an insightful and powerful tool to study annihilation and spectral fluctuation dynamics in molecular aggregates. In future work, we plan to employ R^5-2D spectroscopy not only on molecular systems but also on 2D semiconductors. The aim is the study of fundamental many-body processes in these fascinating materials with unprecedented time resolution.

Bibliography

[1] C. Heshmatpour, J. Hauer, and F. Šanda. Interplay of exciton annihilation and transport in fifth order electronic spectroscopy. *Chem. Phys.*, 528:110433, 2020.

[2] C. Heshmatpour, P. Malevich, F. Plasser, M. Menger, C. Lambert, F. Šanda, and J. Hauer. Annihilation dynamics of molecular excitons measured at a single perturbative excitation energy. *J. Phys. Chem. Lett.*, 11(18):7776–7781, 2020.

[3] L. Wolz, C. Heshmatpour, A. Perri, D. Polli, G. Cerullo, J. J. Finley, E. Thyrhaug, J. Hauer, and A. V. Stier. Time-domain photocurrent spectroscopy based on a common-path birefringent interferometer. *Rev. Sci. Instrum.*, 91(12):123101, 2020.

[4] C. Heshmatpour, J. Hauer, and F. Šanda. Correlated spectral fluctuations quantified by line shape analysis of fifth-order two-dimensional electronic spectra. *J. Chem. Phys.*, 156(8):084114, 2022.

[5] P. Malevich, C. Heshmatpour, H. Ceymann, M. H. Schreck, and J. Hauer. Molecular annihilation dynamics measured in the perturbative regime of excitation. *The 22nd International Conference on Ultrafast Phenomena 2020*, page Th2A.2, 2020.

[6] A. Gelzinis, D. Abramavicius, and L. Valkunas. Absorption lineshapes of molecular aggregates revisited. *J. Chem. Phys.*, 142(15):154107, 2015.

[7] S. Mukamel. *Principles of Nonlinear Optical Spectroscopy.* OUP, 1995.

[8] V. May and O. Kuhn. *Charge and Energy Transfer Dynamics in Molecular Systems.* WILEY-VCH Verlag, 2011.

[9] V. May. Kinetic theory of exciton–exciton annihilation. *J. Chem. Phys.*, 140(5):054103, 2014.

[10] Y. B. Gaididei and A. I. Onipko. A kinetic theory of incoherent exciton annihilation. *Mol. Cryst. Liq. Cryst.*, 62(3-4):213–235, 1979.

[11] Y. Yu, Y. Yu, C. Xu, A. Barrette, K. Gundogdu, and L. Cao. Fundamental limits of exciton-exciton annihilation for light emission in transition metal dichalcogenide monolayers. *Phys. Rev. B*, 93:201111, 2016.

[12] L. Tzabari, V. Zayats, and N. Tessler. Exciton annihilation as bimolecular loss in organic solar cells. *J. Appl. Phys.*, 114(15):154514, 2013.

[13] T. J. McDonough, L. Zhang, S. S. Roy, N. M. Kearns, M. S. Arnold, M. T. Zanni, and T. L. Andrew. Triplet exciton dissociation and electron extraction in graphene-templated pentacene observed with ultrafast spectroscopy. *Phys. Chem. Chem. Phys.*, 19:4809–4820, 2017.

[14] B. Brüggemann and V. May. Exciton exciton annihilation dynamics in chromophore complexes. II. Intensity dependent transient absorption of the LH2 antenna system. *J. Chem. Phys.*, 120(5):2325–36, 2004.

[15] L. Valkunas, Y. Z. Ma, and G. R. Fleming. Exciton-exciton annihilation in single-walled carbon nanotubes. *Phys. Rev. B*, 73:115432, 2006.

[16] V. Perlík, J. Hauer, and F. Šanda. Finite pulse effects in single and double quantum spectroscopies. *J. Opt. Soc. Am. B*, 34(2):430–439, 2017.

[17] B. Brüggemann and T. Pullerits. Nonperturbative modeling of fifth-order coherent multidimensional spectroscopy in light harvesting antennas. *New J. Phys.*, 13:025024, 2011.

[18] J. Dostál, F. Fennel, F. Koch, S. Herbst, F. Wurthner, and T. Brixner. Direct observation of exciton-exciton interactions. *Nat. Commun.*, 9:2466, 2018.

[19] P. Malý, J. Lüttig, A. Turkin, J. Dostál, C. Lambert, and T. Brixner. From wavelike to sub-diffusive motion: exciton dynamics and interaction in squaraine copolymers of varying length. *Chem. Sci.*, 11(2):456–466, 2020.

[20] A. S. Davydov. The theory of molecular excitons. *Sov. Phys. Uspekhi*, 7(2):145–178, 1964.

[21] T. Renger, V. May, and O. Kühn. Ultrafast excitation energy transfer dynamics in photosynthetic pigment–protein complexes. *Phys. Rep.*, 343(3):137–254, 2001.

[22] J. Frenkel. On the transformation of light into heat in solids. I. *Phys. Rev.*, 37:17–44, 1931.

[23] J. Frenkel. On the transformation of light into heat in solids. II. *Phys. Rev.*, 37:1276 – 1294, 1931.

[24] S. Tretiak, C. Middleton, V. Chernyak, and S. Mukamel. Exciton Hamiltonian for the bacteriochlorophyll system in the LH2 antenna complex of purple bacteria. *J. Phys. Chem. B*, 104(18):4519–4528, 2000.

[25] Frank C. Spano. The spectral signatures of frenkel polarons in H- and J-aggregates. *Acc. Chem. Res.*, 43(3):429–439.

[26] T. Renger, V. May, and O. Kühn. Ultrafast excitation energy transfer dynamics in photosynthetic pigment–protein complexes. *Phys. Rep.*, 343(3):137–254, 2001.

[27] F. Milota, J. Sperling, A. Nemeth, T. Mančal, and H. F. Kauffmann. Two-dimensional electronic spectroscopy of molecular excitons. *Acc. Chem. Res.*, 42(9):1364–1374, 2009.

[28] A. Classen, C. L. Chochos, L. Lüer, V. G. Gregoriou, J. Wortmann, A. Osvet, K. Forberich, I. McCulloch, T. Heumüller, and C. J. Brabec. The role of exciton lifetime for charge generation in organic solar cells at negligible energy-level offsets. *Nat. Energy*, 5(9):711–719, 2020.

[29] H.-G. Duan, A. L. Stevens, P. Nalbach, M. Thorwart, V. I. Prokhorenko, and R. J. D. Miller. Two-dimensional electronic spectroscopy of light-harvesting complex II at ambient temperature: a joint experimental and theoretical study. *J. Phys. Chem. B*, 119(36):12017–12027, 2015.

[30] G. S. Schlau-Cohen, A. Ishizaki, and G. R. Fleming. Two-dimensional electronic spectroscopy and photosynthesis: Fundamentals and applications to photosynthetic light-harvesting. *Chem. Phys.*, 386(1):1–22, 2011.

[31] D. Zigmantas, E. L. Read, T. Mančal, T. Brixner, A. T. Gardiner, R. J. Cogdell, and G. R. Fleming. Two-dimensional electronic spectroscopy of the B800–B820 light-harvesting complex. *Proc. Natl. Acad. Sci. U.S.A.*, 103(34):12672–12677, 2006.

[32] N. Christensson, F. Milota, A. Nemeth, J. Sperling, H. F. Kauffmann, T. Pullerits, and J. Hauer. Two-dimensional electronic spectroscopy of β-carotene. *J. Phys. Chem. B*, 113(51):16409–16419, 2009.

[33] R. Berera, R. van Grondelle, and J. T. Kennis. Ultrafast transient absorption spectroscopy: principles and application to photosynthetic systems. *Photosynth. Res.*, 101:105 – 118, 2009.

[34] R. Kubo. Statistical-mechanical theory of irreversible processes. I. General theory and simple applications to magnetic and conduction problems. *J. Phys. Soc. Jpn.*, 12:570, 1957.

[35] K. Blum. *Density Matrix Theory and Applications*. Springer Berlin, 2014.

[36] D. Abramavicius, B. Palmieri, D. V. Voronine, F. Šanda, and S. Mukamel. Coherent multidimensional optical spectroscopy of excitons in molecular aggregates; quasiparticle versus supermolecule perspectives. *Chem. Rev.*, 109:2350 – 2408, 2009.

[37] P. Hamm and M. T. Zanni. *Concepts and methods of 2D infrared spectroscopy*. C.U.P., New York, 2011.

[38] U. Megerle, I. Pugliesi, C. Schriever, C. F. Sailer, and E. Riedle. Sub-50 fs broadband absorption spectroscopy with tunable excitation: putting the analysis of ultrafast molecular dynamics on solid ground. *Appl. Phys. B*, 96(2-3):215–231, 2009.

[39] S. A. Kovalenko, A. L. Dobryakov, J. Ruthmann, and N. P. Ernsting. Femtosecond spectroscopy of condensed phases with chirped supercontinuum probing. *Phys. Rev. A*, 59:2369–2384, 1999.

[40] I. H.M. van Stokkum, D. S. Larsen, and R. van Grondelle. Global and target analysis of time-resolved spectra. *Biochim. Biophys. Acta*, 1657(2-3):82–104, 2004.

[41] S. Mukamel. Multidimensional femtosecond correlation spectroscopies of electronic and vibrational excitations. *Annu. Rev. Phys. Chem.*, 51(1):691–729, 2000.

[42] D. M. Jonas. Two-dimensional femtosecond spectroscopy. *Annu. Rev. Phys. Chem.*, 54:425 – 463, 2003.

[43] E. L. Read, G. S. Engel, T. R. Calhoun, T. Mancal, T. K. Ahn, R. E. Blankenship, and G. R. Fleming. Cross-peak-specific two-dimensional electronic spectroscopy. *Proc. Natl. Acad. Sci. U.S.A.*, 104(36):14203–14208, 2007.

[44] F. Šanda, V. Perlík, C. N. Lincoln, and J. Hauer. Center line slope analysis in two-dimensional electronic spectroscopy. *J. Phys. Chem. A*, 119(44):10893, 2015.

[45] James Lim, David Paleček, Felipe Caycedo-Soler, Craig N. Lincoln, Javier Prior, Hans von Berlepsch, Susana F. Huelga, Martin B. Plenio, Donatas Zigmantas, and Jürgen Hauer. Vibronic origin of long-lived coherence in an artificial molecular light harvester. *Nat. Commun.*, 6(1), 2015.

[46] D. Zigmantas, E. L. Read, T. Mancal, T. Brixner, A. T. Gardiner, R. J. Cogdell, and G. R. Fleming. Two-dimensional electronic spectroscopy of the B800-B820 light-harvesting complex. *Proc. Natl. Acad. Sci. U.S.A.*, 103(34):12672–12677, 2006.

[47] M. W. Graham, T. R. Calhoun, A. A. Green, M. C. Hersam, and G. R. Fleming. Two-dimensional electronic spectroscopy reveals the dynamics of phonon-mediated excitation pathways in semiconducting single-walled carbon nanotubes. *Nano Lett.*, 12(2):813–819, 2012.

[48] R. D. Mehlenbacher, T. J. McDonough, M. Grechko, M.-Y. Wu, M. S. Arnold, and M. T. Zanni. Energy transfer pathways in semiconducting carbon nanotubes revealed using two-dimensional white-light spectroscopy. *Nat. Commun.*, 6(1), 2015.

[49] V. R. Policht, M. Russo, F. Liu, C. Trovatello, M. Maiuri, Y. Bai, X. Zhu, S. Dal Conte, and G. Cerullo. Dissecting interlayer hole and electron transfer in transition metal dichalcogenide heterostructures via two-dimensional electronic spectroscopy. *Nano Lett.*, 21(11):4738–4743, 2021.

[50] L. P. DeFlores, R. A. Nicodemus, and A. Tokmakoff. Two-dimensional fourier transform spectroscopy in the pump-probe geometry. *Opt. Lett.*, 32(20):2966, 2007.

[51] F. D. Fuller and J. P. Ogilvie. Experimental implementations of two-dimensional fourier transform electronic spectroscopy. *Annu. Rev. Phys. Chem.*, 66(1):667–690, 2015.

[52] P. F. Tekavec, J. A. Myers, K. L. M. Lewis, and J. P. Ogilvie. Two-dimensional electronic spectroscopy with a continuum probe. *Opt. Lett.*, 34(9):1390, 2009.

[53] J. Cao, R. J. Cogdell, D. F. Coker, H.-G. Duan, J. Hauer, U. Kleinekathöfer, T. L. C. Jansen, T. Mančal, R. J. D. Miller, J. P. Ogilvie, V. I. Prokhorenko, T. Renger, H.-S. Tan, R. Tempelaar, M. Thorwart, E. Thyrhaug, S. Westenhoff, and D. Zigmantas. Quantum biology revisited. *Sci. Adv.*, 6(14), 2020.

[54] P. M. Donaldson, H. Strzalka, and P. Hamm. High sensitivity transient infrared spectroscopy: a UV/visible transient grating spectrometer with a heterodyne detected infrared probe. *Opt. Express*, 20(12):12761, 2012.

[55] T. Brixner, T. Mančal, I. V. Stiopkin, and G. R. Fleming. Phase-stabilized two-dimensional electronic spectroscopy. *J. Chem. Phys.*, 121(9):4221–4236, 2004.

[56] S.-H. Shim and M. T. Zanni. How to turn your pump–probe instrument into a multidimensional spectrometer: 2d IR and vis spectroscopiesvia pulse shaping. *Phys. Chem. Chem. Phys.*, 11(5):748–761, 2009.

[57] M. Orrit and J. Bernard. Single pentacene molecules detected by fluorescence excitation in ap-terphenyl crystal. *Phys. Rev. Lett.*, 65(21):2716–2719, 1990.

[58] G. Nardin, T. M. Autry, K. L. Silverman, and S. T. Cundiff. Multidimensional coherent photocurrent spectroscopy of a semiconductor nanostructure. *Opt. Express*, 21(23):28617, 2013.

[59] K. J. Karki, J. R. Widom, J. Seibt, I. Moody, M. C. Lonergan, T. Pullerits, and A. H. Marcus. Coherent two-dimensional photocurrent spectroscopy in a PbS quantum dot photocell. *Nat. Commun.*, 5(1), 2014.

[60] M. Aeschlimann, T. Brixner, A. Fischer, C. Kramer, P. Melchior, W. Pfeiffer, C. Schneider, C. Strüber, P. Tuchscherer, and D. V. Voronine. Coherent two-dimensional nanoscopy. *Science*, 333(6050):1723–1726, 2011.

[61] S. Roeding and T. Brixner. Coherent two-dimensional electronic mass spectrometry. *Nat. Commun.*, 9(1), 2018.

[62] P. Malý, J. Lüttig, S. Mueller, M. H. Schreck, C. Lambert, and T. Brixner. Coherently and fluorescence-detected two-dimensional electronic spectroscopy: direct comparison on squaraine dimers. *Phys. Chem. Chem. Phys.*, 22(37):21222–21237, 2020.

[63] P. F. Tekavec, T. R. Dyke, and A. H. Marcus. Wave packet interferometry and quantum state reconstruction by acousto-optic phase modulation. *J. Chem. Phys.*, 125(19):194303, 2006.

[64] S. Fu, A. Sakurai, L. Liu, F. Edman, T. Pullerits, V. Öwall, and K. J. Karki. Generalized lock-in amplifier for precision measurement of high frequency signals. *Rev. Sci. Instrum.*, 84(11):115101, 2013.

[65] S. Mueller, S. Draeger, X. Ma, M. Hensen, T. Kenneweg, W. Pfeiffer, and T. Brixner. Fluorescence-detected two-quantum and one-quantum–two-quantum 2D electronic spectroscopy. *J. Phys. Chem. Lett.*, 9(8):1964–1969, 2018.

[66] P. Malý and T. Brixner. Fluorescence-detected pump–probe spectroscopy. *Angew. Chem. Int. Ed.*, 60(34):18867–18875, 2021.

[67] P. Malý and T. Mančal. Signatures of exciton delocalization and exciton–exciton annihilation in fluorescence-detected two-dimensional coherent spectroscopy. *J. Phys. Chem. Lett.*, 9(19):5654–5659, 2018.

[68] V. Tiwari, Y. A. Matutes, A. T. Gardiner, T. L. C. Jansen, R. J. Cogdell, and J. P. Ogilvie. Spatially-resolved fluorescence-detected two-dimensional electronic spectroscopy probes varying excitonic structure in photosynthetic bacteria. *Nat. Commun.*, 9(1), 2018.

[69] K. J. Karki, J. Chen, A. Sakurai, Q. Shi, A. T. Gardiner, O. Kühn, R. J. Cogdell, and T. Pullerits. Before Förster. Initial excitation in photosynthetic light harvesting. *Chem. Sci.*, 10(34):7923–7928, 2019.

[70] E. Harel and G. S. Engel. Quantum coherence spectroscopy reveals complex dynamics in bacterial light-harvesting complex 2 (LH2). *Proc. Natl. Acad. Sci. U.S.A.*, 109(3):706–711, 2012.

[71] M. Ferretti, R. Hendrikx, E. Romero, J. Southall, R. J. Cogdell, V. I. Novoderezhkin, G. D. Scholes, and R. van Grondelle. Dark states in the light-harvesting complex 2 revealed by two-dimensional electronic spectroscopy. *Sci. Rep.*, 6(1), 2016.

[72] O. Kühn, T. Mančal, and T. Pullerits. Interpreting fluorescence detected two-dimensional electronic spectroscopy. *J. Phys. Chem. Lett.*, 11(3):838–842, 2020.

[73] T. Kunsel, V. Tiwari, Y. A. Matutes, A. T. Gardiner, R. J. Cogdell, J. P. Ogilvie, and T. L. C. Jansen. Simulating fluorescence-detected two-dimensional electronic spectroscopy of multichromophoric systems. *J. Phys. Chem. B*, 123(2):394–406, 2018.

[74] M. A. Baldo, R. J. Holmes, and S. R. Forrest. Prospects for electrically pumped organic lasers. *Phys. Rev. B*, 66:035321, 2002.

[75] E. Linardy, D. Yadav, D. Vella, I. A. Verzhbitskiy, K. Watanabe, T. Taniguchi, F. Pauly, M. Trushin, and G. Eda. Harnessing exciton-exciton annihilation in two-dimensional semiconductors. *Nano Lett.*, 20(3):1647–1653, 2020.

[76] M. G. Muller, P. Lambrev, M. Reus, E. Wientjes, R. Croce, and A. R. Holzwarth. Singlet energy dissipation in the photosystem II light-harvesting complex does not involve energy transfer to carotenoids. *ChemPhysChem*, 11:1289 – 1296, 2010.

[77] L. Valkunas, I. H. M. van Stokkum, R. Berera, and R. van Grondelle. Exciton migration and fluorescence quenching in LHCII aggregates: Target analysis using a simple nonlinear annihilation scheme. *Chem. Phys.*, 357:17 – 20, 2009.

[78] G. Trinkunas, J. L. Herek, T. Polivka, V. Sundstrom, and T. Pullerits. Exciton delocalization probed by excitation annihilation in the light-harvesting antenna LH2. *Phys. Rev. Lett.*, 86:4167 – 4170, 2001.

[79] L. Valkunas, G. Trinkunas, V. Liuolia, and R. van Grondelle. Nonlinear annihilation of excitations in photosynthetic systems. *Biophys. J.*, 69:1117 – 1129, 1995.

[80] F. Fennel and S. Lochbrunner. Exciton-exciton annihilation in a disordered molecular system by direct and multistep förster transfer. *Phys. Rev. B*, 92(14), 2015.

[81] T. Q. Nguyen, I. B. Martini, J. Liu, and B. J. Schwartz. Controlling interchain interactions in conjugated polymers: The effects of chain morphology on exciton-exciton annihilation and aggregation in MEH-PPV films. *J. Phys. Chem. B*, 104(2):237–255, 2000.

[82] T. Pullerits, M. Chachisvilis, and V. Sundström. Exciton delocalization length in the B850 antenna of rhodobacter sphaeroides. *J. Phys. Chem.*, 100(25):10787–10792, 1996.

[83] B. Brüggemann, J. L. Herek, V. Sundström, T. Pullerits, and V. May. Microscopic theory of exciton annihilation: application to the LH2 antenna system. *J. Phys. Chem. B*, 105(46):11391–11394, 2001.

[84] B. Brüggemann, N. Christensson, and T. Pullerits. Temperature dependent exciton–exciton annihilation in the LH2 antenna complex. *Chem. Phys.*, 357(1-3):140–143, 2009.

[85] D. Paleček, P. Edlund, E. Gustavsson, S. Westenhoff, and D. Zigmantas. Potential pitfalls of the early-time dynamics in two-dimensional electronic spectroscopy. *J. Chem. Phys.*, 151(2):024201, 2019.

[86] A. Nemeth, F. Milota, T. Mančal, T. Pullerits, J. Sperling, J. Hauer, H. F. Kauffmann, and N. Christensson. Double-quantum two-dimensional electronic spectroscopy of a three-level system: Experiments and simulations. *J. Chem. Phys.*, 133(9):094505, 2010.

[87] K. W. Stone, K. Gundogdu, D. B. Turner, X. Li, S. T. Cundiff, and K. A. Nelson. Two-quantum 2D FT electronic spectroscopy of biexcitons in GaAs quantum wells. *Science*, 324(5931):1169–1173, 2009.

[88] A. Nemeth, J. Sperling, J. Hauer, H. F. Kauffmann, and F. Milota. Compact phase-stable design for single- and double-quantum two-dimensional electronic spectroscopy. *Opt. Lett.*, 34(21):3301, 2009.

[89] T. Förster. Zwischenmolekulare Energiewanderung und Fluoreszenz. *Ann. Phys. (Berlin)*, 437:55 – 75, 1948.

[90] A. G. Redfield. On the theory of relaxation processes. *IBM J. Res. Dev.*, 1:19 – 31, 1957.

[91] J. Lüttig, T. Brixner, and P. Malý. Anisotropy in fifth-order exciton–exciton-interaction two-dimensional spectroscopy. *J. Chem. Phys.*, 154(15):154202, 2021.

[92] P. Malý, S. Mueller, J. Lüttig, C. Lambert, and T. Brixner. Signatures of exciton dynamics and interaction in coherently and fluorescence-detected four- and six-wave-mixing two-dimensional electronic spectroscopy. *J. Chem. Phys.*, 153(14):144204, 2020.

[93] O. Rancova, R. Jankowiak, and D. Abramavicius. Role of bath fluctuations in the double-excitation manifold in shaping the 2DES of bacterial reaction centers at low temperature. *J. Phys. Chem. B*, 122(4):1348, 2018.

[94] S. Deng, E. Shi, L. Yuan, L. Jin, L. Dou, and L. Huang. Long-range exciton transport and slow annihilation in two-dimensional hybrid perovskites. *Nat. Commun.*, 11(1), 2020.

[95] D. Brida, C. Manzoni, and G. Cerullo. Phase-locked pulses for two-dimensional spectroscopy by a birefringent delay line. *Opt. Lett.*, 37(15):3027, 2012.

Appendix

A. Full Length Article of Section 3.1

Chemical Physics 528 (2020) 110433

Contents lists available at ScienceDirect

Chemical Physics

journal homepage: www.elsevier.com/locate/chemphys

Interplay of exciton annihilation and transport in fifth order electronic spectroscopy

C. Heshmatpour[a,b], J. Hauer[b,c], F. Šanda[a,*]

[a] Institute of Physics, Faculty of Mathematics and Physics, Charles University, Ke Karlovu 5, Prague 121 16, Czech Republic
[b] Fakultät für Chemie, Technische Universität München, Lichtenbergstr. 4, D-85748 Garching b. München, Germany
[c] Photonics Institute, TU Wien, Gußhausstraße 27-29, 1040 Vienna, Austria

ARTICLE INFO

Keywords:
Exciton-exciton annihilation
Multidimensional electronic spectroscopy
Fifth order spectroscopy

ABSTRACT

Multidimensional fifth order spectroscopy is a sophisticated and specialized tool for probing bi-exciton dynamics. The complexity of the signals emitted into $\pm 2\vec{K}_1 \mp 2\vec{K}_2 + \vec{K}_3$ directions calls for a detailed theoretical treatment of 2D line shapes, including both exciton-exciton annihilation and intraband relaxation dynamics. Based on a master equation formalism, we discuss the signal's temporal evolution and clearly distinguish between intraband transport within first and second exciton manifolds. We prove analytically that signatures of single exciton transport vanish from spectrally integrated signals of parallel homo-aggregates of arbitrary length, while transport within the second manifold accounts for the diffusion limitations of annihilation. In an effort to model fifth order electronic spectra of tractably small systems, we develop a dynamical model for molecular dimers and trimers. We show that fifth order two-dimensional spectroscopy allows to track and pinpoint population transfer- and annihilation dynamics of bi-excitons, without the need to perform and analyse intensity dependent experiments.

1. Introduction

When two excitons are in close proximity to each other, they deactivate by fusion, followed by non-radiative relaxation. This process is referred to as exciton-exciton annihilation (EEA) [1]. EEA is an undesirable loss mechanism of excitation energy in lasers based on organic thin films [2] or polariton microcavities [3]. In other cases it serves a desirable functional purpose, e.g. it has a leading role in photoprotection of light harvesting complexes [4], or helps the formation of separated charges [5] or interchain species [6]. Due to the direct relation of EEA to the mobility of excitons, it is used to study diffusion lengths of excitons through molecular systems [7,8].

Dynamics of states involving multiple excitations cannot be probed directly by time resolved third order spectroscopic experiments such as pump probe [9] or two-dimensional electronic spectroscopy (2D-ES) [10]. EEA and related phenomena will rather show indirectly as intensity dependencies of time-resolved third-order signals [11–13]. Double quantum 2D-ES signal [14] offers the possibility to exclusively probe bi-excitonic coherences. Yet this specialized type of third order spectroscopy cannot probe bi-excitonic populations and their relaxation channels such as EEA.

Brüggemann *et al* [15] suggested certain fifth order coherent signals emitted into phase matching directions $\vec{K}_R = 2\vec{K}_1 - 2\vec{K}_2 + \vec{K}_3$ and $\vec{K}_{NR} = -2\vec{K}_1 + 2\vec{K}_2 + \vec{K}_3$, to track bi-exciton dynamics of the Fenna-Matthews-Olson light harvesting complex. Dostál *et al* [16] implemented this signal experimentally and studied large perylene based J-aggregates arguing that the integrated signal directly and specifically measures the exciton annihilation dynamics. More recently a theoretical study of Süß *et al* [17], discussed predictions of dimer spectra accounting also for instable local bi-excitons, which are rarely studied beyond a phenomenological description [1,18,19]. Herein, we refer to this specific fifth order technique as R^5-2D-ES.

In the present study, we theoretically investigate the R^5-2D-ES signal of small molecular aggregates (dimer, trimer) taking both intraband transport and EEA into account. We stay within the standard two level model for the chromophores, but investigate $\vec{K}_{NR}$ and $\vec{K}_R$ signals further by a detailed account of the exciton transport dynamics in the limits of both coherent excitonic motion and incoherent hopping of excitons. We thus present a quantum master equation approach for transport to incorporate both Redfield and Förster theory of excitonic transport. EEA is described by a similar master equation approach. In more detail, we ascribe rates for unidirectional transport to lower excitonic manifolds if two excitons are situated at adjacent sites. We thus

* Corresponding author.
E-mail address: sanda@karlov.mff.cuni.cz (F. Šanda).

https://doi.org/10.1016/j.chemphys.2019.110433
Received 26 April 2019; Received in revised form 1 July 2019; Accepted 1 July 2019
Available online 04 July 2019
0301-0104/

omit a detailed microscopic description of the bi-exciton transients and the sequence of processes from exciton fusion and initial localization of excitation energy on one site with its subsequent non-radiative relaxation outlined in reference [17]. We rather focus to investigate the effects of exciton transport processes on the signal.

The model is used to discuss the waiting time evolution of the R^5-2D-ES signal in both peak shapes and peak volumes. Of specific interest is the interference between various pathways of the R^5-2D-ES signal and the thereby resulting line shapes of individual peaks as a witness to EEA. We then provide a - to large extent analytical - treatment of peak volume dynamics, focusing on the role of intraband relaxation. The latter can be shown to contribute to R^5-2D-ES signal dynamics for the general case of a hetero aggregate. A spectrally integrated signal of a homo-aggregate, however, is exclusively determined by annihilation dynamics.

2. Model

2.1. Multidimensional line shapes of the fifth order response

We start by formulating the theory of 5th order spectra of N resonantly coupled molecules, each possessing two electronic energy levels. All calculations are performed in natural units where the Planck constant $\hbar$, the speed of light c and the Boltzmann constant k_B are set to one, *i. e.* $\hbar = c = k_B = 1$.

The non-linear response of a molecular system to a train of incident laser pulses, is calculated by employing Kubo theory [20,21]. It is based upon a perturbation expansion in the dipole interaction between a classical laser field $E(t)$ and a molecular aggregate, as described by the interaction Hamiltonian $\widehat{H}_{int}(t) = -\hat{\mu}\cdot E(t) + h.\,c.$. Herein, we consider a chain of N molecules and define the total dipole moment $\hat{\mu} = \sum_{n=1}^{N} d_n \widehat{B}_n^{\dagger}$, where d_n is the transition dipole moment of the n^{th} molecule and $\widehat{B}_n^{\dagger}$ ($\widehat{B}_n$) is the creation (annihilation) operator of an exciton at site n, obeying the Pauli commutation rule

$$[\widehat{B}_n, \widehat{B}_m^{\dagger}] = \delta_{nm}(1 - 2\widehat{B}_m^{\dagger}\widehat{B}_n). \tag{1}$$

To calculate the R^5-2D-ES signal, we evaluate the above described perturbative expansion up to the fifth order in the electric field $E(t)$. Even though the R^5-2D-ES signal is calculated from the fifth order response $\chi^{(5)}$, solely three excitation pulses are required for its generation. Signals emitted along the phase matching directions $\vec{K}_{NR} = -2\vec{K}_1 + 2\vec{K}_2 + \vec{K}_3$ and $\vec{K}_R = -2\vec{K}_2 + 2\vec{K}_1 + \vec{K}_3$ originate from a double interaction of the sample with the first/second pulse and a single interaction with the last pulse. In the impulsive limit, *i. e.* $E(t) = \sum_{j=1}^{3} E_j \delta(t - \tau_j)$, the signal thus depends only on intervals t_1, t_2 between the pules and interval t_3 for detection, *i. e.* $R^{(5)}(t_1, t_2, t_3) \equiv \chi^{(5)}(0, t_1, 0, t_2, t_3)$, and can be conveniently displayed analogously to standard third order 2D-ES correlation plots. Standard Green's function superoperator techniques [22] will be employed to calculate the non-rephasing signal

$$R_{NR}^{(5)}(t_1, t_2, t_3) = (i)^5 \langle\langle \mu | \breve{\mathscr{G}}(t_3)\breve{\mu}^{(+)}\breve{\mathscr{G}}(t_2)\breve{\mu}^{(+)}\breve{\mu}^{(+)}\breve{\mathscr{G}}(t_1)\breve{\mu}^{(-)}\breve{\mu}^{(-)}|gg\rangle\rangle \tag{2}$$

and rephasing signal

$$R_{R}^{(5)}(t_1, t_2, t_3) = (i)^5 \langle\langle \mu | \breve{\mathscr{G}}(t_3)\breve{\mu}^{(+)}\breve{\mathscr{G}}(t_2)\breve{\mu}^{(-)}\breve{\mu}^{(-)}\breve{\mathscr{G}}(t_1)\breve{\mu}^{(+)}\breve{\mu}^{(+)}|gg\rangle\rangle \tag{3}$$

emitted into phase matching directions $\vec{K}_{NR}$ and $\vec{K}_R$, respectively. Eqs. (2) and (3) are written in Liouville space [23,24] with inner product $\langle\langle A|B\rangle\rangle := \mathrm{Tr}\{A^{\dagger}B\}$. The dipole superoperator actions in Eqs. (2) and (3), $\breve{\mu}^{(+)} := \sum_{n=1}^{N} d_n(\breve{B}_{nl}^{\dagger} - \breve{B}_{nr}^{\dagger})$ and $\breve{\mu}^{(-)} := \sum_{n=1}^{N} d_n(\breve{B}_{nl} - \breve{B}_{nr})$, are defined with the use of left $\breve{B}_l|A\rangle\rangle := \widehat{B}\widehat{A}$ and right $\breve{B}_r|A\rangle\rangle := \widehat{A}\widehat{B}$ acting superoperators. The excitonic density matrix is initially in the ground state $|gg\rangle\rangle$.

Superoperator

$$\breve{\mathscr{G}}(t) = \exp((\breve{\mathscr{L}} + \breve{\mathscr{D}} + \breve{\mathscr{A}})t) \tag{4}$$

describes the temporal evolution of the excitonic density matrix $|\rho(t)\rangle\rangle = \breve{\mathscr{G}}(t)|\rho(0)\rangle\rangle$ between pulses, *i. e.* it is the Green's function solution to the excitonic master equation

$$\frac{\partial}{\partial t}|\rho(t)\rangle\rangle = (\breve{\mathscr{L}} + \breve{\mathscr{D}} + \breve{\mathscr{A}})|\rho(t)\rangle\rangle. \tag{5}$$

The generators of coherent evolution $\breve{\mathscr{L}}$, dissipative dynamics $\breve{\mathscr{D}}$ and EEA $\breve{\mathscr{A}}$, will be specified in Section 2.2. Eq. (5) assumes Markovian dynamics, memory effects and correlations between intervals (accountable by straightforward application of strategies developed for three interval response functions of third order 2D-ES [22,25]) are neglected here for simplicity.

The two signals defined by Eqs. (2) and (3) are conveniently displayed as two dimensional maps in mixed time-frequency domain defined as

$$\widetilde{R}_{NR}(\Omega_1, t_2, \Omega_3) := -\mathrm{Im}\left\{\int_0^{\infty} dt_1 \int_0^{\infty} dt_3 e^{i\Omega_1 t_1} e^{i\Omega_3 t_3} R_{NR}^{(5)}(t_1, t_2, t_3)\right\} \tag{6}$$

and

$$\widetilde{R}_{R}(\Omega_1, t_2, \Omega_3) := -\mathrm{Im}\left\{\int_0^{\infty} dt_1 \int_0^{\infty} dt_3 e^{-i\Omega_1 t_1} e^{i\Omega_3 t_3} R_{R}^{(5)}(t_1, t_2, t_3)\right\}. \tag{7}$$

Purely absorptive line shapes can be standardly obtained by summing both rephasing and non-rephasing signals

$$\widetilde{R}_{2D}(\Omega_1, t_2, \Omega_3) := \widetilde{R}_{R}(\Omega_1, t_2, \Omega_3) + \widetilde{R}_{NR}(\Omega_1, t_2, \Omega_3). \tag{8}$$

We note that the sign convention defined by Eqs. (2)–(8) (with *e. g.* negative sign for ground state bleach (GSB) contribution, see Fig. 1) corresponds to reference [15], while publications [16,17] opted for the opposite sign convention.

Expanding Eqs. (2) and (3) in excitonic indices the non-linear signals are summed up from a number of contributions

$$R_{R(NR)}^{(5)}(t_1, t_2, t_3) = \sum_i S_i(t_1, t_2, t_3), \tag{9}$$

called Liouville space pathways (LSP), standardly symbolized by double sided Feynman diagrams [21]. The complete classification of all LSP relevant for the present R^5-2D-ES signals, is given in Fig. 1. The summation at the right hand side of Eq. (9) runs over each specification of excitonic indices of each diagram drawn at Fig. 1a and Fig. 1b for $R_{NR}^{(5)}$ and $R_R^{(5)}$ signals, respectively.

The two-dimensional maps usually consist out of several peaks $P_j (j = 1, 2, ...)$. Information on relaxation and annihilation dynamics of excitons is conveniently retrieved from changes of peak volumes V_{P_j} which are standardly defined by integrating the response function $\widetilde{R}_{2D}(\Omega_1, t_2, \Omega_3)$ over a defined area in Ω_1 and Ω_3, *i. e.*

$$V_{P_j}(t_2) = \int_{\Omega_{1,j}^{min}}^{\Omega_{1,j}^{max}} d\Omega_1 \int_{\Omega_{3,j}^{min}}^{\Omega_{3,j}^{max}} d\Omega_3 \widetilde{R}_{2D}(\Omega_1, t_2, \Omega_3). \tag{10}$$

The limits of integration are chosen in a way that peak P_j is within the area of integration. A precise numeric integration of the peak volume may be challenging for overlapping peaks; an analytical treatment will even be impossible following Eq. (10) alone. As an alternative, we reworked Eq. (10) to make it suitable for calculations. Each peak P_j can be associated with a certain exclusive set X_j ($X_k \cap X_l = \varnothing$) of LSP in Fig. 1, with specific exciton indices. For instance pathway NR1 with $l = 1$ and $m = 2$ is associated only to peak at $(\Omega_1, \Omega_3) = (E_{\alpha_1} - E_g, E_{a_2} - E_g)$. In the calculation of the peak volume V_{P_j} we can thus restrict the summation in Eq. (9) over LSP of the set X_j, and in the same moment the limits of integration in Eq. (11) can be relaxed, *i. e.*

$$V_{P_j}(t_2) = \int_{-\infty}^{\infty} d\Omega_1 \int_{-\infty}^{\infty} d\Omega_3 \sum_{i \in X_j} \widetilde{S}_i(\Omega_1, t_2, \Omega_3). \tag{11}$$

Finally we note that Eq. (11) is the inverse Fourier transform evaluated at $t_{1,3} = 0$, *i. e.*

(a)

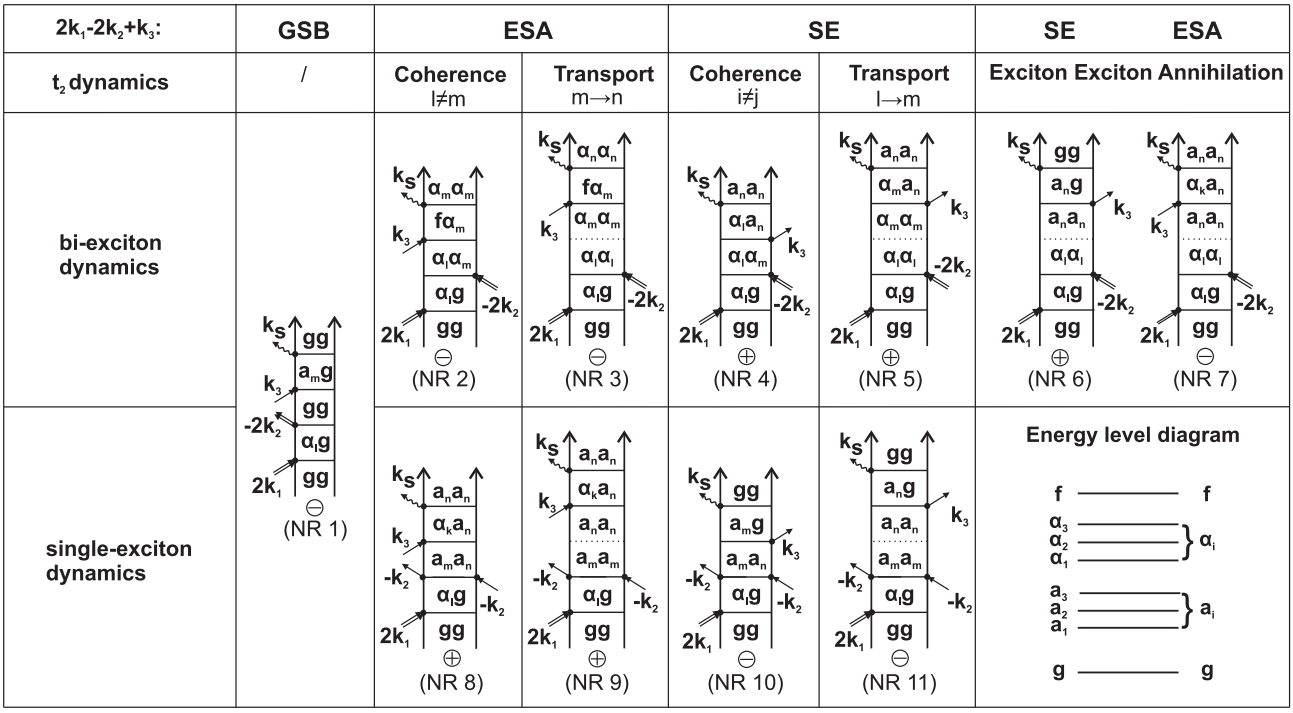

(b)

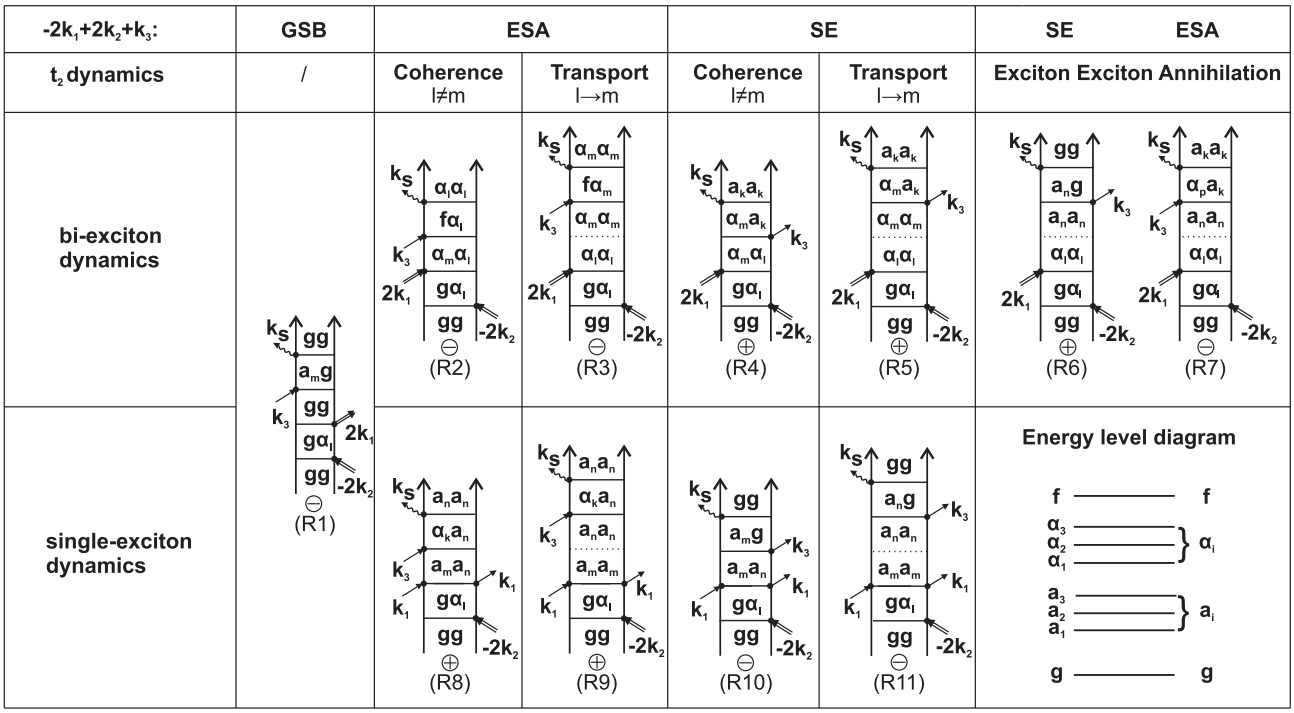

Fig. 1. Liouville space pathways (LSP) relevant for the calculation of the R^5-2D-ES signal of molecular dimers and trimers. Panel (a) and (b) depict the non-rephasing $\vec{K}_{NR} = 2\vec{K}_1 - 2\vec{K}_2 + \vec{K}_3$ and rephasing $\vec{K}_R = -2\vec{K}_1 + 2\vec{K}_2 + \vec{K}_3$ pathways, respectively. Single-, bi- and tri-exciton states are labeled by $\{|a_i\rangle\}$, $\{|\alpha_i\rangle\}$ and $\{|f_i\rangle\}$, respectively. The energy level diagram of the herein considered molecular trimer (see Section 3.2) is depicted at the bottom right of both (a) and (b). GSB: Ground state bleach, ESA: excited state absorption, SE: stimulated emission.

$$V_{P_j}(t_2) := \sum_{i \in X_j} S_i(t_1 = 0, t_2, t_3 = 0). \tag{12}$$

Eq. (12) can be understood as a new definition of the peak volume, well-suited for simulations and avoiding ambiguities when the peaks overlap. All peak volume calculations presented henceforth are thus carried out using definition (12). At many points we will integrate the volume over all peaks. This signal $V(t_2)$ can be related directly to response functions of Eqs. (2) and (3), *i. e.*

$$V(t_2) = \sum_j V_{P_j}(t_2) = \sum_j \sum_{i\in X_j} S_i(t_1=0,\, t_2,\, t_3=0)$$
$$= \sum_i S_i(t_1=0,\, t_2,\, t_3=0)$$
$$= R^{(5)}_{NR}(t_1=0,\, t_2,\, t_3=0) + R^{(5)}_{R}(t_1=0,\, t_2,\, t_3=0). \quad (13)$$

Response functions defined by Eqs. (2) and (3) are in principle rank 6 tensors. For the present work, most result are shown for aggregates with parallel orientation of dipoles where the rich tensor structure can be omitted. Certain results for aggregates with non-parallel dipoles are discussed in Section 4 and in Appendix C.

2.2. Quantum master equation for transport and annihilation

We next specify the excitonic master Eq. (5) [29] for two types of transport dynamics, Förster [26] and Redfield [27]. Transport of excitation energy, represented by superoperators $\mathscr{D}$ and $\breve{\mathscr{D}}$ in Eq. (5), is induced by electrostatic (resonance) coupling J_{mn} between transition dipoles of molecules m and n. We start with the Frenkel exciton Hamiltonian [28]

$$\widehat{H}_M = \sum_{n=1}^{N} E_n \widehat{B}_n^\dagger \widehat{B}_n + \sum_{\substack{\{n,m\}\\ n\neq m}} J_{mn} \widehat{B}_m^\dagger \widehat{B}_n, \quad (14)$$

where E_n is the energy of exciton at site n. We consider the transfer of excitation energy, induced by J_{mn}, in the framework of both Redfield and Förster theory to analyse the signal's properties in the limit of coherent and incoherent exciton dynamics, respectively. The applicability of either of these transport theories depends on the comparison between the magnitude of the resonance coupling J_{mn} and site energy fluctuations $\widehat{E}_n(t) = E_n + \widehat{Q}_n(t)$, where $\widehat{Q}_n(t)$ is a bath coordinate quantitatively characterized by the correlation function $\widetilde{C}_n(t) = \langle \widehat{Q}_n(t)\widehat{Q}_n\rangle$ [29]. Hereafter, we will employ the correlation function (in frequency domain $C_n(\omega)$: $= \int_{-\infty}^{\infty} \widetilde{C}_n(t) e^{-i\omega t} dt$

$$C_n(\omega) = \left[1 + \coth\left(\frac{\omega}{T}\right)\right] 2\lambda_n \frac{\omega\Lambda_n}{\omega^2 + \Lambda_n^2}, \quad (15)$$

describing quantum Gaussian-Markovian fluctuations. The reorganization energy λ_n measures the magnitude of fluctuations, Λ_n is the bath relaxation rate and T is the temperature. Depending on the relative magnitude between λ and J, EET is described either by Redfield or Förster theory.

For strong resonance couplings ($J \gg \lambda$) Redfield theory, a perturbative calculation in bath induced fluctuations λ, is applicable. Transport of excitation energy occurs among eigenstates $|\varepsilon_i\rangle$ of $\widehat{H}_M$ (Eq. (14)). The subsets of single-, bi- and tri-exciton states are referred to by $\{|a_i\rangle\}$, $\{|\alpha_i\rangle\}$ and $\{|f_i\rangle\}$, respectively. Dynamics in higher manifolds (involving more than three excitations) do not enter the R^5-2D-ES signal after perturbative excitation, *i. e.* Eqs. (2) and (3).

The superoperators $\breve{\mathscr{L}}_R$ for coherent evolution and $\breve{\mathscr{D}}_R$ for dissipative dynamics in both Markov [24,30] – and secular approximation [27], reads

$$\breve{\mathscr{L}}_R|\rho(t)\rangle\rangle = -i[\widehat{H}_M, \widehat{\rho}(t)] \quad (16)$$

and

$$\breve{\mathscr{D}}_R|\rho(t)\rangle\rangle = \sum_{i,j;i\neq j} [k_{\varepsilon_i\to\varepsilon_j}(|\varepsilon_j\rangle\langle\varepsilon_i|\widehat{\rho}(t)|\varepsilon_i\rangle\langle\varepsilon_j| - \tfrac{1}{2}\{|\varepsilon_i\rangle\langle\varepsilon_i|, \widehat{\rho}(t)\})$$
$$- \gamma^{pd}_{\varepsilon_i\varepsilon_j}|\varepsilon_i\rangle\langle\varepsilon_i|\widehat{\rho}(t)|\varepsilon_j\rangle\langle\varepsilon_j|], \quad (17)$$

with $\{\widehat{A}, \widehat{B}\} := \widehat{A}\widehat{B} + \widehat{B}\widehat{A}$. Transport rates $k_{\varepsilon_i\to\varepsilon_j}$ from excitonic state $|\varepsilon_i\rangle$ to $|\varepsilon_j\rangle$ are given by

$$k_{\varepsilon_i\to\varepsilon_j} = \sum_{n=1}^{N} C_n(\omega_{\varepsilon_i\varepsilon_j})|\langle\varepsilon_i|\widehat{B}_n^\dagger\widehat{B}_n|\varepsilon_j\rangle|^2, \quad (18)$$

where $\omega_{\varepsilon_i\varepsilon_j}$ is the electronic energy gap between eigenstates $|\varepsilon_i\rangle$ and $|\varepsilon_j\rangle$. The pure dephasing elements $\gamma^{pd}_{\varepsilon_i\varepsilon_j}$ are given by

$$\gamma^{pd}_{\varepsilon_i\varepsilon_j} = \frac{1}{2}\sum_{n=1}^{N} C_n(0)[\langle\varepsilon_i|\widehat{B}_n^\dagger\widehat{B}_n|\varepsilon_i\rangle - \langle\varepsilon_j|B_n^\dagger B_n|\varepsilon_j\rangle]^2. \quad (19)$$

In the case of weak coupling ($J \ll \lambda$) transport is calculated perturbatively in J. The coherent part $\breve{\mathscr{L}}_F$ of the molecule's temporal evolution

$$\breve{\mathscr{L}}_F|\rho(t)\rangle\rangle = -i[\widehat{H}_0, \widehat{\rho}(t)] \quad (20)$$

is induced by the uncoupled Hamiltonian

$$\widehat{H}_0 = \sum_{n=1}^{N} E_n \widehat{B}_n^\dagger \widehat{B}_n. \quad (21)$$

The exciton eigenbasis is local, i.e. subsets of single -, bi- and tri-exciton states of $\widehat{H}_0$ are referred to by $|n\rangle = \widehat{B}_n^\dagger|g\rangle$, $|nm\rangle = \widehat{B}_n^\dagger\widehat{B}_m^\dagger|g\rangle$ and $|nml\rangle = \widehat{B}_n^\dagger\widehat{B}_m^\dagger\widehat{B}_l^\dagger|g\rangle$ ($|g\rangle$ is the system ground state), respectively. The complete basis of local excitonic states is labeled by $\{|s_i\rangle\}$.

Förster theory for incoherent single exciton jumps [26] is embedded into the quantum master equation for transport between multi-excitonic states $|s_i\rangle$ based on a Lindblad form [31,32] of dissipative dynamics, *i. e.*

$$\breve{\mathscr{D}}_F|\rho(t)\rangle\rangle = \sum_{i,j;i\neq j} [k_{s_i\to s_j}(|s_j\rangle\langle s_i|\widehat{\rho}(t)|s_i\rangle\langle s_j| - \tfrac{1}{2}\{|s_i\rangle\langle s_i|, \widehat{\rho}(t)\})$$
$$- \gamma^{pd}_{s_i s_j}|s_i\rangle\langle s_i|\widehat{\rho}(t)|s_j\rangle\langle s_j|]. \quad (22)$$

The multi-excitonic relaxation rates $k_{s_i\to s_j}$ are calculated from the Förster rates $k_{m\to n}$, corresponding to incoherent jumps between different sites m and n, *i. e.*

$$k_{s_i\to s_j} = \sum_{m,n} k_{m\to n}|\langle s_j|B_n^\dagger B_m|s_i\rangle|^2. \quad (23)$$

Single exciton rates $k_{m\to n}$ are finally calculated from the Förster rule [26]

$$k_{m\to n} = |J_{mn}|^2 \int_0^\infty dt\; e^{-i(E_n - E_m + 2\lambda_m)t} e^{-\int_0^t dt' \int_0^{t'} dt''[C_n(t'') + C_m(t'')]}. \quad (24)$$

The pure dephasing elements $\gamma^{pd}_{s_i s_j}$ read

$$\gamma^{pd}_{s_i s_j} = \frac{1}{2}\sum_{n=1}^{N} C_n(0)[\langle s_i|B_n^\dagger B_n|s_i\rangle - \langle s_j|B_n^\dagger B_n|s_j\rangle]^2. \quad (25)$$

So far, we have discussed transport dynamics induced by the fluctuating Frenkel exciton Hamiltonian (Eq. (14)), where creation of an exciton is always connected with annihilation of another, meaning that the total number of excitons $\widehat{\mathscr{N}} = \sum_n \widehat{B}_n^\dagger\widehat{B}_n$ is conserved for both Förster and Redfield dynamics.

The process of EEA, in contrast, changes the number of excitons through a mechanism of unidirectional transport to lower excitonic manifolds, occurring when excitations are situated at adjacent sites. We employ an annihilation master equation of the following form

$$\breve{\mathscr{A}}|\rho(t)\rangle\rangle = \sum_{i=1}^{N-1}\left(k_i^{A_-}\left[\hat{L}_i^{(-)}\widehat{\rho}\,\hat{L}_i^{(-)\dagger} - \frac{1}{2}\{\hat{L}_i^{(-)\dagger}\hat{L}_i^{(-)}, \widehat{\rho}(t)\}\right] + \right.$$
$$\left. k_i^{A_+}\left[\hat{L}_i^{(+)}\widehat{\rho}\,\hat{L}_i^{(+)\dagger} - \frac{1}{2}\{\hat{L}_i^{(+)\dagger}\hat{L}_i^{(+)}, \widehat{\rho}(t)\}\right]\right), \quad (26)$$

where $k_i^{A_-}$ and $k_i^{A_+}$ are annihilation rates associated with operators

$$\hat{L}_i^{(-)} := B_{i+1}^\dagger B_{i+1} B_i$$
$$\hat{L}_i^{(+)} := B_i^\dagger B_i B_{i+1} \quad (27)$$

for annihilation of an excitation at site i ($\hat{L}_i^{(-)}$) or $i+1$ ($\hat{L}_i^{(+)}$), if two excitations are present at adjacent sites i and $i+1$. We omitted a detailed description of the annihilation process, such as the initial step of localization of excitation energy on one site with its subsequent non-radiative relaxation to the first excited state [1]. The annihilation

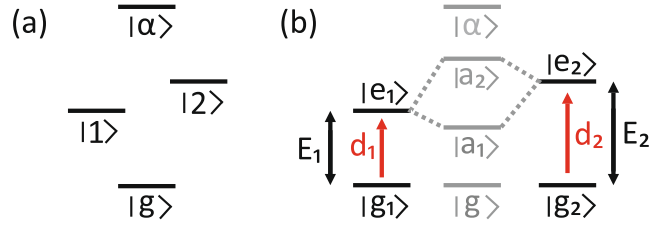

Fig. 2. (a) Energy level scheme of a weakly coupled molecular dimer with site energies E_i and transition dipoles d_i of monomer i ($i \in \{1, 2\}$). Each monomer i posses two electronic energy levels $|g_i\rangle$ and $|e_i\rangle$. (b) Strong excitonic coupling J leads to the formation of two delocalized single exciton states $|a_1\rangle$ and $|a_2\rangle$, and one bi-exciton state $|\alpha\rangle$.

dynamics of Eq. (26) defines transport between populations with different numbers of excitons in the local basis. Transformed into the delocalized basis of Redfield transport, it introduces for trimers and higher aggregates certain non-secular terms. These, however, contribute negligibly to signals [27] and will be neglected.

3. Results

3.1. Molecular dimer

We first apply the developed dynamical model to a molecular dimer. The energy level scheme is depicted in Fig. 2 for both weak ($J \ll \lambda$) and strong ($J \gg \lambda$) coupling. Assuming symmetric annihilation, i.e. $k_1^{A_+} = k_1^{A_-} = k_A$, both transport theories, i.e. Förster and Redfield, lead to a formally identical master equation for dimer populations

$$\frac{\partial}{\partial t}\begin{pmatrix}\rho_{gg}(t)\\ \rho_{x_1x_1}(t)\\ \rho_{x_2x_2}(t)\\ \rho_{\alpha\alpha}(t)\end{pmatrix} = \begin{pmatrix}0 & 0 & 0 & 0\\ 0 & -k_{x_1\to x_2} & k_{x_2\to x_1} & k_A\\ 0 & k_{x_1\to x_2} & -k_{x_2\to x_1} & k_A\\ 0 & 0 & 0 & -2k_A\end{pmatrix}\begin{pmatrix}\rho_{gg}(t)\\ \rho_{x_1x_1}(t)\\ \rho_{x_2x_2}(t)\\ \rho_{\alpha\alpha}(t)\end{pmatrix} \tag{28}$$

and coherences

$$\begin{aligned}
\tfrac{\partial}{\partial t}\rho_{x_2x_1}(t) &= -\left[i\omega_{x_2x_1} + \tfrac{1}{2}(k_{x_2\to x_1} + k_{x_1\to x_2}) + \gamma^{pd}_{x_2x_1}\right]\rho_{x_2x_1}(t)\\
\tfrac{\partial}{\partial t}\rho_{gx_2}(t) &= -\left[i\omega_{gx_2} + \tfrac{1}{2}k_{x_2\to x_1} + \gamma^{pd}_{gx_2}\right]\rho_{gx_2}(t)\\
\tfrac{\partial}{\partial t}\rho_{gx_1}(t) &= -\left[i\omega_{gx_1} + \tfrac{1}{2}k_{x_1\to x_2} + \gamma^{pd}_{gx_1}\right]\rho_{gx_1}(t)\\
\tfrac{\partial}{\partial t}\rho_{g\alpha}(t) &= -\left[i\omega_{g\alpha} + \gamma^{pd}_{g\alpha} + k_A\right]\rho_{g\alpha}(t)\\
\tfrac{\partial}{\partial t}\rho_{\alpha x_2}(t) &= -\left[i\omega_{\alpha x_2} + \tfrac{1}{2}k_{x_2\to x_1} + \gamma^{pd}_{\alpha x_2} + k_A\right]\rho_{\alpha x_2}(t)\\
\tfrac{\partial}{\partial t}\rho_{\alpha x_1}(t) &= -\left[i\omega_{\alpha x_1} + \tfrac{1}{2}k_{x_1\to x_2} + \gamma^{pd}_{\alpha x_1} + k_A\right]\rho_{\alpha x_1}(t).
\end{aligned} \tag{29}$$

States $|x_i\rangle$ and rates $k_{x_i\to x_j}$ are, however, once given by local single exciton states $|i\rangle$ and the Förster rates (24), or the delocalized single exciton states $|a_i\rangle$ and the Redfield rates (18) in the latter case. The Green's functions for Eqs. (28) and (29) are given analytically in Appendix A.

3.1.1. Homo-dimer

We first consider a parallel homo-dimer, *i. e.* $E_1 = E_2 = E$, $d_1 = d_2 = d$ and $k_{1\to 2} = k_{2\to 1} = k$. The R^5-2D-ES line shape of the weakly coupled dimer, depicted in Fig. 3(a), consists of a single negative peak positioned at $(\Omega_1, \Omega_3) = (2E, E)$, as all the single quantum coherences $|ig\rangle\rangle$, or $|\alpha i\rangle\rangle$ ($i = \{1, 2\}$) oscillate at the same frequency E during interval t_3. The peak volume of the complete signal, plotted at the bottom of Fig. 3(a), approaches its asymptotic value mono-exponentially and is independent of the single-exciton transport rate k:

$$V(t_2) = 16\mathrm{d}^6[G_{\alpha\alpha,\alpha\alpha}(t_2) - G_{\mathrm{gg,gg}}(t_2)] = 16\mathrm{d}^6[e^{-2k_At_2} - 1]. \tag{30}$$

Even though the spectrally integrated signal vanishes at short delays ($t_2 = 0$), the signal's peak intensity is relatively strong as shown in the top left panel of Fig. 3(a). Therefore, the central negative feature is perfectly compensated by the surrounding positive signal. To understand the nature of this compensation in more detail we analyze the temporal evolution of the response $\overline{R}(\Omega_1, t_2, t_3)$ in t_3 and take a cut at the bi-exciton energy $\Omega_1 = 2E$, before any relaxation or annihilation dynamics appear ($t_2 = 0$). The response function is given by the difference between contributions which evolve in $|\alpha a_i\rangle\rangle$ coherences during t_3 (pathways: 5, 8, and 9 in Fig. 1(a) and (b)) and in $|a_ig\rangle\rangle$ coherence (pathways: 1, 10, 11 in Fig. 1(a) and (b)) during t_3

$$\overline{R}(2E_1, 0, t_3) = 48d^6\frac{\mathrm{e}^{-(iE+\Gamma_A)t_3} - \mathrm{e}^{-(iE+\Gamma_R)t_3}}{k_A + \gamma^{pd}_{g\alpha}}. \tag{31}$$

The two terms oscillate with the same (average) frequency E, but their damping rates $\Gamma_A = \frac{1}{2}k + k_A + \gamma^{pd}$ and $\Gamma_R = \frac{1}{2}k + \gamma^{pd}$ are different as the annihilation selectively broadens $|\alpha a_i\rangle\rangle$coherence. A half sided Fourier transformation of Eq. (31) over t_3 thus results in complex line shapes, given by the subtraction of two Lorentzians with different widths

$$\overline{R}(2E, t_2 = 0, \Omega_3) = \frac{48d^6}{k_A + \gamma^{pd}_{g\alpha}}\frac{[(\Omega_3 - E)^2 - \Gamma_A\Gamma_R](\Gamma_A - \Gamma_R)}{[(\Omega_3 - E)^2 + \Gamma_A^2][(\Omega_3 - E)^2 + \Gamma_R^2]}, \tag{32}$$

seen in Fig. 3(a) at $t_2 = 0$. At later delay times $k_At_2 \gg 1$ annihilation erases bi-exciton population and the negative contributions (pathways: 1, 10, 11 in Fig. 1(a) and (b)) dominate the line shape of the signal.

By increasing the excitonic coupling J the eigenstates lose local character and become delocalized. The state $|a_2\rangle = \frac{1}{\sqrt{2}}(|1\rangle + |2\rangle)$ carries all dipole moment $\mu_{a_2g} = \mu_{\alpha a_2} = \sqrt{2}\,d$, while $|a_1\rangle = \frac{1}{\sqrt{2}}(|1\rangle - |2\rangle)$ is dark and cannot be directly probed as $\mu_{a_2g} = \mu_{\alpha a_2} = 0$, for the assumed parallel configuration. The strong excitonic coupling also separates frequencies of coherence $|a_2g\rangle\rangle$ from coherence $|\alpha a_2\rangle\rangle$ and shifts them to $E + J$ and , respectively. This splits the single peak observed in the weakly coupled case into a positive and a negative peak, positioned at $(2E, E + J)$ and $(2E, E - J)$. Peak P_1 (P_2) is only contributed by pathways oscillating during t_3 with frequency of coherence $|\alpha a_2\rangle\rangle$ ($|a_2g\rangle\rangle$), the line shape of both peaks is thus simple Lorentzian at all t_2 delays. The peak volumes of P_1

$$V_{P_1}(t_2) = 16d^6[2G_{a_2a_2,a_2a_2}(t_2) - G_{a_2a_2,\alpha\alpha}(t_2) + G_{\alpha\alpha,\alpha\alpha}(t_2)] \tag{33}$$

and P_2

$$V_{P_2}(t_2) = 16\mathrm{d}^6[G_{a_2a_2,\alpha\alpha}(t_2) - 2G_{a_2a_2,a_2a_2}(t_2) - G_{\mathrm{gg,gg}}(t_2)] \tag{34}$$

thus depend on both transport and annihilation dynamics. However, the sum of both signals, i.e. the total signal, given by

$$V(t_2) = V_{P_1}(t_2) + V_{P_2}(t_2) = 16\mathrm{d}^6[G_{\alpha\alpha,\alpha\alpha}(t_2) - G_{\mathrm{gg,gg}}(t_2)], \tag{35}$$

is identical to the weakly coupled case (see Eq. (30)), and solely controlled by the annihilation rate.

The annihilation rate of a parallel homo-dimer is therefore directly accessible in a fifth order experiment through a measurement of the spectrally integrated peak volume. This observation is true independently of the coupling regime and timescale of the single exciton transport in agreement with and in extension of reference [16]. Below we explore the applicability of similar statements beyond the symmetric case.

3.1.2. Hetero-dimer

We consider the R^5-2D-ES signal of a hetero-dimer, i.e. $E_1 < E_2$, $d_1 \neq d_2$. The line shapes for the weak coupling case are depicted in Fig. 4(a). They consist of two peaks, P_1 and P_2, positioned at the site energies $\Omega_3 = \{E_1, E_2\}$ and at the double excitation energy at $\Omega_1 = E_1 + E_2$.

The peak volume of P_1

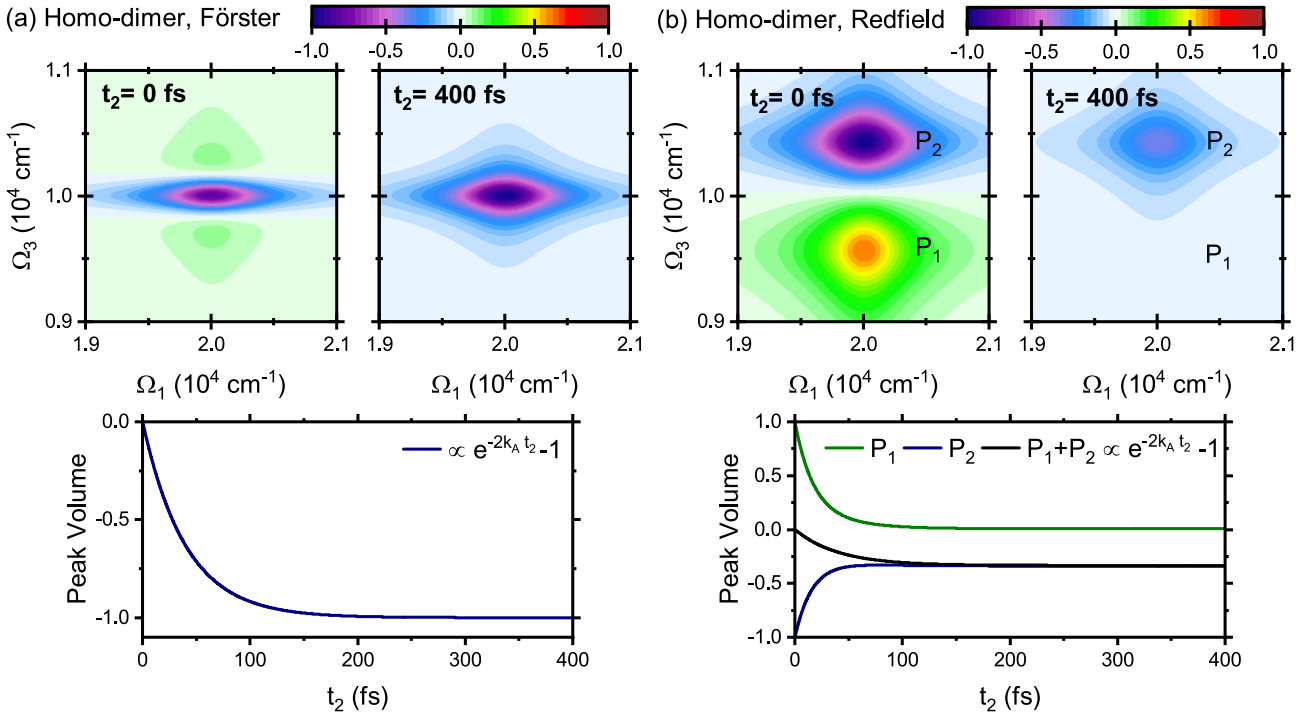

Fig. 3. R^5-2D-ES signal (top panels) of a weakly (a) and strongly (b) coupled homo-dimer for two different waiting times. Parameters: $E = 10^4\,\mathrm{cm}^{-1}$, $k_A^{-1} = 80$ fs, and (Förster transport Eq. (22) at left panel): $k_{2\to1}^{-1} = k_{1\to2}^{-1} = 400$ fs, (Redfield transport Eq. (17) at right panel): $k_{a_2\to a_1}^{-1} = 17$ fs, $k_{a_1\to a_2}^{-1} = 980$ fs, $J = 420\,\mathrm{cm}^{-1}$. The presented 2D maps are normalized to the maximum of all calculated 2D maps. The bottom panel in both (a) and (b) shows the evolution of the peak volume, normalized to the asymptotic (a) or to the starting value (b) of the signal, versus the waiting time t_2.

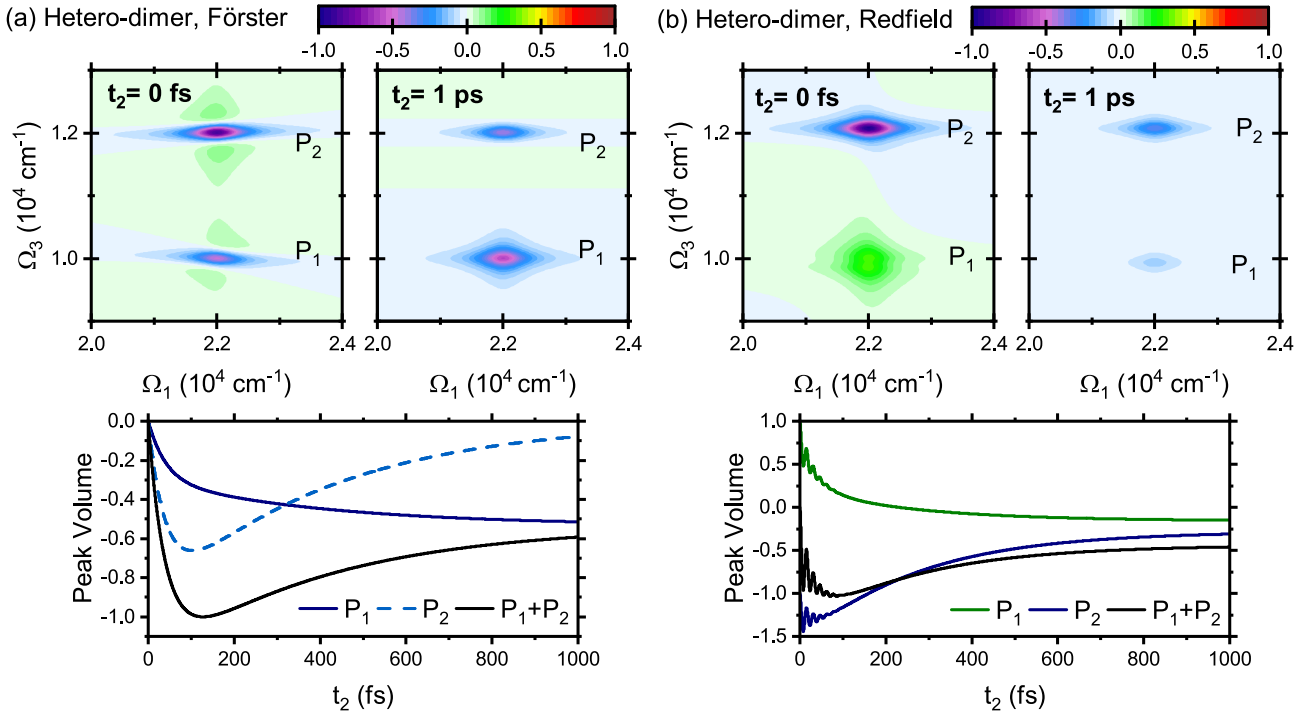

Fig. 4. R^5-2D-ES signal (top panels) of a weakly (a) and strongly (b) coupled hetero-dimer for two different waiting times. Parameters: $E_1 = 10^4\,\mathrm{cm}^{-1}$, $E_2 = 1.2{\cdot}10^4\,\mathrm{cm}^{-1}$, $d_2 = 2d_1$, $k_A^{-1} = 80$ fs, specific for Förster Eq. (22): $k_{2\to1}^{-1} = 400$ fs, $k_{1\to2}^{-1} \approx 0$ fs, specific for Redfield Eq. (17): $k_{a_2\to a_1}^{-1} = 265$ fs, $k_{a_1\to a_2}^{-1} \approx 0$ fs, $J = 374\,\mathrm{cm}^{-1}$. The presented 2D maps are normalized to the maximum of all calculated 2D maps. The bottom panel in both (a) and (b) shows the evolution of the peak volume, normalized to the minimum (a) or to the starting value (b) of the signal, versus the waiting time t_2.

$$V_{P_1}(t_2) = 8d_1^4 d_2^2 [G_{\alpha\alpha,\alpha\alpha}(t_2) - G_{gg,gg}(t_2) + G_{22,11}(t_2) + G_{22,22}(t_2) - G_{11,11}(t_2) - G_{11,22}(t_2) - G_{22,\alpha\alpha}(t_2) + G_{11,\alpha\alpha}(t_2)] \quad (36)$$

again vanishes at $t_2 = 0$, and the line shape shows similar compensating features, as we have seen for the homo-dimer. In the case of peak P_1, it originates from interference of $|\alpha 2\rangle\rangle$ and $|1g\rangle\rangle$ coherences which oscillate with the same frequency $\omega_{\alpha 2} = \omega_{g1}$. Similarly to Eq. (31), transport

and annihilation broadens the two coherences differently as $\Gamma_A = \frac{1}{2}k_{2\to1} + k_A + \gamma_{\alpha 2}^{pd}$ and $\Gamma_R = \frac{1}{2}k_{1\to2} + \gamma_{g1}^{pd}$.

At longer t_2 delays, annihilation deactivates bi-exciton populations $|\alpha\alpha\rangle\rangle$ while the populations of lower lying single exciton $|1\alpha\rangle\rangle$ retain (as $k_{2\to1} > k_{1\to2}$). The line shape of P_1 in Fig. 4(a) is thus asymptotically dominated by the first term of Eq. (31) and becomes single-Lorentzian.

The volume of peak P_2

$$\begin{aligned} V_{P_2}(t_2) = 8d_1^2 d_2^4 [&G_{\alpha\alpha,\alpha\alpha}(t_2) - G_{gg,gg}(t_2) \\ &- G_{22,11}(t_2) - G_{22,22}(t_2) + G_{11,11}(t_2) + G_{11,22}(t_2) \\ &+ G_{22,\alpha\alpha}(t_2) - G_{11,\alpha\alpha}(t_2)] \end{aligned} \tag{37}$$

is again vanishing at short delays and shows compensating features caused by differences between widths of $|\alpha 1\rangle\rangle$ coherence ($\Gamma_A = \frac{1}{2}k_{2\to1} + k_A + \gamma_{\alpha 2}^{pd}$) and $|2g\rangle\rangle$ coherence ($\Gamma_R = \frac{1}{2}k_{1\to2} + \gamma_{g1}^{pd}$). The evolution is different from P_1, as at later t_2 times the population $|22\rangle\rangle$ tends to be small as $k_{2\to1} > k_{1\to2}$. The peak volume of P_2 thus remains small for long waiting times. From the above Eqs. (36) and (37) it is evident that the dynamics of peaks P_1 and P_2 are always influenced by both transport and annihilation processes, as is the total peak volume (see bottom panel of Fig. 4(a))

$$\begin{aligned} V(t_2) &= V_{P_1}(t_2) + V_{P_2}(t_2) \\ &= 8d_1^2 d_2^2 [(d_1^2 + d_2^2)(G_{\alpha\alpha,\alpha\alpha}(t_2) - G_{gg,gg}(t_2)) \\ &\quad + (d_1^2 - d_2^2)(G_{22,22}(t_2) - G_{11,11}(t_2) \\ &\quad - G_{11,22}(t_2) + G_{22,11}(t_2) - G_{22,\alpha\alpha}(t_2) + G_{11,\alpha\alpha}(t_2))]. \end{aligned} \tag{38}$$

The second term $\propto (d_1^2 - d_2^2)$, however, may vanish if the two dipole moments are the same, *i.e.* $d_1 = d_2$. In this limit Eq. (30) is recovered, regardless the difference in transition energies E_1 and E_2.

For a strongly coupled hetero-dimer, a similar line shape analysis as for the above discussed weak coupling case can be performed. Details of the calculation are discussed in Appendix B. The calculated R^5-2D-ES spectra depicted in Fig. 4(b) show two peaks at $(2E,\ E_{a_1})$, and $(2E,\ E_{a_2})$, respectively. The distinguishing feature of the strong coupling case are oscillatory beatings at early times, resulting from evolution of $|a_1 a_2\rangle\rangle$ and $|a_2 a_1\rangle\rangle$ coherence within the waiting time t_2. Traces of the individual peaks P_1 and P_2 as well as the total peak volume (bottom of Fig. 4(b)) depend on both relaxation and annihilation processes. The analytical expression for the integrated signal reads

$$\begin{aligned} V(t_2) = 2D^2 [&(\mu_{\alpha a_2}^2 + \mu_{\alpha a_1}^2) G_{\alpha\alpha,\alpha\alpha}(t_2) - (\mu_{a_1 g}^2 + \mu_{a_2 g}^2) G_{gg,gg}(t_2) \\ &+ (\mu_{a_2 g}^2 - \mu_{\alpha a_2}^2) G_{a_2 a_2,\alpha\alpha}(t_2) + (\mu_{a_1 g}^2 - \mu_{\alpha a_1}^2) G_{a_1 a_1,\alpha\alpha}(t_2)] \\ &+ 4D [\mu_{a_1 g}\mu_{\alpha a_1}(\mu_{\alpha a_2}^2 - \mu_{a_2 g}^2) G_{a_2 a_2, a_1 a_1}(t_2) \\ &+ \mu_{a_2 g}\mu_{\alpha a_2}(\mu_{\alpha a_2}^2 - \mu_{a_2 g}^2) G_{a_2 a_2, a_2 a_2}(t_2) \\ &+ \mu_{a_1 g}\mu_{\alpha a_1}(\mu_{\alpha a_1}^2 - \mu_{a_1 g}^2) G_{a_1 a_1, a_1 a_1}(t_2) \\ &+ \mu_{a_2 g}\mu_{\alpha a_2}(\mu_{\alpha a_1}^2 - \mu_{a_1 g}^2) G_{a_1 a_1, a_2 a_2}(t_2) \\ &+ (\mu_{a_1 g}\mu_{\alpha a_1}(\mu_{\alpha a_2}^2 - \mu_{a_2 g}^2) + \mu_{a_2 g}\mu_{\alpha a_2}(\mu_{\alpha a_1}^2 - \mu_{a_1 g}^2)) \mathrm{Re}\{G_{a_1 a_2, a_1 a_2}(t_2)\}], \end{aligned} \tag{39}$$

where $D := \mu_{a_1 g}\mu_{\alpha a_1} + \mu_{a_2 g}\mu_{\alpha a_2}$. Expressions for the peak volume evolution of the individual peaks is given in Appendix B.

As the eigenstates $|a_1\rangle$ and $|a_2\rangle$ are orthonormal, condition for identical dipoles $d_1 = d_2$ translates into the following relation of oscillatory strengths between the delocalized states, $\mu_{\alpha a_1} = \mu_{a_1 g}$ and $\mu_{a_2 \alpha} = \mu_{a_2 g}$. In that case Eq. (39) simplifies significantly, as all transport and coherence components identically vanish and Eq. (30) is restored.

The above calculations for homo-dimers do not show any dependence of the integrated signal on exciton transport, despite the fact that annihilation is known to be diffusion limited [33]. Dynamics of the molecular dimer, however, inherently lacks migration through the bi-exciton manifold (pathways: 2–5 in Fig. 1(a) and (b)), where the diffusion of two excitons properly limits the annihilation. We thus investigate the signal of molecular trimers in the next subsection, as the simplest aggregate allowing to address the question of migration through the bi-exciton manifold, while maintaining a tractable master equation model.

3.2. Molecular trimer

In this section we focus on simulations of R^5-2D-ES signals from homo-trimers. We have shown in Section 3.1 that the spectrally integrated peak volume is a well-suited measure of annihilation dynamics for a homo-dimer. Before applying the same method to the homo-trimer, we present a general proof for the applicability of integrated R^5-2D-ES signals as a reporter on EEA in molecular aggregates. In other words, we show that total peak volume vanishes for exciton conserving dynamics ($k_A = 0$), see Eqs. (30) and (35), for larger aggregates with identical and parallel dipole moments. We formally extend the proof to a chain of arbitrary length and identical dipoles, *i.e.* $\vec{d}_i = \vec{d}$ (i=1, ... ,N).

Due to the Pauli commutation rule Eq. (1), any Liouville space element $|W\rangle\rangle$ obeys the following relation:

$$\langle\langle\mu|\breve{\mu}^{(+)}|W\rangle\rangle = \sum_n d_n^2 \mathrm{Tr}\{(1 - 2\hat{B}_n^\dagger \hat{B}_n)\widehat{W}\}.$$

Assuming identical dipoles $d_n = d$, the right hand side can be factorized to the exciton number operator $\hat{\mathcal{N}} \equiv \sum_n \hat{B}_n^\dagger \hat{B}_n$, as

$$\langle\langle\mu|\breve{\mu}^{(+)}|W\rangle\rangle = d^2 \mathrm{Tr}\{(1 - 2\hat{\mathcal{N}})\widehat{W}\}. \tag{40}$$

For exciton (and total density) conserving evolution $\widehat{W}(t_2) = \breve{G}(t_2)\widehat{W}(0)$, the expectations of Eq. (40) shall not change

$$\mathrm{Tr}\{(1 - 2\hat{\mathcal{N}})\widehat{W}(t_2)\} = \mathrm{Tr}\{(1 - 2\hat{\mathcal{N}})\widehat{W}(0)\}.$$

Setting $\widehat{W}(t_2) = \breve{\mathscr{G}}(t_2)\breve{\mu}^{(-)}\breve{\mu}^{(-)}\breve{\mu}^{(+)}\breve{\mu}^{(+)}|gg\rangle\rangle$ (note, that $\mathrm{Tr}\{\widehat{W}\} = 0$) we reconstruct the integrated peak volume of the non-rephasing signal

$$R_{NR}^{(5)}(t_1 = 0,\ t_2,\ t_3 = 0) = \langle\langle\mu|\breve{\mu}^{(+)}|\widehat{W}(t_2)\rangle\rangle \tag{41}$$

and conclude that is not changed during t_2, for annihilation free dynamics of homo-aggregates

$$R_{NR}^{(5)}(0,\ t_2,\ 0) = R_{NR}^{(5)}(0,\ 0,\ 0) = d^2 \mathrm{Tr}\{(1 - 2\hat{\mathcal{N}})\widehat{W}\}$$

and, in fact, vanishes $R_{NR}^{(5)}(0,\ t_2,\ 0) = 0$, as can be proved by straightforward evaluation of $R_{NR}^{(5)}(0,\ 0,\ 0)$ with the use of commutation relation (1).

The proof of $R_R^{(5)}(0,\ t_2,\ 0) = 0$ is completely analogous with setting $\widehat{W}(t_2) = \breve{\mathscr{G}}(t_2)\breve{\mu}^{(+)}\breve{\mu}^{(+)}\breve{\mu}^{(-)}\breve{\mu}^{(-)}|gg\rangle\rangle$. With Eq. (12) we get $V(t_2) = R_R^{(5)}(0,\ t_2,\ 0) + R_{NR}^{(5)}(0,\ t_2,\ 0) = 0$. Quod erat demonstrandum.

We thus focus on simulations of homo-trimers ($d_1 = d_2 = d_3 = d$, $E_1 = E_2 = E_3 = E$, $J_{12} = J_{23} \gg J_{13}$), which excitonic level scheme (ground state, three single/bi-exciton states and one tri-exciton state) is depicted in Fig. 5. Assuming weak coupling between the monomeric units, the excitonic eigenstates (Fig. 5(a)) are degenerate and have local character. The R^5-2D-ES signal of a weakly coupled homo-trimer depicted in Fig. 6(a) thus consists of a single peak centered at the site energy $\Omega_3 = E$ and at the bi-exciton eigenenergy at $\Omega_1 = 2E$ with a line shape roughly similar to the weakly coupled homo-dimer depicted in Fig. 3(a).

The temporal evolution of the peak volume, plotted at the bottom of Fig. 6(a) for various relaxation rates k_R but fixed annihilation rate, is decidedly different to the homo-dimer case. It shows a clear bi-exponential behavior, combining timescales of annihilation and transport. In detail, early times reveal fast annihilation of neighboring excitations. Subsequently, annihilation of excitons placed on the first and third molecule must be preceded by exciton transport to adjacent sites. The slower component of exponential decay is thus controlled by the transport (exciton diffusion) rate as shown in the bottom panel of Fig. 6(a).

The top panels of Fig. 6(b) depict the R^5-2D-ES signal of a strongly

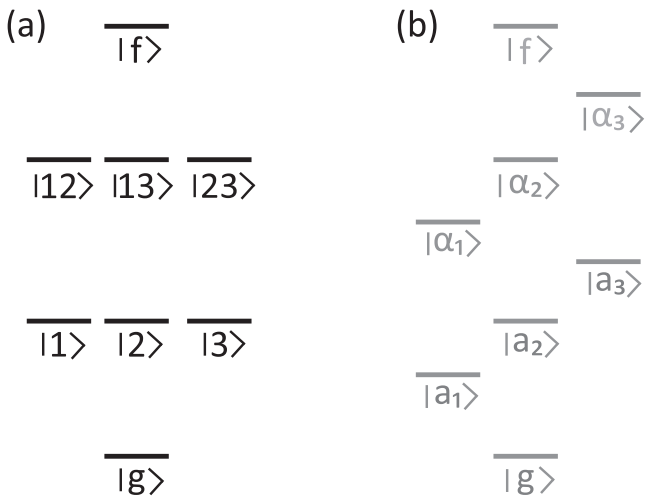

Fig. 5. (a) Energy level scheme of a weakly coupled homo-trimer, where each unit posses two electronic levels (b) Strong excitonic coupling lifts the degeneracy between the excitonic states and leads to the formation of highly delocalized single –, bi, and tri-exciton states, $|a_i\rangle$, $|\alpha_i\rangle$ and $|f\rangle$, respectively. ($i \in \{1, 2, 3\}$).

coupled homo-trimer for two different waiting times. The strong excitonic coupling lifts the degeneracy between the excitonic states and leads to the formation of highly delocalized excitonic eigenstates (5). Only a few transitions between these states carries significant dipole: from ground to the single exciton manifold eigenstate $|a_3\rangle \approx |1\rangle + \sqrt{2}|2\rangle + |3\rangle$, from $|a_3\rangle$ to the bi-exciton state $|\alpha_3\rangle \approx |12\rangle + \sqrt{2}|13\rangle + |23\rangle$ and from $|\alpha_3\rangle$ to $|f\rangle$. The transition dipoles are given by $\mu_{\alpha_3 g} = \mu_{\alpha_3 a_3} \approx \frac{2-\sqrt{2}}{2} d$ and $\mu_{f\alpha_3} \approx \frac{3}{2} d$ (symbol $\approx$ refers to limit $J_{13} \ll J_{12}$).

The R^5-2D-ES maps thus show features at the bi-exciton energy $\Omega_1 \approx 2E + \sqrt{2}\, J_{12}$ (marked by a solid line in Fig. 6(b)) linked to bi-exciton $|\alpha_3\rangle$. Peaks along Ω_3 appear at the energies of coherence $|a_3 g\rangle\rangle$ ($\Omega_3 \approx E + \sqrt{2}\, J_{12}$), $|\alpha_3 a_3\rangle\rangle$ ($\Omega_3 \approx E$) and $|f\alpha_3\rangle\rangle$ ($\Omega_3 \approx E - \sqrt{2}\, J_{12}$) marked by dashed lines in Fig. 6(b). The peak intensities along Ω_3 varies with t_2 delay times. At short times we see significant SE (pathways NR4 and NR5 in Fig. 1(a) and R4 and R5 in Fig. 1(b); below referred in short as pathways 4 and 5) and ESA (pathways 8 and 9) contributions at frequency of coherence $|\alpha_3 a_3\rangle\rangle$. At frequency $|a_3 g\rangle\rangle$ we still notice strong GSB (pathway 1) and SE (pathways 10 and 11) contributions at early times. The peak related to coherence $|f\alpha_3\rangle\rangle$ is weaker, as $\mu_{f\alpha_3} \ll \mu_{g a_3} = \mu_{\alpha_3 a_3}$. At long delays ($t_2 = 400$ fs, right panel) all transport and annihilation dynamics are finished. The signal is then dominated by the GSB (pathway 1) contribution at $|a_3 g\rangle\rangle$ resonance and the asymptotic values of SE (pathways 4 and 5) contributions at resonance $|\alpha_3 a_3\rangle\rangle$. The peak at resonance $|f\alpha_3\rangle\rangle$ vanishes completely with bi-exciton manifold depopulation.

The bottom panel of Fig. 6(b) shows the evolution of the peak volume with the waiting time t_2, plotted for various relaxation rates k_R. It behaves significantly different to the weak coupling case. The high delocalization of the excitonic states leads to annihilation of excitation energy on very short timescale and thus, for the small trimeric aggregate, no time-scale separation between transport and annihilation dynamics is predicted. The signal thus decays mono-exponentially and independent from the relaxation rate k_R, but dominated by the annihilation rate, to its asymptotic value. The peak volume of the R^5-2D-ES signal of a homo-trimer with parallel dipoles, independent of the coupling regime, thus allows a direct investigation of bi-exciton relaxation channels.

4. Discussion and conclusion

In this study, we investigated the effects of transport and annihilation of excitons on fifth order spectra emitted into $\vec{K}_R = 2\vec{K}_1 - 2\vec{K}_2 + \vec{K}_3$

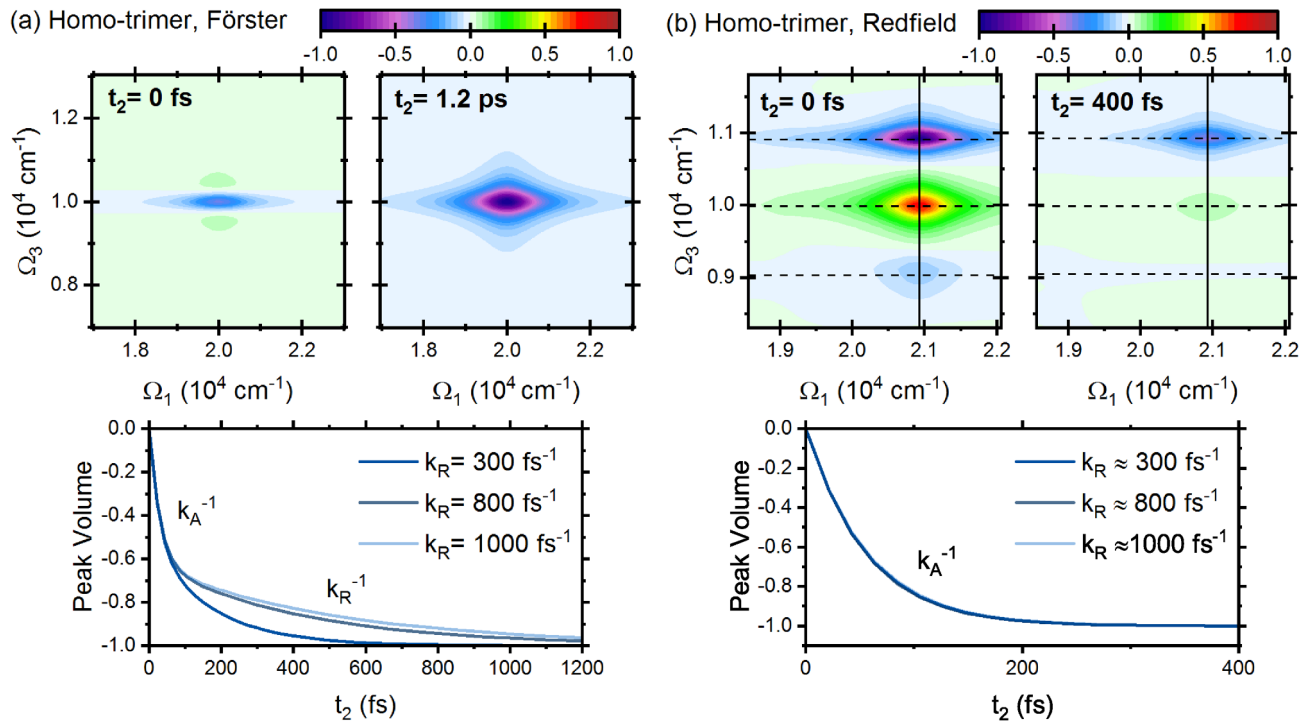

Fig. 6. R^5-2D-ES signal of a weakly (top panels of a) and strongly (top panels of b) coupled homo-trimer for two different waiting times, as indicated in the respective figure. General parameter for the presented R^5-2D-maps: $E = 10^4\ \mathrm{cm}^{-1}$, $k_A^{-1} = 60$ fs, specific for Förster: $k_{1\to2}^{-1} = k_{2\to1}^{-1} = k_{3\to2}^{-1} = k_{2\to3}^{-1} = 300$ fs, $k_{3\to1}^{-1} = k_{1\to3}^{-1} = 0$, specific for Redfield: $k_{a_2\to a_1}^{-1} = k_{a_3\to a_2}^{-1} \approx 300$ fs, $k_{a_1\to a_2}^{-1} = k_{a_2\to a_3}^{-1} = k_{a_1\to a_3}^{-1} \approx 0$ fs, $J_{12} = J_{23} = 630\ \mathrm{cm}^{-1}$, $J_{13} = 80\ \mathrm{cm}^{-1}$. The presented 2D maps are normalized to the maximum of all calculated 2D maps. The bottom panel in both (a) and (b) shows the evolution of the peak volume for different relaxation rates, normalized to its asymptotic value, versus the waiting time t_2.

and $\vec{K}_{NR} = -2\vec{K}_1 + 2\vec{K}_2 + \vec{K}_3$ phase matching directions. We presented a master equation approach to simulate these signals in the limit of Redfield and Förster type exciton transport dynamics for dimers and trimers.

We chose the electronic two level dimer as a starting point to analyze the properties of the R^5-2D-ES signal in an analytically solvable model. The model confirms that the signal from a homo-dimer is directly related to the annihilation rate. The vanishing peak volumes, still does not always imply a vanishing line shape. We argue that significant annihilation rates imply $|\alpha a\rangle\rangle$ coherences to be wider than $|ag\rangle\rangle$ coherence and despite their negative interference the signal does not vanish identically, but result into fairly complex line shapes. In case of the hetero-dimer, the peak volume evolution shows a more involved dependency on both annihilation and transport rates. The proper effects of transport are inside the second exciton manifold as we demonstrated in simulations of molecular trimers. The timescale of exciton diffusion affects the peak volume decay of a weakly coupled trimer, as excitons must migrate to adjacent sites to annihilate. The highly delocalized excitons of a strongly coupled trimer, however, do not allow for more than one stable exciton within the delocalization length and thus no exciton diffusion timescale is visible in the peak volume decay.

We further show that the annihilation dynamics is essential for the appearance of an integrated signal of homo-aggregates of arbitrary length. This finding is of considerable interest for measurements of the R^5-2D-ES signal, as the total peak volume is easily accessible, whereas the comparison of individual peaks is far more challenging.

For the above conclusions on homo-aggregates, only the equality of dipoles seems technically important, site energies may be allowed to vary. This view is, however, closely tied to the impulsive limit used in the present study. For experiments performed with finite pulses, the transition frequencies of the chromophores should also be similar, as finite pulses effectively rescale dipole magnitudes. As a simple example, a transition μ_{a_1g} has to be replaced by $\mu_{a_1g} \times E(\omega_{a_1g})$ [34,35], where $E(\omega_{a_1g})$ is the electric field evaluated at transition frequency ω_{a_1g}. Thus also transition frequencies of the chromophores should be identical, as they are for true homo-aggregates.

The core assumption of our entire analysis is a parallel configuration of dipoles. An interesting question is whether our conclusions can be extended towards more general spatial arrangements. In particular, will the integrated signal disappear for annihilation-free dynamics in aggregates consisting of identical ($|d_n| = d$) but non-parallel molecules ($\vec{d}_i \neq \vec{d}_j$). To this end the so far omitted tensor structure of the response functions (Eqs. (2) and (3)) should be considered. Assuming a periodic structure, such as a crystal, where the dipoles orientation is fixed in space, solely a specific tensor element of the non-linear response has to be calculated according to the polarization of the electric field. The obtained signals are thus similar to the hetero-dimer signals given by Eqs. (38) and (39). In liquids samples, however, the orientation differs from one individual aggregate to another and one usually considers them to be uniformly distributed along the entire spatial angle. We thus implemented a procedure to rotationally average tensors of rank six along reference [36] on the top of our dimer and trimer simulations.

Our simulations found that the integrated isotropic signal $V(t_2)$ of a dimer seems to vanish for annihilation-free dynamics ($k_A = 0\,\mathrm{fs}^{-1}$) whenever the dipoles have the same magnitude $|d_1| = |d_2|$, regardless of their relative orientation, Redfield/Förster transport or laser pulse polarization. In Appendix C we outline a formal proof for Förster dynamics in the dimer-case. Simulations on trimers (with bent structures), suggest that an extension to larger aggregates is not possible. We obtain non-zero signals for such structures in both weak and strong coupling regime of annihilation-free dynamics. However, this means that the peak volume of the R^5-2D-ES signal, beyond its capability of directly monitoring bi-exciton relaxation channels, contains information on the molecule's conformation.

Acknowledgment

J. H and C. H. acknowledge support by Deutsche Forschungsgemeinschaft (DFG, German Research Foundation) through TUM International Graduate School of Science and Engineering (IGSSE), GSC 81 and funding by DFG under Germany's Excellence Strategy – EXC 2089/1–390776260. F.Š and C.H. acknowledge support by Czech Science Foundation (Grant No. 17-22160S). Mobility is supported by project "*Exciton-exciton annihilation probed by non-linear spectroscopy* " (MSMT Grant No. 8J19DE009, DAAD-Projekt 57444962).

Appendix A. Green's functions for dynamics of dimer

The Green's function solution to master Eqs. (28) and (29):

$$G_{gg,gg}(t) = 1 \tag{A.1}$$

$$G_{x_2x_2,x_2x_2}(t) = \frac{k_{x_1\to x_2} + k_{x_2\to x_1} e^{-(k_{x_2\to x_1}+k_{x_1\to x_2})t}}{k_{x_2\to x_1} + k_{x_1\to x_2}} \tag{A.2}$$

$$G_{x_2x_2,x_1x_1}(t) = \frac{k_{x_1\to x_2}}{k_{x_2\to x_1} + k_{x_1\to x_2}}(1 - e^{-(k_{x_2\to x_1}+k_{x_1\to x_2})t}) \tag{A.3}$$

$$G_{x_2x_2,\alpha\alpha}(t) = \frac{k_{x_1\to x_2}}{k_{x_2\to x_1} + k_{x_1\to x_2}} + \frac{k_A(k_{x_1\to x_2} - k_{x_2\to x_1})e^{-(k_{x_2\to x_1}+k_{x_1\to x_2})t}}{(k_{x_2\to x_1} + k_{x_1\to x_2})(k_{x_2\to x_1} + k_{x_1\to x_2} - 2k_A)} + \frac{(k_{x_1\to x_2} - k_A)e^{-2k_At}}{2k_A - k_{x_2\to x_1} - k_{x_1\to x_2}} \tag{A.4}$$

$$G_{x_1x_1,x_2x_2}(t) = \frac{k_{x_2\to x_1}}{k_{x_2\to x_1} + k_{x_1\to x_2}}(1 + e^{-(k_{x_2\to x_1}+k_{x_1\to x_2})t}) \tag{A.5}$$

$$G_{x_1x_1,x_1x_1}(t) = \frac{k_{x_2\to x_1} + k_{x_1\to x_2} e^{-(k_{x_2\to x_1}+k_{x_1\to x_2})t}}{k_{x_2\to x_1} + k_{x_1\to x_2}} \tag{A.6}$$

$$G_{x_1x_1,\alpha\alpha}(t) = \frac{k_{x_2\to x_1}}{k_{x_2\to x_1} + k_{x_1\to x_2}} + \frac{k_A(k_{x_2\to x_1} - k_{x_1\to x_2})e^{-(k_{x_2\to x_1}+k_{x_1\to x_2})t}}{(k_{x_2\to x_1} + k_{x_1\to x_2})(k_{x_2\to x_1} + k_{x_1\to x_2} - 2k_A)} + \frac{(k_{x_2\to x_1} - k_A)e^{-2k_At}}{2k_A - k_{x_2\to x_1} - k_{x_1\to x_2}} \tag{A.7}$$

$$G_{\alpha\alpha,\alpha\alpha}(t) = e^{-2k_At} \tag{A.8}$$

are ready to be substituted into Eqs. (30)–(39). Other elements of Green's function than these of Eqs. (A.1)–(A.8) are zero.

Appendix B. Peak volumes and lineshapes of hetero dimers with Redfield dynamics

The analytical expressions for the peak volume of peak P_1 and P_2 in Fig. 4(b) are given by

$$V_{P_1}(t_2) = 2D^2[\mu_{\alpha a_2}^2 (G_{\alpha\alpha,\alpha\alpha}(t_2) - G_{a_2a_2,\alpha\alpha}(t_2)) + \mu_{a_1g}^2 (G_{a_1a_1,\alpha\alpha}(t_2) - G_{gg,gg}(t_2))]$$
$$+ 4D[\mu_{a_1g}\mu_{\alpha a_1}\mu_{\alpha a_2}^2 G_{a_2a_2,a_1a_1}(t_2) + \mu_{a_2g}\mu_{\alpha a_2}^3 G_{a_2a_2,a_2a_2}(t_2) - \mu_{a_1g}^3\mu_{\alpha a_1} G_{a_1a_1,a_1a_1}(t_2) - \mu_{a_2g}\mu_{\alpha a_2}\mu_{a_1g}^2 G_{a_1a_1,a_2a_2}(t_2)]$$
$$+ 2D[\mu_{a_1g}(\mu_{\alpha a_1}\mu_{\alpha a_2}^2 - \mu_{a_2g}^2\mu_{\alpha a_1}) + \mu_{a_2g}(\mu_{\alpha a_1}^2\mu_{\alpha a_2} - \mu_{a_1g}^2\mu_{\alpha a_2})] G_{a_1a_2,a_1a_2}(t_2) \tag{B.1}$$

and

$$V_{P_2}(t_2) = 2D^2[\mu_{\alpha a_1}^2 (G_{\alpha\alpha,\alpha\alpha}(t_2) - G_{a_1a_1,\alpha\alpha}(t_2)) + \mu_{a_2g}^2 (G_{a_2a_2,\alpha\alpha}(t_2) - G_{gg,gg}(t_2))] + 4D[\mu_{a_1g}\mu_{\alpha a_1}^3 G_{a_1a_1,a_1a_1}(t_2) + \mu_{a_2g}\mu_{\alpha a_2}\mu_{\alpha a_1}^2 G_{a_1a_1,a_2a_2}(t_2)$$
$$- \mu_{a_1g}\mu_{\alpha a_1}\mu_{a_2g}^2 G_{a_2a_2,a_1a_1}(t_2) - \mu_{a_2g}^3\mu_{\alpha a_2} G_{a_2a_2,a_2a_2}(t_2)] + 2D[\mu_{a_1g}(\mu_{\alpha a_1}\mu_{\alpha a_2}^2 - \mu_{a_2g}^2\mu_{\alpha a_1}) + \mu_{a_2g}(\mu_{\alpha a_1}^2\mu_{\alpha a_2} - \mu_{a_1g}^2\mu_{\alpha a_2})] G_{a_2a_1,a_2a_1}(t_2). \tag{B.2}$$

The difference between the line shape of peak P_1 and P_2 can be understood from the response $\bar{S}_{P_i}(\Omega_1 = 2E,\ t_2 = 0,\ t_3)$ ($i \in \{1,2,3\}$). Peak P_1 at $t_2 = 0$ fs is given by

$$\bar{S}_{P_1}(\Omega_1 = 2E,\ t_2 = 0,\ t_3) = \frac{1}{k_A + \gamma_{g\alpha}^{pd}}[c_1 \cdot G_{\alpha a_2,\alpha a_2}(t_2) - c_2 \cdot G_{a_1g,a_1g}(t_2)]$$
$$= \frac{1}{k_A + \gamma_{g\alpha}^{pd}}[c_1 \cdot e^{-i(\omega_{a_1g} + \Gamma_A)t_3} - c_2 \cdot e^{-i(\omega_{a_1g} + \Gamma_R)t_3}] \tag{B.3}$$

where $c_1 = 2D[D\mu_{\alpha a_2}^2 + 2\mu_{a_2g}\mu_{\alpha a_2}^3 + \mu_{a_2g}\mu_{\alpha a_1}^2\mu_{\alpha a_2} + \mu_{a_1g}\mu_{\alpha a_2}^2\mu_{\alpha a_1}]$, $c_2 = 2D[D\mu_{a_1g}^2 + 2\mu_{a_1g}^3\mu_{\alpha a_1} + \mu_{a_2g}^2\mu_{\alpha a_1}\mu_{a_1g} + \mu_{a_1g}^2\mu_{\alpha a_1}\mu_{a_2g}]$, $D = \mu_{a_1g}\mu_{\alpha a_1} + \mu_{a_2g}\mu_{\alpha a_2}$, $\Gamma_A = \frac{1}{2}k_{a_2\to a_1} + k_A + \gamma_{\alpha a_2}^{pd}$, and $\Gamma_R = \frac{1}{2}k_{a_1\to a_2} + \gamma_{ga_1}^{pd}$. Peak P_2 reads

$$\bar{S}_{P_2}(\Omega_1 = 2E,\ t_2 = 0,\ t_3) = \frac{1}{k_A + \gamma_{g\alpha}^{pd}}[c_3 \cdot G_{\alpha a_1,\alpha a_1}(t_2) - c_4 \cdot G_{a_2g,a_2g}(t_2)] = \frac{1}{k_A + \gamma_{g\alpha}^{pd}}[c_3 \cdot e^{-i(\omega_{a_2g} + \bar{\Gamma}_A)t_3} - c_4 \cdot e^{-i(\omega_{a_2g} + \bar{\Gamma}_R)t_3}] \tag{B.4}$$

where $c_3 = 2D[D\mu_{\alpha a_1}^2 + 2\mu_{a_1g}\mu_{\alpha a_1}^3 + \mu_{a_1g}\mu_{\alpha a_2}^2\mu_{\alpha a_1} + \mu_{a_2g}\mu_{\alpha a_1}^2\mu_{\alpha a_2}]$, $c_4 = 2D[D\mu_{a_2g}^2 + 2\mu_{a_2g}^3\mu_{\alpha a_2} + \mu_{a_1g}^2\mu_{\alpha a_2}\mu_{a_2g} + \mu_{a_2g}^2\mu_{\alpha a_2}\mu_{a_1g}]$, $\bar{\Gamma}_A = \frac{1}{2}k_{a_1\to a_2} + k_A + \gamma_{\alpha a_1}^{pd}$ and $\bar{\Gamma}_R = \frac{1}{2}k_{a_2\to a_1} + \gamma_{ga_2}^{pd}$.

Both peaks are thus given by negative interference of Lorentzians, which magnitudes have a complicated dependency on the transition dipole moments. However, P_1 is given by the difference between $G_{\alpha a_2,\alpha a_2}(t)$ and $G_{a_1g,a_1g}(t)$. $G_{\alpha a_2,\alpha a_2}(t)$ is both broadened by the lifetime of excitonic state $|a_2\rangle$ and the annihilation rate k_A. $G_{a_1g,a_1g}(t)$ is effectively solely broadened by the dephasing element $\gamma_{a_1g}^{pd}$ ($k_{a_1\to a_2} \approx 0$). The subtraction of these two Green's functions results in the observed double peak structure of peak P_1. Peak P_2 is given by the subtraction of $G_{\alpha a_1,\alpha a_1}(t_3)$ and $G_{a_2g,a_2g}(t_3)$. These two Green's functions are broadened by the annihilation rate k_A and the transport rate $k_{a_2\to a_1}$, respectively, and their respective pure dephasing elements. This results, for the parameters used in Fig. 4(b), into a roughly equal broadening and the peak structure does not deviate dramatically from the expected star shape. A slight tilt, however, is noticeable.

Appendix C. Isotropic ensembles of molecular dimers with arbitrary orientation of constituents

In the present Appendix we allow for more general geometric configurations of molecules inside the aggregate. We consider a molecular dimer with arbitrary dipoles $\vec{d}_1$ and $\vec{d}_2$, supplemented with Förster transport dynamics. In the molecular frame the tensor components are as follows:

$$R^{\phi\epsilon\delta\gamma\beta\alpha}(t_2) = \langle\langle \mu|^{\phi} \breve{\mu}^{(+),\epsilon} \breve{\mathscr{G}}(t_2) \breve{\mu}^{(+),\delta} \breve{\mu}^{(+),\gamma} \breve{\mu}^{(-),\beta} \breve{\mu}^{(-),\alpha} |gg\rangle\rangle$$
$$= (d_2^{\phi} d_2^{\epsilon} + d_1^{\phi} d_1^{\epsilon}) A(t_2) (d_1^{\delta} d_2^{\gamma} + d_2^{\delta} d_1^{\gamma})(d_1^{\beta} d_2^{\alpha} + d_2^{\beta} d_1^{\alpha})$$
$$+ (d_1^{\phi} d_1^{\epsilon} - d_2^{\phi} d_2^{\epsilon}) B(t_2) (d_1^{\delta} d_2^{\gamma} + d_2^{\delta} d_1^{\gamma})(d_1^{\beta} d_2^{\alpha} + d_2^{\beta} d_1^{\alpha}). \tag{C.1}$$

where we defined the annihilation component $A(t) \coloneqq (G_{\alpha\alpha,\alpha\alpha}(t) - G_{gg,gg}(t))$ and the transport component

$$B(t) \coloneqq G_{22,22}(t) - G_{11,11}(t) - G_{11,22}(t) + G_{22,11}(t_2) - G_{22,\alpha\alpha}(t) + G_{11,\alpha\alpha}(t).$$

The aggregates usually occur in isotropic ensembles. The rotational averages of response functions are obtained by a linear combinations of molecular frame tensors

$$\mathscr{R}_{ijklmn} = \sum_{\alpha\beta\gamma\delta\epsilon\phi} I_{ijklmn}^{\alpha\beta\gamma\delta\epsilon\phi} R^{\alpha\beta\gamma\delta\epsilon\phi},$$

where the coefficients I are given in Table II and Eq. (20) of reference [36]. We notice that for all 15 isotropic components [36] of the signal

$$R^{\phi\phi\gamma\gamma\alpha\alpha} = [4(d_1^2 + d_2^2)A(t_2) + 4(d_1^2 - d_2^2)B(t_2)](\vec{d}_1 \cdot \vec{d}_2)^2$$

$$R^{\phi\phi\alpha\gamma\gamma\alpha} = R^{\phi\phi\gamma\alpha\gamma\alpha} = [2(d_1^2 + d_2^2)A(t_2) + 2(d_1^2 - d_2^2)B(t_2)][(d_1^2 + d_2^2) + (\vec{d}_1 \cdot \vec{d}_2)^2]$$

$$R^{\phi\epsilon\phi\epsilon\alpha\alpha} = R^{\phi\epsilon\epsilon\phi\alpha\alpha} = R^{\phi\epsilon\alpha\alpha\epsilon\phi} = R^{\phi\epsilon\alpha\alpha\phi\epsilon} = [4(d_1^2 + d_2^2)A(t_2) + 4(d_1^2 - d_2^2)B(t_2)](\vec{d}_1 \cdot \vec{d}_2)^2$$

$$R^{\phi\epsilon\phi\alpha\epsilon\alpha} = R^{\phi\epsilon\phi\alpha\alpha\epsilon} = R^{\phi\epsilon\alpha\phi\alpha\epsilon} = R^{\phi\epsilon\alpha\phi\epsilon\alpha} = R^{\phi\epsilon\alpha\epsilon\phi\alpha} = R^{\phi\epsilon\alpha\epsilon\alpha\phi} = R^{\phi\epsilon\epsilon\alpha\alpha\phi} = [(d_1^2 + d_2^2)A(t_2) + (d_1^2 - d_2^2)B(t_2)][d_1^2 d_2^2 + 3(\vec{d}_1 \cdot \vec{d}_2)^2]$$

the transport components $B(t)$ vanishes for $d_1^2 = d_2^2$. The above derivation applies for Förster dynamics, nevertheless numerical simulations we made suggest the total signal vanishes also for Redfield type of dynamics from isotropic ensemble of dimers with $d_1^2 = d_2^2$.

References

[1] V. May, Kinetic theory of exciton-exciton annihilation, J. Chem. Phys. 140 (2014) 054103.
[2] M.A. Baldo, R.J. Holmes, S.R. Forrest, Prospects for electrically pumped organic lasers, Phys. Rev. B 66 (2002) 035321.
[3] G.M. Akselrod, Y.R. Tischler, E.R. Young, D.G. Nocera, V. Bulovic, Exciton-exciton annihilation in organic polariton microcavities, Phys. Rev. B 82 (2010) 113106.
[4] M.G. Muller, P. Lambrev, M. Reus, E. Wientjes, R. Croce, A.R. Holzwarth, Singlet energy dissipation in the photosystem II light-harvesting complex does not involve energy transfer to carotenoids, ChemPhysChem 11 (2010) 1289–1296.
[5] S. Gelinas, J. Kirkpatrick, I.A. Howard, K. Johnson, M.W. Wilson, G. Pace, R.H. Friend, C. Silva, Recombination dynamics of charge pairs in a push-pull polyfluorene-derivative, J. Phys. Chem. B 117 (2013) 4649–4653.
[6] I.B. Martini, A.D. Smith, B.J. Schwartz, Exciton-exciton annihilation and the production of interchain species in conjugated polymer films: comparing the ultrafast stimulated emission and photoluminescence dynamics of MEH-PPV, Phys. Rev. B 69 (2004) 035204.
[7] F. Fennel, S. Lochbrunner, Exciton-exciton annihilation in a disordered molecular system by direct and multistep Förster transfer, Phys. Rev. B 92 (2015) 140301.
[8] T. Nguyen, I.B. Martini, J. Liu, B.J. Schwartz, Controlling interchain interactions in conjugated polymers: the effects of chain morphology on exciton-exciton annihilation and aggregation in MEH-PPV films, J. Phys. Chem. B 104 (2000) 237–255.
[9] R. Berera, R. van Grondelle, J.T. Kennis, Ultrafast transient absorption spectroscopy: principles and application to photosynthetic systems, Photosynth. Res. 101 (2009) 105–118.
[10] D.M. Jonas, Two-dimensional femtosecond spectroscopy, Annu. Rev. Phys. Chem. 54 (2003) 425–463.
[11] L. Valkunas, I.H.M. van Stokkum, R. Berera, R. van Grondelle, Exciton migration and fluorescence quenching in LHCII aggregates: target analysis using a simple nonlinear annihilation scheme, Chem. Phys. 357 (2009) 17–20.
[12] G. Trinkunas, J.L. Herek, T. Polivka, V. Sundstrom, T. Pullerits, Exciton delocalization probed by excitation annihilation in the light-harvesting antenna LH2, Phys. Rev. Lett. 86 (2001) 4167–4170.
[13] F. Šanda, S. Mukamel, Cooperative effects in photon statistics of molecular dimers with spectral diffusion, J. Chem. Phys. 124 (2006) 124103.
[14] A. Nemeth, F. Milota, T. Mancal, T. Pullerits, J. Sperling, J. Hauer, H.F. Kauffmann, N. Christensson, Double-quantum two-dimensional electronic spectroscopy of a three-level system: experiments and simulations, J. Chem. Phys. 133 (2010) 094505.
[15] B. Brüggemann, T. Pullerits, Nonperturbative modeling of fifth-order coherent multidimensional spectroscopy in light harvesting antennas, New J. Phys. 13 (2011) 025024.
[16] J. Dostál, F. Fennel, F. Koch, S. Herbst, F. Wurthner, T. Brixner, Direct observation of exciton-exciton interactions, Nat. Commun. 9 (2018) 2466.
[17] J. Süß, J. Wehner, J. Dostál, T. Brixner, V. Engel, Mapping of exciton-exciton annihilation in a molecular dimer via fifth-order femtosecond two-dimensional spectroscopy, J. Chem. Phys. 150 (2019) 104304.
[18] R. Tempelaar, T.L.C. Jansen, J. Knoester, Exciton-exciton annihilation is coherently suppressed in H-aggregates, but not in J-aggregates, J. Phys. Chem. Lett. 8 (2017) 6113–6117.
[19] B. Brüggemann, N. Christensson, T. Pullerits, Temperature dependent exciton – exciton annihilation in the LH2 antenna complex, Chem. Phys 357 (2009) 140–143.
[20] R. Kubo, Statistical-mechanical theory of irreversible processes. I. general theory and simple applications to magnetic and conduction problems, J. Phys. Soc. Jpn. 12 (1957) 570–586.
[21] S. Mukamel, Principles of Nonlinear Optical Spectroscopy, Oxford University Press, 1995.
[22] D. Abramavicius, B. Palmieri, D.V. Voronine, F. Šanda, S. Mukamel, Coherent multidimensional optical spectroscopy of excitons in molecular aggregates; quasiparticle versus supermolecule perspectives, Chem. Rev. 109 (2009) 2350–2408.
[23] U. Fano, Description of states in quantum mechanics by density matrix and operator techniques, Rev. Mod. Phys. 29 (1957) 570–586.
[24] R.W. Zwanzig, Statistical mechanics of irreversibility, Lect. Theor. Phys. (Boulder) 3 (1960) 106–141.
[25] V. Perlík, F. Šanda, Vibrational relaxation beyond the linear damping limit in two-dimensional optical spectra of molecular aggregates, J. Chem. Phys. 147 (2017) 084104.
[26] T. Förster, Zwischenmolekulare Energiewanderung und Fluoreszenz, Ann. Phys. (Berlin) 437 (1948) 55–75.
[27] A.G. Redfield, On the theory of relaxation processes, IBM J. Res. Dev. 1 (1957) 19–31.
[28] J. Frenkel, On the transformation of light into heat in solids, II. Phys. Rev 37 (1931) 1276–1294.
[29] A.O. Caldeira, A.J. Leggett, Path integral approach to quantum brownian motion, Physica A 121 (1983) 587–616.
[30] L. Van Hove, Quantum-mechanical perturbations giving rise to a statistical transport equation, Physica 21 (1954) 517–540.
[31] V. Gorini, A. Kossakowski, E.C.G. Sudarshan, Completely positive semigroups of N-level systems, J. Math. Phys. 17 (1976) 821–825.
[32] G. Lindblad, On the generators of quantum dynamical semigroups, Commun. Math. Phys. 48 (1976) 119–130.
[33] L. Valkunas, G. Trinkunas, V. Liuolia, R. van Grondelle, Nonlinear annihilation of excitations in photosynthetic systems, Biophys. J. 69 (1995) 1117–1129.
[34] V. Perlík, J. Hauer, F. Šanda, Finite pulse effects in single and double quantum spectroscopies, J. Opt. Soc. Am. 34 (2017) 430–439.
[35] Thanh Nhut Doa, L. Chenb, A.K. Belyaevc, H. Tana, M.F. Gelin, Pulse-shape effects in fifth-order multidimensional optical spectroscopy, Chem. Phys. 515 (2018) 119–128.
[36] D.L. Andrews, T. Thirunamachandran, On three-dimensional rotational averages, J. Chem. Phys. 67 (1977) 5026–5033.

B. Full Length Article of Section 3.2

THE JOURNAL OF PHYSICAL CHEMISTRY Letters

pubs.acs.org/JPCL Letter

Annihilation Dynamics of Molecular Excitons Measured at a Single Perturbative Excitation Energy

C. Heshmatpour, P. Malevich, F. Plasser, M. Menger, C. Lambert, F. Šanda, and J. Hauer*

Cite This: J. Phys. Chem. Lett. 2020, 11, 7776−7781 Read Online

ACCESS | Metrics & More | Article Recommendations | Supporting Information

ABSTRACT: Exciton−exciton annihilation (EEA) is a ubiquitous phenomenon, which may limit the efficiency of photovoltaic devices. Conventional methods of determining EEA time scales rely on measuring the intensity dependence of third-order signals. In this work, we directly extract the annihilation rate of molecular excitons in a covalently joined molecular trimer without the need to perform and analyze intensity dependent data by employing fifth-order coherent optical spectroscopy signals emitted into $\pm 2\vec{k}_1 \mp 2\vec{k}_2 + \vec{k}_3$ phase matching directions. Measured two-dimensional line shapes and their time traces are analyzed in the framework of the many-body version of the Frenkel exciton model, extended to incorporate annihilation dynamics. Combining double-sided Feynman diagrams with explicit simulations of the fifth-order response, we identify a single peak as a direct reporter of EEA. We retrieve an annihilation time of 30 fs for the investigated squaraine trimer.

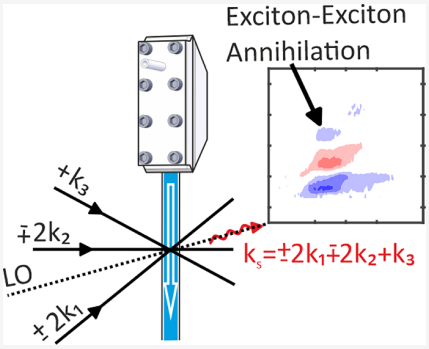

Exciton−exciton annihilation (EEA) is the process of excitation energy quenching by fusion of two neighboring excitons followed by nonradiative relaxation.[1,2] EEA thus hampers the efficient conversion from light into usable energy in organic solar cells[3,4] and is a limiting factor for lasers based on organic thin films[5] by setting an upper limit for the exciton density.[6] However, the efficient removal of excess energy via EEA is not solely undesirable as it, e.g., plays an important role in the photoprotection of natural light harvesting complexes.[7−10] EEA additionally explains the unconventional photocurrent generation efficiency of van der Waals heterostructure devices through the creation of hot holes.[11] The most widespread application of EEA is to determine exciton diffusion constants as excitons need to migrate to adjacent sites to annihilate.[12,13] Time-resolving annihilation dynamics thus allows us on the one hand to identify undesirable loss channels and on the other hand to obtain insights into the energy level structure of the material under study.

The investigation of annihilation dynamics is, however, experimentally challenging as it is commonly studied as an intensity dependent contribution to time-resolved third-order signals.[14,15] Such approaches are prone to experimental artifacts at high excitation intensities, complicating the interpretation of the data. Fifth-order 2D-electronic spectroscopy (R^5-2D) line shapes detected along the $\vec{k}_S = \pm 2\vec{k}_1 \mp 2\vec{k}_2 + \vec{k}_3$ phase matching directions overcome this problem as biexciton dynamics, such as EEA, contribute to the signal already at perturbative level of excitation density.[16−18] The general temporal evolution of the R^5-2D signal still contains both exciton transport and annihilation contributions. In a recent publication,[19] we formally proved that spectral integration of fifth-order signals over both excitation and emission frequencies eliminates the dependence on single exciton transport rates for homo-aggregates with aligned transition dipole moment geometry of arbitrary length. The spectrally integrated R^5-2D signal of such aggregates is thus a measure for tracking and pinpointing annihilation dynamics of molecular excitons at a single perturbative excitation density.

In this Letter we extend our efforts toward aggregates with non-aligned transition dipoles and present a joint experimental and theoretical study of the R^5-2D signal of a squaraine homotrimer. To extract the annihilation dynamics of the trimer, we investigate the observed line shapes in detail and identify a single peak as a direct reporter of EEA.

The experimental setup for measuring the R^5-2D ($\vec{k}_S = \pm 2\vec{k}_1 \mp 2\vec{k}_2 + \vec{k}_3$) signals is a fully non-collinear 50 kHz shot-to-shot detected 2D electronic spectroscopy setup with sub 10 fs pulses in the visible. Our approach relies on conventional optics and represents an extension of our previously published setup[20] for measuring R^3-2D ($\vec{k}_S = \pm \vec{k}_1 \mp \vec{k}_2 + \vec{k}_3$) signals. Figure 1A depicts the modified phase matching geometry enabling us to detect both R^3- and R^5-2D signals within one experimental setup. A single 2D map was acquired in under 4 s by employing the 50 kHz shot-to-shot broadband detection

Received: July 14, 2020
Accepted: August 26, 2020
Published: August 26, 2020

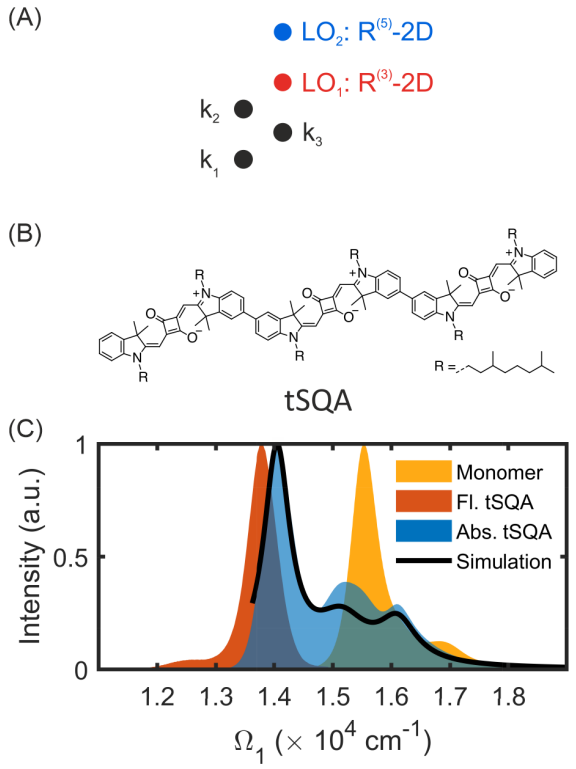

Figure 1. (A) Phase matching geometry used for heterodyne detection of R^3- and R^5-2D signals of tSQA with local oscillators LO_1 and LO_2, respectively. Rephasing and non-rephasing signals were measured by interchanging the time ordering of pulses k_1 and k_2. (B) tSQA's molecular structure. (C) Normalized linear spectra of tSQA and its monomer in mesitylene and toluene solution, respectively. The black solid line depicts the simulation of the absorption spectrum of tSQA employing the Frenkel exciton model described in the text.

and rapid scanning of coherence time t_1. A detailed explanation of the setup and the measurement procedure is presented in section 1 of the Supporting Information.

Measurements were performed on a squaraine-trimer (tSQA, see Figure 1B) in mesitylene solution. This solvent was chosen for its high viscosity and low vapor pressure. Both parameters are important, as all time-resolved measurements were performed in a window-free jet.[21] tSQA was chosen as a paradigmatic strongly coupled trimeric system with a high absorption cross section and spectra shown in Figure 1C.[22] Furthermore, a trimer is the smallest aggregate allowing for the full wealth of relaxation channels potentially affecting R^5-2D signals, including biexciton transport, while the system of electronic states required for the simulations of the nonlinear signals is sufficiently small to hold a full many-body excitonic treatment.[19]

The experimental data of tSQA (absorption, R^3-2D, and R^5-2D) are thus compared against simulations employing a Frenkel exciton trimer model[23] developed in ref 19. Briefly, each squaraine molecule is considered as a two-level system with site energy E. Electronic coupling is considered between all chromophores. Strong coupling between the squaraine molecules requires us to assume Redfield type transport dynamics[24] between delocalized many-body eigenstates, such as single-exciton states $|a_i\rangle$ and biexciton states $|\alpha_i\rangle$ ($i \in \{1, 2, 3\}$), obtained by diagonalization of the Frenkel exciton Hamiltonian. A schematic energy level diagram is shown in Figure 2A. EEA dynamics, which will be shown to be essential for the simulation of the R^5-2D data, are assumed to occur when neighboring sites are occupied. EEA then leads to

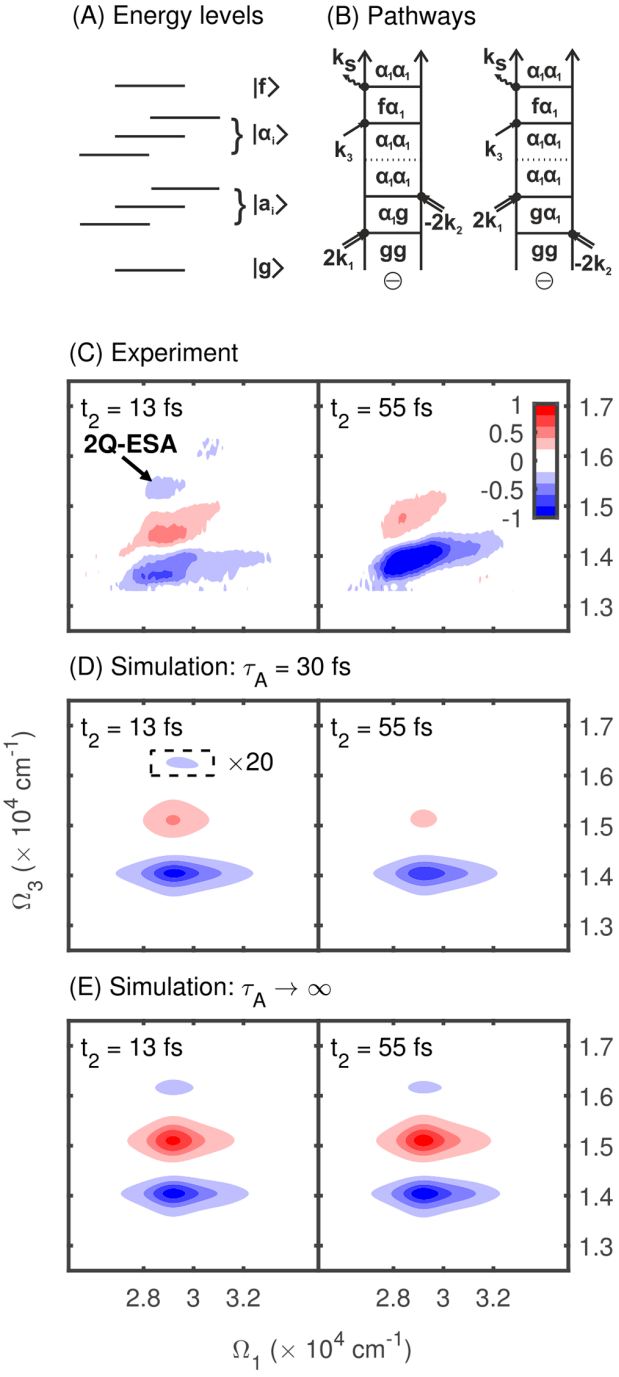

Figure 2. (A) tSQA energy level diagram. (B) Double-sided Feynman diagrams of the predominant contributions to peak 2Q-ESA. (C) Experimental R^5-2D spectra of tSQA for two different waiting times. (D, E) Simulations of the R^5-2D signal for the same waiting times as in (C), for an annihilation time τ_A of 30 fs (D) and no annihilation between excitons (E). The peak in the dotted square is magnified by a factor of 20 for better visibility. The disappearance of the top negative peak, termed 2Q-ESA, for long waiting times is a direct reporter of EEA (see text).

https://dx.doi.org/10.1021/acs.jpclett.0c02141
J. Phys. Chem. Lett. 2020, 11, 7776−7781

unidirectional transfer between manifolds, i.e., from triexciton states $|f\rangle \rightarrow |\alpha\rangle$ and $|\alpha\rangle \rightarrow |a\rangle$. The annihilation kinetics are Markovian and identical for both chromophore pairs. The linear and non-linear response of the trimer is calculated in the impulsive limit employing Kubo theory.[25] We implemented a procedure to rotationally average absorption, R^3- and R^5-2D signals along ref 26. No additional line-broadening procedure has been applied, the calculated line shapes are thus purely homogeneous. Liouville space pathways,[27] details, and the parametrization of the model can be found in the Supporting Information.

The Frenkel exciton Hamiltonian (site energy and couplings) is parametrized by quantum chemical calculations with restrictions set by the tSQA absorption spectrum (see Figure 1C). It displays a pronounced peak at 14100 cm^{-1}, a weaker peak at 16100 cm^{-1}, and a spectrally broad feature around 15000−16000 cm^{-1}. The transition strength from the ground state into these single exciton states depends on the relative orientation of the transition dipoles associated with each chromophore and is thus linked to the trimer's conformation.[28] From tSQA's molecular structure, shown in Figure 1B, one can expect the presence of several conformers, as rotations around the single bond connecting the monomeric units is conceivable. We thus performed exploratory quantum chemical calculations at the PBE0/SVP level of theory,[29,30] suggesting seven relevant conformers at room temperature. These can be grouped into linear conformers, analogous to the structure shown in Figure 1B, as well as structures with one and two kinks. All conformers are depicted in section 4 of the Supporting Information. We further computed the electronic couplings between the three chromophores of every structure by employing time-dependent density functional theory[31,32] according to the scheme of Iozzi et al.[33,34] implemented in Gaussian 16.[35] A comparison between single exciton level splittings of all conformers, observed in theory and experiment, revealed that the quantum chemistry based evaluations slightly underestimate the couplings. We thus scaled the couplings by 16% but kept their relative proportion. The scaled coupling data can be found in Table 2 of the Supporting Information.

An effort to simultaneously fit all spectra, using all suggested conformers with their associated coupling data and transition dipole geometries, revealed that the complete data set can be adequately reproduced by an equal-weight linear combination employing the two conformers possessing one kink in their structure (structure numbers 5 and 6 in Figure 4 of the Supporting Information). The resulting absorption spectrum is shown in Figure 1C as a solid black line, which is in good agreement with the experiment. Differences between theory and experiment at the broad central feature are attributed to our calculation omitting the minor vibronic feature visible in the monomer spectrum. The extent of vibronic contributions to the central broad peak of the trimer's absorption spectrum can be estimated by projecting the local 1300 cm^{-1} vibrations onto the lowest exciton $|a_1\rangle$. We estimate the amount of vibronic mixing by $d^2\sum_{i=1}^{3}|\langle i|a_1\rangle|^4$, where $d^2 = 0.125$ is the monomer Huang−Rhys factor. We find that the vibronic progression contributes less than 5% of the transition strength from the main absorption band for all structures, translating into a 10% vibronic contribution to the central peak volume. This is consistent with the observed deviation between experiment and theory as depicted in Figure 1C.

Fitting the absorption spectrum of tSQA adjusts, besides the Frenkel exciton Hamiltonian, the total peak broadenings as a sum of all pure dephasing and transport related broadenings. The R^3-2D signal of tSQA is instrumental to distinguish between the two broadening mechanisms, by measuring dynamics inside the single exciton manifold. To keep the number of parameters tractable, we derive the relaxation and decoherence rates from the environmental spectral density composed of an underdamped intramolecular mode at 1300 cm^{-1} identified in the monomer absorption spectrum (see Figure 1C) and a Lorentzian density for other vibrations and solvent modes. We thus used the R^3-2D signal to parametrize the spectral densities, or in other words to ensure that our parametrization captures the transport dynamics of tSQA. The result is depicted in section 5 of the Supporting Information.

As we now established a model for the transport dynamics of tSQA, we can tackle the non-linear exciton dynamics, which can be extracted from R^5-2D spectra. The respective signal of tSQA is depicted in Figure 2C for two different waiting times. It shows an overall three peak structure, i.e., two negative and one positive peak. We discussed a similar peak structure in ref 19 for a strongly coupled model homo-trimer with H-type coupling. The non-aligned case of tSQA is slightly different as additional transitions are optically allowed. However, we confirmed numerically that only one transition between manifolds $|g\rangle \rightarrow |a\rangle$, $|a\rangle \rightarrow |\alpha\rangle$ and $|\alpha\rangle \rightarrow |f\rangle$ is dominant in each case. The electronic coupling between chromophores 1 and 3 in tSQA is small compared to the couplings between neighboring sites, which means that the level scheme of tSQA can be approximated by the nearest neighbor Hamiltonian of ref 19. We employ an excitonic coupling $J \approx 700$ cm^{-1} as a good approximation for both relevant structures. The dominant transitions are from ground to the lowest single exciton eigenstate $|a_1\rangle$ (transition frequency $\omega_{ga_1} \approx E - \sqrt{2}J \approx 14110$ cm^{-1}), from $|a_1\rangle$ to the lowest biexciton state $|\alpha_1\rangle$ ($\omega_{a_1\alpha_1} \approx E \approx 15100$ cm^{-1}) and from $|\alpha_1\rangle$ to triexciton state $|f\rangle$ ($\omega_{\alpha_1 f} \approx E + \sqrt{2}J \approx 16090$ cm^{-1}). Three peaks are thus expected to appear at positions $(\Omega_1, \Omega_3) = (\omega_{g\alpha_1}, \omega_{ga_1})$, $(\omega_{g\alpha_1}, \omega_{a_1\alpha_1})$ and $(\omega_{g\alpha_1}, \omega_{\alpha_1 f})$, where $\omega_{g\alpha_1} \approx 2E - \sqrt{2}J \approx 29210$ cm^{-1} is the frequency of coherence $|g\alpha_1\rangle\rangle$. The lowest negative feature thus stems predominantly from an interference between pathways in coherence $|a_1 g\rangle\rangle$ during t_3, the positive middle feature predominantly from pathways ending in $|\alpha_1 a_1\rangle\rangle$ and the negative feature at 15400 cm^{-1}, termed 2Q-ESA in Figure 2C, predominantly from pathways in coherence $|f\alpha_1\rangle\rangle$ (see Figure 2B). The numbers obtained from the nearest neighbor model are in agreement with the simulation depicted in Figure 2D, which accounts for couplings between all units. The experimental peak positions in Figure 2C are, however, slightly shifted down in Ω_3 for early times compared to the nearest neighbor model and the simulations shown in Figure 2D. Quantitative discrepancies in peak magnitudes between experiment and simulation (Figure 2D) are attributed to overlaps of too-far reaching wings of simulated peaks, in other words to the Markovian approximation of the applied system kinetics. Despite these minor differences between Figure 2C,D, one sees that the electronic model describes the overall three-peak structure and the varying intensities with increasing waiting time with good agreement. To extract the annihilation rate of tSQA from the signal, we notice that the dominant diagrams for 2Q-ESA depicted in Figure 2B require population of the biexcitonic state during t_2. The strength of this negative

https://dx.doi.org/10.1021/acs.jpclett.0c02141
J. Phys. Chem. Lett. 2020, 11, 7776−7781

contribution is thus a direct measure of population inside the biexciton manifold. Its disappearance directly relates to population relaxation out of the biexciton manifold, which determines the time scale for EEA.[36] In Figure 2E we simulated the R^5-2D spectrum of tSQA without EEA to verify that the behavior of the 2Q-ESA peak is a suitable reporter of EEA dynamics. The resulting 2D maps are distinctly changed, showing no major changes in the first few femtoseconds, despite the slight broadening along Ω_1 of the lowest negative and the positive peak attributed to ultrafast excitation energy transfer. However, the 2Q-ESA peak shows no change, as population persists inside the biexciton manifold.

Figure 3 depicts the experimental and simulated temporal evolution of the 2Q-ESA-peak's intensity in more detail. The

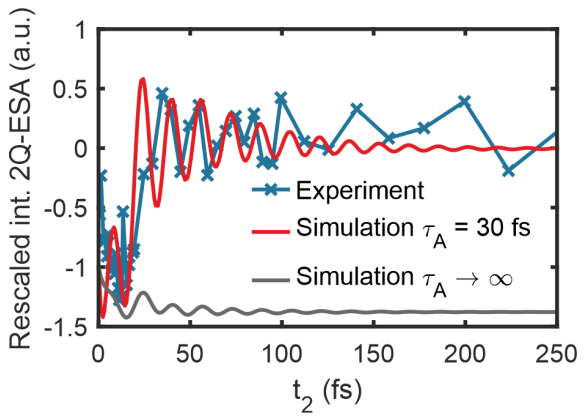

Figure 3. Experimental (blue) and simulated (red, τ_A = 30 fs; black, no EEA) intensity of peak 2Q-ESA versus the waiting time t_2. The intensity is rescaled to start at −1 and to approach zero by subtracting an average value at long delays. Comparing all time traces, we can associate the fast rise of the signal to EEA.

experimental signal shows fast oscillations during pulse overlap[37,38] and up to 20 fs followed by a rapid rise progressing into an oscillatory behavior around its asymptotic value. The rapid rise of the signal is missing in simulations omitting annihilation, and we thus assign it to EEA. The best agreement between theory and experiment in terms of 2D line shapes and temporal traces of the 2Q-ESA peak (see Figure 3) is found with an annihilation time of 30 fs. The sensitivity of this multicriterial fit against τ_A is quantified by the mean of the residuals (MOR) of the fitted traces in Figure 3 as compared to the experimental data; the choice of τ_A = 30 fs leads to a MOR of 0.01 with the residuals normally distributed around zero with no systematic deviations. Setting τ_A to 50 fs leads to a 6-fold increase in MOR and a deviation of the residual from a zero average value (not shown). The 30 fs annihilation time scale is in agreement with the annihilation time of 28 fs found for a squaraine heterodimer (see the Supporting Information of ref 18) following the temporal behavior of a peak in fluorescence detected 2D-ES.[39] The oscillations in the simulated signal (τ_A = 30 fs) in Figure 3 are attributed to an excitonic beating in the first manifold, in particular between states $|a_1\rangle$ and $|a_3\rangle$ (see pathways R10, NR10, R8, and NR8 in Figure 2 of the Supporting Information). In this Letter we presented a direct study of ultrafast annihilation dynamics of molecular excitons via R^5-2D spectroscopy. Spectroscopic measurements were performed on tSQA, a molecular trimer. The measured line shapes and time traces were explained by a developed theoretical model employing a Frenkel exciton Hamiltonian and Redfield theory for exciton dynamics, extended to incorporate EEA. Excitonic coupling and molecular structure were parametrized using quantum chemistry. The electronic model reproduces absorption, R^3-2D (see the Supporting Information), and R^5-2D spectra with good agreement. A possible, but computationally demanding, extension of the electronic model toward a vibronic description[40,41] is left for future research. Employing double-sided Feynman diagrams, we identified a single peak as a reporter of EEA. Our analysis was consolidated by explicit simulations of the fifth-order response of tSQA allowing and prohibiting EEA. The simulated time traces clearly show that the fast rise observed in the experiment is directly connected to EEA. Fitting the experimental data with our model we could extract an annihilation time of 30 fs. The obtained time constant is in accordance with measurements performed on aggregates of similar size, employing fluorescence detected 2D-ES (see the Supporting Information of ref 18). In conclusion, we showed that R^5-2D presents a robust way of detecting biexciton dynamics, such as EEA, and thus circumvents the need to perform and analyze intensity dependent experiments.

■ ASSOCIATED CONTENT

Supporting Information

The Supporting Information is available free of charge at https://pubs.acs.org/doi/10.1021/acs.jpclett.0c02141.

Experimental setup, model for optical dynamics of tSQA, double-sided Feynman diagrams for R^3- and R^5-2D, tSQA structures, R^3-2D signal of tSQA (PDF)

■ AUTHOR INFORMATION

Corresponding Author

J. Hauer − *Professur für Dynamische Spektroskopien, Fakultät für Chemie, Technische Universität München, D-85748 Garching b. München, Germany;* orcid.org/0000-0002-6874-6138; Email: juergen.hauer@tum.de

Authors

C. Heshmatpour − *Institute of Physics, Faculty of Mathematics and Physics, Charles University, Prague 121 16, Czech Republic; Professur für Dynamische Spektroskopien, Fakultät für Chemie, Technische Universität München, D-85748 Garching b. München, Germany*

P. Malevich − *Professur für Dynamische Spektroskopien, Fakultät für Chemie, Technische Universität München, D-85748 Garching b. München, Germany*

F. Plasser − *Department of Chemistry, Loughborough University, Loughborough LE11 3TU, United Kingdom;* orcid.org/0000-0003-0751-148X

M. Menger − *Faculty of Science and Engineering, Zernike Institute for Advanced Materials, University of Groningen, 9747AG Groningen, The Netherlands*

C. Lambert − *Institut für Organische Chemie, Center for Nanosystems Chemistry, Universität Würzburg, 97074 Würzburg, Germany;* orcid.org/0000-0002-9652-9165

F. Sanda − *Institute of Physics, Faculty of Mathematics and Physics, Charles University, Prague 121 16, Czech Republic;* orcid.org/0000-0003-2416-8804

Complete contact information is available at: https://pubs.acs.org/10.1021/acs.jpclett.0c02141

https://dx.doi.org/10.1021/acs.jpclett.0c02141
J. Phys. Chem. Lett. 2020, 11, 7776−7781

Notes

The authors declare no competing financial interest.

■ ACKNOWLEDGMENTS

J.H., P.M., and C.H. thank Harald Ceymann for providing and synthesizing the sample. J.H. and C.H. acknowledge support by Deutsche Forschungsgemeinschaft (DFG, German Research Foundation) through TUM International Graduate School of Science and Engineering (IGSSE), GSC 81, and funding by DFG under Germany's Excellence Strategy (EXC 2089/1-390776260). F.Š. and C.H. acknowledge support by Czech Science Foundation (Grant No. 17-22160S). Mobility is supported by project "Exciton-exciton annihilation probed by nonlinear spectroscopy" (MSMT Grant No. 8J19DE009, DAAD-Projekt 57444962). P.M. acknowledges the support of the Alexander von Humboldt Foundation as well as the donor, the Federal Ministry for Education and Research.

■ REFERENCES

(1) Gaididei, Y. B.; Onipko, A. I. A Kinetic Theory of Incoherent Exciton Annihilation. *Mol. Cryst. Liq. Cryst.* **1980**, *62*, 213−235.
(2) May, V. Kinetic theory of exciton-exciton annihilation. *J. Chem. Phys.* **2014**, *140*, No. 054103.
(3) Tzabari, L.; Zayats, V.; Tessler, N. Exciton annihilation as bimolecular loss in organic solar cells. *J. Appl. Phys.* **2013**, *114*, 154514.
(4) McDonough, T. J.; Zhang, L.; Roy, S. S.; Kearns, N. M.; Arnold, M. S.; Zanni, M. T.; Andrew, T. L. Triplet exciton dissociation and electron extraction in graphene-templated pentacene observed with ultrafast spectroscopy. *Phys. Chem. Chem. Phys.* **2017**, *19*, 4809−4820.
(5) Baldo, M. A.; Holmes, R. J.; Forrest, S. R. Prospects for electrically pumped organic lasers. *Phys. Rev. B: Condens. Matter Mater. Phys.* **2002**, *66*, No. 035321.
(6) Yu, Y.; Yu, Y.; Xu, C.; Barrette, A.; Gundogdu, K.; Cao, L. Fundamental limits of exciton-exciton annihilation for light emission in transition metal dichalcogenide monolayers. *Phys. Rev. B: Condens. Matter Mater. Phys.* **2016**, *93*, 201111.
(7) Muller, M. G.; Lambrev, P.; Reus, M.; Wientjes, E.; Croce, R.; Holzwarth, A. R. Singlet energy dissipation in the photosystem II light-harvesting complex does not involve energy transfer to carotenoids. *ChemPhysChem* **2010**, *11*, 1289−1296.
(8) Valkunas, L.; van Stokkum, I. H. M.; Berera, R.; van Grondelle, R. Exciton migration and uorescence quenching in LHCII aggregates: Target analysis using a simple nonlinear annihilation scheme. *Chem. Phys.* **2009**, *357*, 17−20.
(9) Trinkunas, G.; Herek, J. L.; Polivka, T.; Sundstrom, V.; Pullerits, T. Exciton delocalization probed by excitation annihilation in the light-harvesting antenna LH2. *Phys. Rev. Lett.* **2001**, *86*, 4167−4170.
(10) Valkunas, L.; Trinkunas, G.; Liuolia, V.; van Grondelle, R. Nonlinear annihilation of excitations in photosynthetic systems. *Biophys. J.* **1995**, *69*, 1117−1129.
(11) Linardy, E.; Yadav, D.; Vella, D.; Verzhbitskiy, I. A.; Watanabe, K.; Taniguchi, T.; Pauly, F.; Trushin, M.; Eda, G. Harnessing Exciton-Exciton Annihilation in Two-Dimensional Semi-conductors. *Nano Lett.* **2020**, *20*, 1647−1653.
(12) Fennel, F.; Lochbrunner, S. Exciton-exciton annihilation in a disordered molecular system by direct and multistep Förster transfer. *Phys. Rev. B: Condens. Matter Mater. Phys.* **2015**, *92*, 140301.
(13) Nguyen, T.-Q.; Martini, I. B.; Liu, J.; Schwartz, B. J. Controlling Interchain Interactions in Conjugated Polymers: The Effects of Chain Morphology on Exciton-Exciton Annihilation and Aggregation in MEH-PPV Films. *J. Phys. Chem. B* **2000**, *104*, 237−255.
(14) Bruggemann, B.; May, V. Exciton exciton annihilation dynamics in chromophore complexes. II. Intensity dependent transient absorption of the LH2 antenna system. *J. Chem. Phys.* **2004**, *120*, 2325−36.
(15) Valkunas, L.; Ma, Y.-Z.; Fleming, G. R. Exciton-exciton annihilation in single-walled carbon nanotubes. *Phys. Rev. B: Condens. Matter Mater. Phys.* **2006**, *73*, 115432.
(16) Brüggemann, B.; Pullerits, T. Nonperturbative modeling of fifth-order coherent multidimensional spectroscopy in light harvesting antennas. *New J. Phys.* **2011**, *13*, No. 025024.
(17) Dostál, J.; Fennel, F.; Koch, F.; Herbst, S.; Wurthner, F.; Brixner, T. Direct observation of exciton-exciton interactions. *Nat. Commun.* **2018**, *9*, 2466.
(18) Malý, P.; Lüttig, J.; Turkin, A.; Dostál, J.; Lambert, C.; Brixner, T. From wavelike to sub-diffusive motion: exciton dynamics and interaction in squaraine copolymers of varying length. *Chem. Sci.* **2020**, *11*, 456−466.
(19) Heshmatpour, C.; Hauer, J.; Šanda, F. Interplay of exciton annihilation and transport in fifth order electronic spectroscopy. *Chem. Phys.* **2020**, *528*, 110433.
(20) Milota, F.; Lincoln, C. N.; Hauer, J. Precise phasing of 2D-electronic spectra in a fully non-collinear phase-matching geometry. *Opt. Express* **2013**, *21*, 15904−15911.
(21) Picchiotti, A.; Prokhorenko, V. I.; Miller, R. J. A closed-loop pump-driven wire-guided ow jet for ultrafast spectroscopy of liquid samples. *Rev. Sci. Instrum.* **2015**, *86*, No. 093105.
(22) Ceymann, H.; Rosspeintner, A.; Schreck, M. H.; Mutzel, C.; Stoy, A.; Vauthey, E.; Lambert, C. Cooperative enhancement versus additivity of two-photon-absorption cross sections in linear and branched squaraine super-chromophores. *Phys. Chem. Chem. Phys.* **2016**, *18*, 16404−16413.
(23) Frenkel, J. On the Transformation of Light into Heat in Solids. II. *Phys. Rev.* **1931**, *37*, 1276−1294.
(24) Redfield, A. G. On the theory of relaxation processes. *IBM J. Res. Dev.* **1957**, *1*, 19−31.
(25) Kubo, R. Statistical-Mechanical Theory of Irreversible Processes. I. General Theory and Simple Applications to Magnetic and Conduction Problems. *J. Phys. Soc. Jpn.* **1957**, *12*, 570−586.
(26) Andrews, D. L.; Thirunamachandran, T. On three-dimensional rotational averages. *J. Chem. Phys.* **1977**, *67*, 5026−5033.
(27) Mukamel, S. *Principles of Nonlinear Optical Spectroscopy*; OUP, 1995.
(28) Seibt, J.; Dehm, V.; Wurthner, F.; Engel, V. Absorption spectroscopy of molecular trimers. *J. Chem. Phys.* **2007**, *126*, 164308.
(29) Adamo, C.; Barone, V. Toward reliable density functional methods without adjustable parameters: The PBE0 model. *J. Chem. Phys.* **1999**, *110*, 6158−6170.
(30) Weigend, F.; Ahlrichs, R. Balanced basis sets of split valence, triple zeta valence and quadruple zeta valence quality for H to Rn: Design and assessment of accuracy. *Phys. Chem. Chem. Phys.* **2005**, *7*, 3297−3305.
(31) Casida, M. E.; Jamorski, C.; Casida, K. C.; Salahub, D. R. Molecular excitation energies to high-lying bound states from time-dependent density-functional response theory: Characterization and correction of the time-dependent local density approximation ionization threshold. *J. Chem. Phys.* **1998**, *108*, 4439−4449.
(32) Yanai, T.; Tew, D. P.; Handy, N. C. A new hybrid exchange−correlation functional using the Coulomb-attenuating method (CAM-B3LYP). *Chem. Phys. Lett.* **2004**, *393*, 51−57.
(33) Iozzi, M. F.; Mennucci, B.; Tomasi, J.; Cammi, R. Excitation energy transfer (EET) between molecules in condensed matter: A novel application of the polarizable continuum model (PCM). *J. Chem. Phys.* **2004**, *120*, 7029−7040.
(34) Curutchet, C.; Mennucci, B. Quantum Chemical Studies of Light Harvesting. *Chem. Rev.* **2017**, *117*, 294−343.
(35) Frisch, M. J.; Trucks, G. W.; Schlegel, H. B.; Scuseria, G. E.; Robb, M. A.; Cheeseman, J. R.; Scalmani, G.; Barone, V.; Petersson, G. A.; Nakatsuji, H.; et al. *Gaussian 16*, Revision B.01; Gaussian Inc. Wallingford CT, 2016.
(36) van Amerongen, H.; van Grondelle, R.; Valkunas, L. *Photosynthetic Excitons*; World Scientific, 2000.
(37) Perlík, V.; Hauer, J.; Šanda, F. Finite pulse effects in single and double quantum spectroscopies. *J. Opt. Soc. Am. B* **2017**, *34*, 430.

https://dx.doi.org/10.1021/acs.jpclett.0c02141
J. Phys. Chem. Lett. 2020, 11, 7776−7781

(38) Do, T. N.; Chen, L.; Belyaev, A. K.; Tan, H.-S.; Gelin, M. F. Pulse-shape effects in fifth-order multidimensional optical spectroscopy. *Chem. Phys.* **2018**, *515*, 119−128.
(39) Malý, P.; Mančal, T. Signatures of Exciton Delocalization and Exciton-Exciton Annihilation in Fluorescence-Detected Two-Dimensional Coherent Spectroscopy. *J. Phys. Chem. Lett.* **2018**, *9*, 5654−5659.
(40) Zhong, C.; Bialas, D.; Collison, C. J.; Spano, F. C. Davydov Splitting in Squaraine Dimers. *J. Phys. Chem. C* **2019**, *123*, 18734−18745.
(41) Perlík, V.; Šanda, F. Vibrational relaxation beyond the linear damping limit in two-dimensional optical spectra of molecular aggregates. *J. Chem. Phys.* **2017**, *147*, No. 084104.

https://dx.doi.org/10.1021/acs.jpclett.0c02141
J. Phys. Chem. Lett. 2020, 11, 7776−7781

B.1. Supporting Information

Supporting information (SI) of C. Heshmatpour, P. Malevich, F. Plasser, M. Menger, C. Lambert, F. Šanda, and J. Hauer. Annihilation dynamics of molecular excitons measured at a single perturbative excitation energy. *J. Phys. Chem. Lett.*, 11(18):7776–7781, 2020. The SI is available free of charge, thus no reprint permission is necessary.

Supporting Information: Annihilation Dynamics of Molecular Excitons Measured at a Single Perturbative Excitation Energy

C. Heshmatpour,[†,‡] P. Malevich,[‡] F. Plasser,[¶] M. Menger,[§] C. Lambert,[‖] F. Šanda,[†] and J. Hauer*[,‡]

†*Institute of Physics, Faculty of Mathematics and Physics, Charles University, Ke Karlovu 5, Prague 121 16, Czech Republic*

‡*Professur für Dynamische Spektroskopien, Fakultät für Chemie, Technische Universität München, Lichtenbergstr. 4, D-85748, Garching b. München, Germany*

¶*Department of Chemistry, Loughborough University, Loughborough, LE11 3TU, United Kingdom*

§*Faculty of Science and Engineering, Zernike Institute for Advanced Materials, University of Groningen, Nijenborgh 4, 9747AG Groningen, The Netherlands*

‖*Institut für Organische Chemie, Center for Nanosystems Chemistry,Universität Würzburg, Am Hubland, 97074 Würzburg, Germany*

E-mail: juergen.hauer@tum.de

Contents

1 Experimental setup

The experimental setup represents an R^5-2D extension to our previously published R^3-2D setup.[1] For a technical drawing and a detailed discussion of the third order setup we refer to reference 1. A simplified schematic of the experimental setup is shown in Fig. S1. The pulse is split by a 50:50 beamsplitter and the delay t_2 between the transmitted and reflected pulse is set by a computer controlled linear motorized translation stage. Both replicas are then focused by separate spherical mirrors (radius of curvature ROC = 750 mm) onto diffractive optical elements (DOE). The diffracted beams are collimated by spherical mirrors (ROC = 600 mm). Two wedge pairs WP_1 and WP_2 are used to control the delay t_1 between pulses along k_1 and k_2. Both wedge pairs are made of fused silica cut at a 2 degree apex angle, with one of the wedges in each pair being stationary and another mounted on a linear motorised stage. To balance the introduced dispersion another wedge pair (WP_3) is placed into the k_3

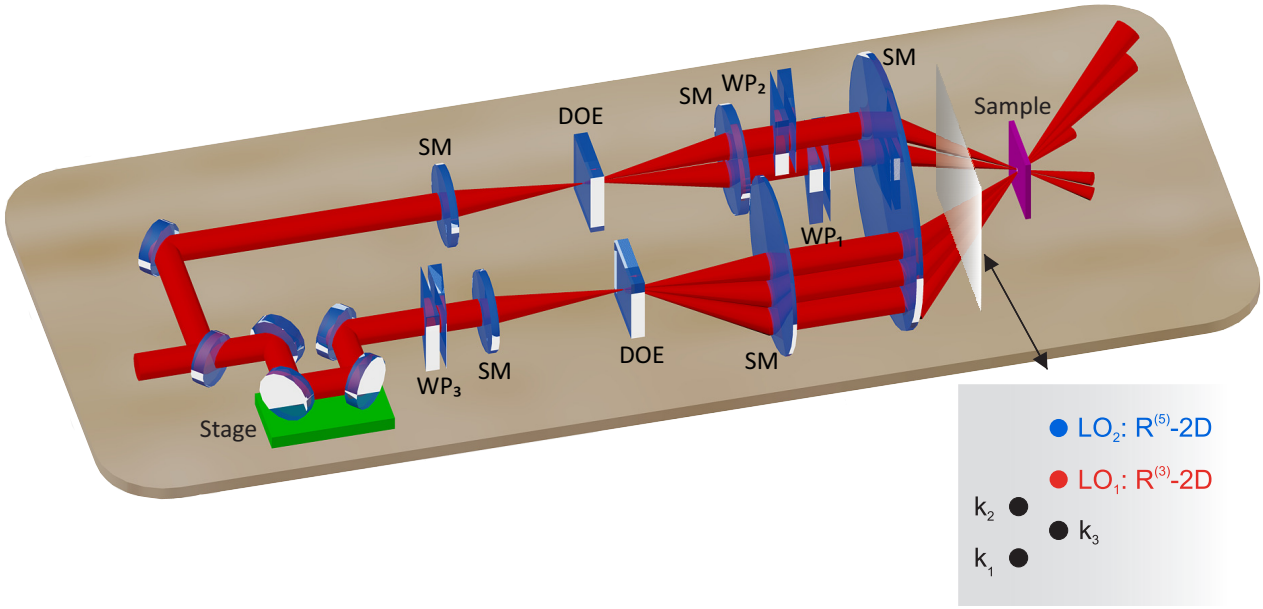

Figure S1: Schematic of the optical setup used to measure all non-linear signals of tSQA. A detailed description is presented in the text. SM: spherical mirror, DOE:diffraction optical element,WP: wedge pair, LO: Local oscillator

and local oscillator beam path. All beams are focused onto the sample position by a spherical mirror (ROC = 750 mm). The liquid sample was circulated by means of a pump driven wire guided liquid jet[2] allowing cuvette-free measurements, while keeping the thickness of the sample in the order of 150-200 μm. The pump speed was set to give a peak OD of 0.1 within the jet. The beams were collimated after the sample by separate mirrors (ROC = 600 mm) and directed to a dual-detector prism-based spectrometer (Entwicklungsbüro Stresing GmbH). The spectrometer can acquire spectra on a 50 kHz shot-to-shot basis enabling us to measure 2D maps in the sweeping regime, meaning that for a certain t_2 delay we fixed either WP_1 or WP_2 to time zero and moved the non-fixed wedge pair at a constant speed while acquiring spectra with the spectrometer. With this approach we could sample the coherence time t_1 with steps of 1.1 as, while still retaining fast data acquisition. A single 2D map was measured within 4s, without repetitions for statistical averaging. The population time t_2 was varied from -100 fs to 10 ps measuring 105 data points in total. We used a 10 fs step size from -100 fs to -20 fs. From -20 to 20 fs we sampled in steps of 1 fs. Between 20 fs and

100 fs we used a step size of 5 fs and from 100 fs up to 1 ps we went in logarithmic steps and collected 20 points per order of magnitude. The whole 3D dataset was measured within 40 minutes. In order to suppress unwanted low-frequency contributions, we recorded all 2D-spectra at a sufficiently large signal-LO-delay of 180 fs, introduced by a 150 μm microscope cover glass in the LO beam path. We phased the measured R^3- and R^5-2D maps to pump-probe and to pump-dump-probe, respectively. The microscope cover glass was removed for pump-probe and pump-dump-probe experiments.

2 Model for optical dynamics of tSQA

Simulations of the experimental signals are based on our developed abstract model of reference 3. Here, we summarize in short the adapted working equations for the squaraine trimer tSQA.

2.1 Exciton Hamiltonian - Level structure

Each tSQA aggregate is modelled as a chain of three two level chromophores associated with creation (annihilation) operator $\hat{B}_n^\dagger$ ($\hat{B}_n$) of an exciton at site n, obeying the Pauli commutation rule

$$\left[\hat{B}_n, \hat{B}_m^\dagger\right] = \delta_{nm}(1 - 2\hat{B}_m^\dagger \hat{B}_n). \tag{S1}$$

The energy level structure is given by Frenkel exciton Hamiltonian[4]

$$\hat{H}_M = E\sum_{n=1}^{3} \hat{B}_n^\dagger \hat{B}_n + \sum_{\{n,m\}=1;n\neq m}^{3} J_{mn}\hat{B}_m^\dagger \hat{B}_n. \tag{S2}$$

Here, E is the site energy and J_{mn} is the resonance coupling between chromophore m and n. Couplings J_{mn} are calculated by quantum chemistry methods described in the main text. To obtain the level splitting observed in the absorption spectrum we scaled the couplings by 16%, but kept their relative proportion.

Eq. (S2) can be partitioned in blocks (manifolds) of many body ground state ($|g\rangle$)

$$H_0 = 0, \tag{S3}$$

of single exciton states ($\{|n\rangle \equiv \hat{B}_n^\dagger |g\rangle\} = \{|1\rangle, |2\rangle, |3\rangle\}$)

$$H_1 = \begin{bmatrix} E & J_{12} & J_{13} \\ J_{21} & E & J_{23} \\ J_{31} & J_{32} & E \end{bmatrix}, \tag{S4}$$

double exciton states ($\{|nm\rangle \equiv \hat{B}_n^\dagger \hat{B}_m^\dagger |g\rangle\} = \{|12\rangle, |13\rangle, |23\rangle\}$)

$$H_2 = \begin{bmatrix} 2E & J_{23} & J_{13} \\ J_{23} & 2E & J_{12} \\ J_{13} & J_{21} & 2E \end{bmatrix} \tag{S5}$$

and tri-exciton state ($|f\rangle \equiv \hat{B}_1^\dagger \hat{B}_2^\dagger \hat{B}_3^\dagger |g\rangle$)

$$H_3 = 3E. \tag{S6}$$

Delocalized single and bi-exciton eigenstates are obtained by numerical diagonalization of the above Hamiltonians (S4) and (S5). The complete set of excitonic eigenstates $|\epsilon_i\rangle$ consists of subsets containing ground ($|g\rangle$), single- ($\{|a_i\rangle\}$), bi- ($\{|\alpha_i\rangle\}$) and tri-exciton ($|f\rangle$) eigenstates, *i.e.* $|\epsilon_i\rangle \in \{|g\rangle, |a_1\rangle\ |a_2\rangle, |a_3\rangle, |\alpha_1\rangle, |\alpha_2\rangle, |\alpha_3\rangle, |f\rangle\}$.

2.2 Quantum master equation for energy transfer and annihilation

Optical dynamics between delocalized eigenstates $|\epsilon_i\rangle$ of tSQA are described by the master equation for the excitonic density matrix

$$\frac{\partial}{\partial t}|\rho(t)\rangle\rangle = \left(\breve{\mathcal{L}} + \breve{\mathcal{D}} + \breve{\mathcal{A}}\right)|\rho(t)\rangle\rangle\,. \tag{S7}$$

It accounts for coherent evolution

$$\breve{\mathcal{L}}\,|\rho(t)\rangle\rangle = -\frac{i}{\hbar}\Big[\hat{H}_M, \hat{\rho}(t)\Big], \tag{S8}$$

for transport dynamics $\breve{\mathcal{D}}$ and exciton-exciton annihilation (EEA) $\breve{\mathcal{A}}$.

Transport dynamics are of secular Redfield type[5] and read

$$\breve{\mathcal{D}}\,|\rho(t)\rangle\rangle = \sum_{i,j=1;i\neq j}^{8}\left[k_{\epsilon_i\to\epsilon_j}\left(|\epsilon_j\rangle\langle\epsilon_i|\,\hat{\rho}(t)\,|\epsilon_i\rangle\langle\epsilon_j| - \frac{1}{2}\{|\epsilon_i\rangle\langle\epsilon_i|\,,\hat{\rho}(t)\}\right) - \gamma^{pd}_{\epsilon_i\epsilon_j}\,|\epsilon_i\rangle\langle\epsilon_i|\,\hat{\rho}(t)\,|\epsilon_j\rangle\langle\epsilon_j|\right], \tag{S9}$$

with $\{\hat{A},\hat{B}\} \equiv \hat{A}\hat{B} + \hat{B}\hat{A}$. Transport rates $k_{\epsilon_i\to\epsilon_j}$ from excitonic state $|\epsilon_i\rangle$ to $|\epsilon_j\rangle$ are given by

$$k_{\epsilon_i\to\epsilon_j} = C(\omega_{\epsilon_i\epsilon_j})\sum_{n=1}^{3}\left|\langle\epsilon_i|\,\hat{B}_n^\dagger\hat{B}_n\,|\epsilon_j\rangle\right|^2, \tag{S10}$$

where $\omega_{\epsilon_i\epsilon_j}$ is the electronic energy gap between eigenstates $|\epsilon_i\rangle$ and $|\epsilon_j\rangle$. The spectral density

$$C(\omega) = \left[1 + \coth\left(\frac{\hbar\omega}{k_B T}\right)\right]\left[2\lambda\frac{\omega\Lambda}{\omega^2+\Lambda^2} + 2\sqrt{2}\lambda_{vib}\frac{\omega\omega_{vib}^2\gamma}{(\omega^2-\omega_{vib}^2)^2 + 2\gamma^2\omega^2}\right] \tag{S11}$$

consists of a continuum of overdamped Brownian oscillator bath modes and one intramolecular mode ω_{vib} seen as a progression in the monomer absorption spectrum. Here, T is the temperature, (λ_{vib}) λ is the (vibrational) reorganization energy, Λ the inverse bath correlation time, γ the damping strength ($\gamma < \omega_{vib}$).

The pure dephasing elements $\gamma^{pd}_{\epsilon_i\epsilon_j}$ are given by

$$\gamma^{pd}_{\epsilon_i\epsilon_j} = \frac{1}{2}C(\omega=0)\sum_{n=1}^{3}\left[\langle\epsilon_i|\,\hat{B}_n^\dagger\hat{B}_n\,|\epsilon_i\rangle - \langle\epsilon_j|\,B_n^\dagger B_n\,|\epsilon_j\rangle\right]^2, \tag{S12}$$

with

$$C(\omega=0) = \frac{4k_BT}{\hbar}\left[\frac{\lambda}{\Lambda} + \frac{\sqrt{2}\gamma\lambda_{vib}}{\omega_{vib}^2}\right]. \tag{S13}$$

EEA reduces the number of excitons through unidirectional transport to lower excitonic manifolds. We assume that annihilation occurs when adjacent chromophores are occupied

$$\breve{\mathcal{A}}\,|\rho(t)\rangle\rangle = k^A\sum_{i=1}^{2}\left(\left[\hat{L}_i^{(-)}\hat{\rho}\hat{L}_i^{(-)\dagger} - \frac{1}{2}\left\{\hat{L}_i^{(-)\dagger}\hat{L}_i^{(-)},\hat{\rho}(t)\right\}\right] + \left[\hat{L}_i^{(+)}\hat{\rho}\hat{L}_i^{(+)\dagger} - \frac{1}{2}\left\{\hat{L}_i^{(+)\dagger}\hat{L}_i^{(+)},\hat{\rho}(t)\right\}\right]\right), \tag{S14}$$

where k^A is the annihilation rate and operators

$$\hat{L}_i^{(-)} \equiv B_{i+1}^\dagger B_{i+1} B_i \tag{S15}$$

and

$$\hat{L}_i^{(+)} \equiv B_i^\dagger B_i B_{i+1} \tag{S16}$$

describe annihilation of an excitation at site i ($\hat{L}_i^{(-)}$) or i+1 ($\hat{L}_i^{(+)}$), if two excitations are present at adjacent sites i and $i+1$.

The parametrization of the excitonic model is given in table S1 and S2.

Table S1: **Parametrization of the Frenkel exciton model**

Quantity	**Abbreviation**	**Value**
Site energy	E	15100 cm^{-1}
Temperature	T	300 K
Reorganization energy	λ	180 cm^{-1}
Inverse bath correlation time	Λ	1/50 fs^{-1}
Vibrational reorganization energy	λ_{vib}	180 cm^{-1}
Vibrational mode	ω_{vib}	1300 cm^{-1}
Damping strength	γ	260 cm^{-1}
Annihilation rate	k_A	1/30 fs^{-1}

Table S2: **Excitonic couplings J_{mn} between chromophores m and n of each structure. Electronic couplings between the three chromophores were computed employing time-dependent density functional theory[6] using the CAM-B3LYP functional[7] along with the SVP basis set.[8] Interchromophore couplings, considering the Coulomb contribution, were computed according to the scheme of Iozzi *et al.*[9,10] implemented in Gaussian 16.[11] The quantum chemistry based evaluations underestimate the experimentally observed single exciton level splitting slightly. For the actual simulations we thus scaled the couplings by 16%, but kept their relative proportion. The scaled couplings are given in table S2.**

Structure	J_{12} (cm^{-1})	J_{13} (cm^{-1})	J_{23} (cm^{-1})
0	-693	-58	-695
1	-700	-58	-696
2	-699	-55	-697
3	-752	-20	-760
4	-754	-31	-750
5	-697	-46	-756
6	-700	-47	-758

2.3 Linear and non-linear signals of tSQA

The linear and non-linear optical response of tSQA is calculated by employing Kubo theory.[12,13] The perturbation is a classical laser field $\vec{\mathcal{E}}(t)$ as described by the matter-field interaction Hamiltonian in long wavelength limit

$$\hat{H}_{int}(t) = -\hat{\vec{\mu}} \cdot \vec{\mathcal{E}}(t) + h.c. = -\sum_{\nu=x,y,z} \hat{\mu}^{\nu} \mathcal{E}^{\nu}(t) + h.c. \tag{S17}$$

Here, $\hat{\mu}^{\nu} \equiv \sum_{n=1}^{3} d_n^{\nu} \hat{B}_n^{\dagger}$ is the total dipole moment operator and d_n^{ν} is the transition dipole moment of each squaraine.

In the impulsive limit, well applicable to experiment, the linear response is given by response function

$$R_{(1)}^{\nu_2\nu_1}(t_1) = \left(\frac{i}{\hbar}\right) \langle\langle \mu^{\nu_2} | \breve{\mathcal{G}}(t_1) \breve{\mu}^{(+),\nu_1} | gg \rangle\rangle, \tag{S18}$$

in the molecular frame. The third order response into rephasing ($\vec{k}_R^{(3)} = -\vec{k}_1 + \vec{k}_2 + \vec{k}_3$) phase

matching direction is characterized by

$$R^{\nu_4\nu_3\nu_2\nu_1}_{(3),R}(t_1,t_2,t_3) = \left(\frac{i}{\hbar}\right)^3 \langle\langle \mu^{\nu_4}| \breve{\mathcal{G}}(t_3)\breve{\mu}^{(+),\nu_3}\breve{\mathcal{G}}(t_2)\breve{\mu}^{(+),\nu_2}\breve{\mathcal{G}}(t_1)\breve{\mu}^{(-),\nu_1}\,|gg\rangle\rangle. \tag{S19}$$

For the non-rephasing ($\vec{k}^{(3)}_{NR} = \vec{k}_1 - \vec{k}_2 + \vec{k}_3$) signal one obtains

$$R^{\nu_4\nu_3\nu_2\nu_1}_{(3),NR}(t_1,t_2,t_3) = \left(\frac{i}{\hbar}\right)^3 \langle\langle \mu^{\nu_4}| \breve{\mathcal{G}}(t_3)\breve{\mu}^{(+),\nu_3}\breve{\mathcal{G}}(t_2)\breve{\mu}^{(-),\nu_2}\breve{\mathcal{G}}(t_1)\breve{\mu}^{(+),\nu_1}\,|gg\rangle\rangle. \tag{S20}$$

The fifth order signals emitted into rephasing ($\vec{k}^{(5)}_{R} = -2\vec{k}_1 + 2\vec{k}_2 + \vec{k}_3$) and non-rephasing ($\vec{k}^{(5)}_{NR} = 2\vec{k}_1 - 2\vec{k}_2 + \vec{k}_3$) phase matching directions are given by

$$R^{\nu_6\nu_5\nu_4\nu_3\nu_2\nu_1}_{(5),R}(t_1,t_2,t_3) = \left(\frac{i}{\hbar}\right)^5 \langle\langle \mu^{\nu_6}| \breve{\mathcal{G}}(t_3)\breve{\mu}^{(+),\nu_5}\breve{\mathcal{G}}(t_2)\breve{\mu}^{(+),\nu_4}\breve{\mu}^{(+),\nu_3}\breve{\mathcal{G}}(t_1)\breve{\mu}^{(-),\nu_2}\breve{\mu}^{(-),\nu_1}\,|gg\rangle\rangle \tag{S21}$$

and

$$R^{\nu_6\nu_5\nu_4\nu_3\nu_2\nu_1}_{(5),NR}(t_1,t_2,t_3) = \left(\frac{i}{\hbar}\right)^5 \langle\langle \mu^{\nu_6}| \breve{\mathcal{G}}(t_3)\breve{\mu}^{(+),\nu_5}\breve{\mathcal{G}}(t_2)\breve{\mu}^{(-),\nu_4}\breve{\mu}^{(-),\nu_3}\breve{\mathcal{G}}(t_1)\breve{\mu}^{(+),\nu_2}\breve{\mu}^{(+),\nu_1}\,|gg\rangle\rangle, \tag{S22}$$

respectively. Eqs. (S18), (S19), (S20), (S21) and (S22) are written in Liouville space[14,15] with inner product $\langle\langle A|B\rangle\rangle \equiv \mathrm{Tr}\{A^\dagger B\}$. The dipole commutator actions $\breve{\mu}^{(+),\nu} \equiv \sum_{n=1}^{3} d^\nu_n(\breve{B}^\dagger_{nl} - \breve{B}^\dagger_{nr})$ and $\breve{\mu}^{(-),\nu} \equiv \sum_{n=1}^{3} d^\nu_n(\breve{B}_{nl} - \breve{B}_{nr})$, are defined with the use of left $\breve{B}_l\,|A\rangle\rangle \equiv \hat{B}\hat{A}$ and right $\breve{B}_r\,|A\rangle\rangle \equiv \hat{A}\hat{B}$ acting superoperators. $|gg\rangle\rangle$ is the initial excitonic density matrix in the electronic ground state. Superoperator $\breve{\mathcal{G}}(t) \equiv \exp\Big(\Big(\breve{\mathcal{L}} + \breve{\mathcal{D}} + \breve{\mathcal{A}}\Big)t\Big)$ describes the temporal evolution of the excitonic density matrix and is the Green's function solution to the excitonic master equation (S7).

The orientation of the individual trimers in solution is random with isotropic distribution. We implemented a procedure to rotationally average the above tensors of rank two, four and six along reference 16, as required for experiments performed with identical linearly polarized

pulses. They read

$$\left\langle R_{(1)}(t_1)\right\rangle_{rot} = \frac{1}{3}\Big[R^{xx}_{(1)} + R^{yy}_{(1)} + R^{zz}_{(1)}\Big], \tag{S23}$$

$$\begin{aligned}\left\langle R_{(3),R/NR}(t_1,t_2,t_3)\right\rangle_{rot} = \frac{1}{15}\Big[&3R^{xxxx}_{(3)} + 3R^{yyyy}_{(3)} + 3R^{zzzz}_{(3)}\\ &+R^{xxyy}_{(3)} + R^{xxzz}_{(3)} + R^{yyxx}_{(3)} + R^{yyzz}_{(3)} + R^{zzxx}_{(3)} + R^{zzyy}_{(3)}\\ &+R^{xyxy}_{(3)} + R^{xzxz}_{(3)} + R^{yxyx}_{(3)} + R^{yzyz}_{(3)} + R^{zxzx}_{(3)} + R^{zyzy}_{(3)}\\ &+R^{xyyx}_{(3)} + R^{xzzx}_{(3)} + R^{yxxy}_{(3)} + R^{yzzy}_{(3)} + R^{zxxz}_{(3)} + R^{zyyz}_{(3)}\Big],\end{aligned} \tag{S24}$$

and

$$\begin{aligned}\left\langle R_{(5),R/NR}(t_1,t_2,t_3)\right\rangle_{rot} = \frac{1}{105}\sum_{a,b,c=x,y,z}\Big[&R^{aabbcc}_{(5)} + R^{aabcbc}_{(5)} + R^{aabccb}_{(5)} + R^{ababcc}_{(5)} + R^{abacbc}_{(5)}\\ &+R^{abaccb}_{(5)} + R^{abbacc}_{(5)} + R^{abcabc}_{(5)} + R^{abcacb}_{(5)} + R^{abbcac}_{(5)}\\ &+R^{abcbac}_{(5)} + R^{abccab}_{(5)} + R^{abbcca}_{(5)} + R^{abcbca}_{(5)} + R^{abccba}_{(5)}\Big],\end{aligned} \tag{S25}$$

omitting the explicit temporal dependencies of the tensors and the additional index for the rephasing and non-rephasing signals on the right hand side of the equation for clarity.

The absorption spectrum $A(\Omega_1)$ of tSQA is obtained as a Fourier-Laplace transform of the linear response (eq. (S23))

$$A(\Omega_1) \equiv \mathrm{Im}\Big\{\int_0^\infty dt_1 e^{i\Omega_1 t_1}\left\langle R_{(1)}(t_1)\right\rangle_{rot}\Big\}. \tag{S26}$$

The non-rephasing and rephasing signals for for $\mathrm{R}^{(3)}$- and R^5-2D are defined in the mixed time-frequency domain as

$$\begin{aligned}\tilde{R}_{(3),NR}(\Omega_1,t_2,\Omega_3) &\equiv -\mathrm{Im}\Big\{\int_0^\infty dt_1\int_0^\infty dt_3 e^{i\Omega_1 t_1}e^{i\Omega_3 t_3}\left\langle R_{(3),NR}(t_1,t_2,t_3)\right\rangle_{rot}\Big\}\\ \tilde{R}_{(5),NR}(\Omega_1,t_2,\Omega_3) &\equiv -\mathrm{Im}\Big\{\int_0^\infty dt_1\int_0^\infty dt_3 e^{i\Omega_1 t_1}e^{i\Omega_3 t_3}\left\langle R_{(5),NR}(t_1,t_2,t_3)\right\rangle_{rot}\Big\}\end{aligned} \tag{S27}$$

and

$$\begin{aligned}
\tilde{R}_{(3),R}(\Omega_1, t_2, \Omega_3) &\equiv -\mathrm{Im}\Big\{ \int_0^\infty dt_1 \int_0^\infty dt_3 e^{-i\Omega_1 t_1} e^{i\Omega_3 t_3} \left\langle R_{(3),R}(t_1, t_2, t_3) \right\rangle_{rot} \Big\} \\
\tilde{R}_{(5),R}(\Omega_1, t_2, \Omega_3) &\equiv -\mathrm{Im}\Big\{ \int_0^\infty dt_1 \int_0^\infty dt_3 e^{-i\Omega_1 t_1} e^{i\Omega_3 t_3} \left\langle R_{(5),R}(t_1, t_2, t_3) \right\rangle_{rot} \Big\}
\end{aligned} \tag{S28}$$

Purely absorptive line shapes for R^3- and R^5-2D are obtained by summing both rephasing and non-rephasing signals, *i.e.*

$$\begin{aligned}
\tilde{R}_{(3),2D}(\Omega_1, t_2, \Omega_3) &\equiv \tilde{R}_{(3),R}(\Omega_1, t_2, \Omega_3) + \tilde{R}_{(3),NR}(\Omega_1, t_2, \Omega_3) \\
\tilde{R}_{(5),2D}(\Omega_1, t_2, \Omega_3) &\equiv \tilde{R}_{(5),R}(\Omega_1, t_2, \Omega_3) + \tilde{R}_{(5),NR}(\Omega_1, t_2, \Omega_3)
\end{aligned} \tag{S29}$$

3 Double-sided Feynman diagrams

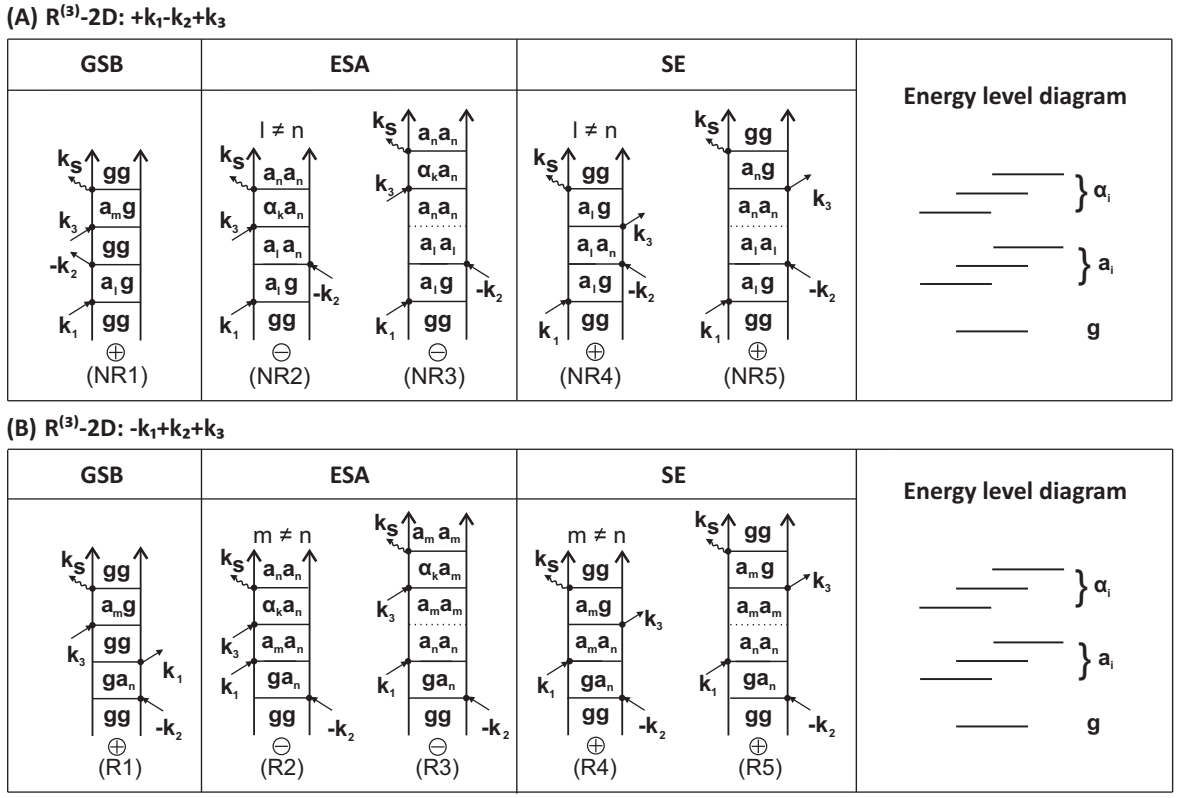

Figure S2: Double-sided Feynman diagrams used for the calculation of the non-rephasing (A) and rephasing (B) R^3-2D signal. The considered energy levels are depicted at the right of both panels. GSB: Ground state bleach, ESA: excited state absorption, SE: stimulated emission.

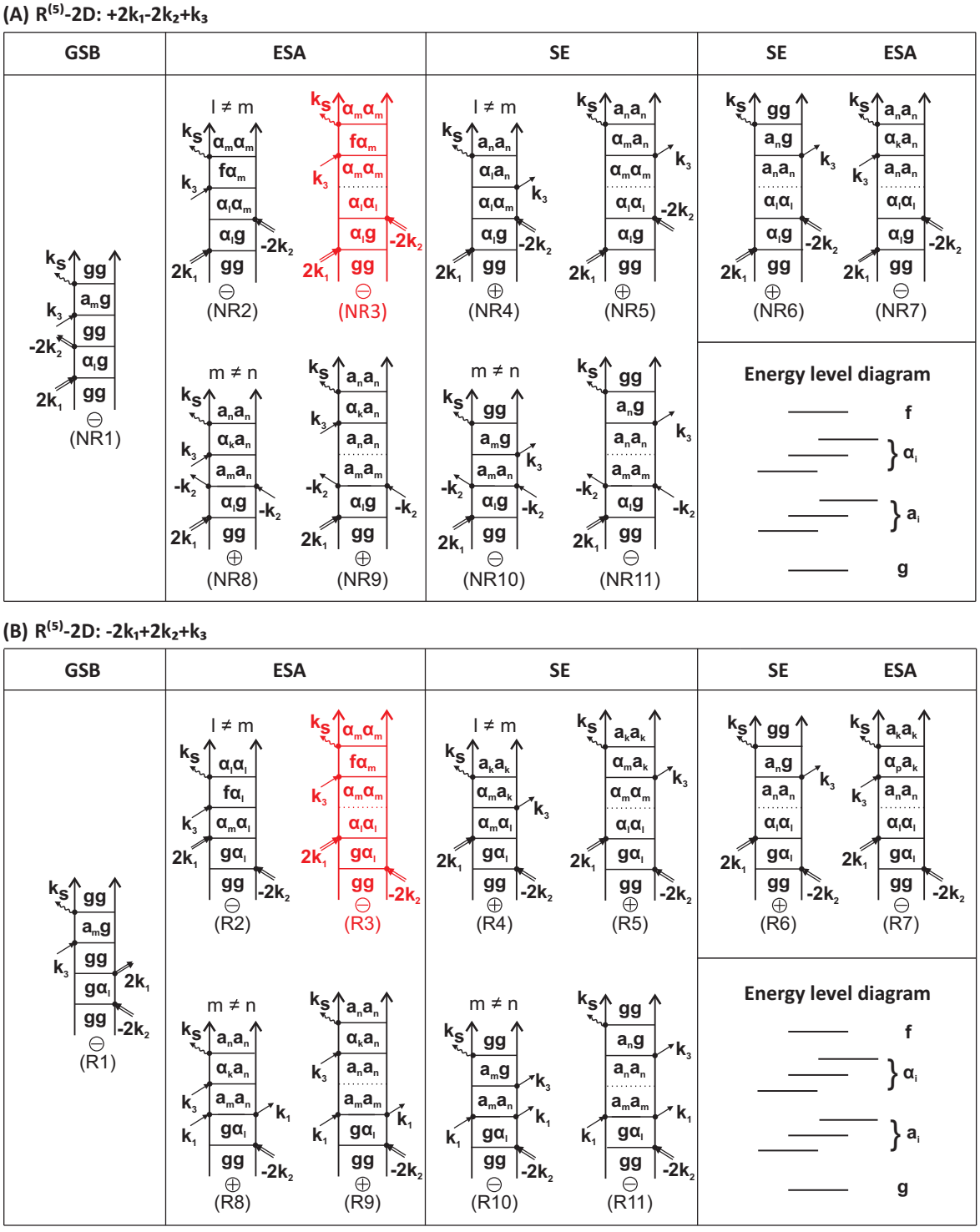

Figure S3: Double-sided Feynman diagrams used for the calculation of the non-rephasing (A) and rephasing (B) R^5-2D signal. The considered energy levels are depicted at the bottom right of both panels. Highlighted in red are the diagrams predominantly contributing to peak 2Q-ESA, essential for the extraction of the annihilation rate. GSB: Ground state bleach, ESA: excited state absorption, SE: stimulated emission.

4 tSQA structures

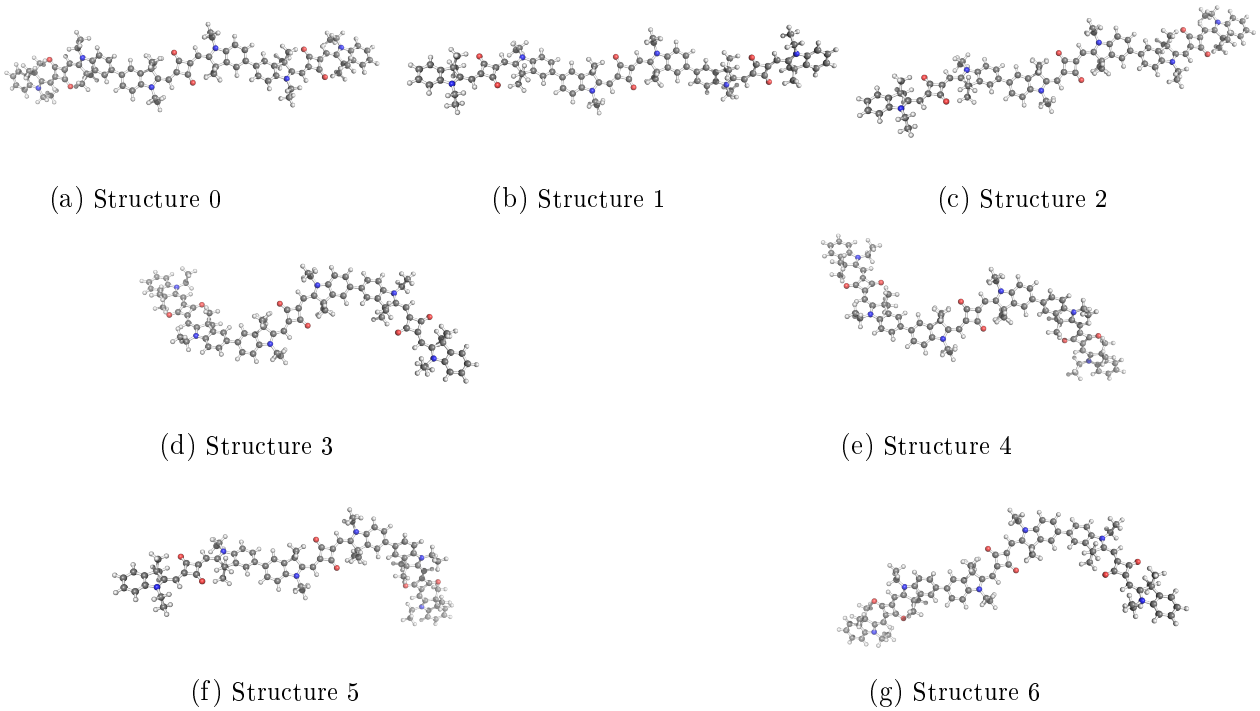

(a) Structure 0 (b) Structure 1 (c) Structure 2

(d) Structure 3 (e) Structure 4

(f) Structure 5 (g) Structure 6

Figure S4: (a)-(g) depict suggested tSQA conformer employing PBE0/SVP level of theory. Fitting the experimental data (absorption, $R^{(3)}$-2D, $R^{(5)}$-2D) of tSQA we find that the complete linear and non-linear dataset can be explained by an equal weight linear combination of signals calculated using structures 5 and 6.

5 R3-2D signal of tSQA

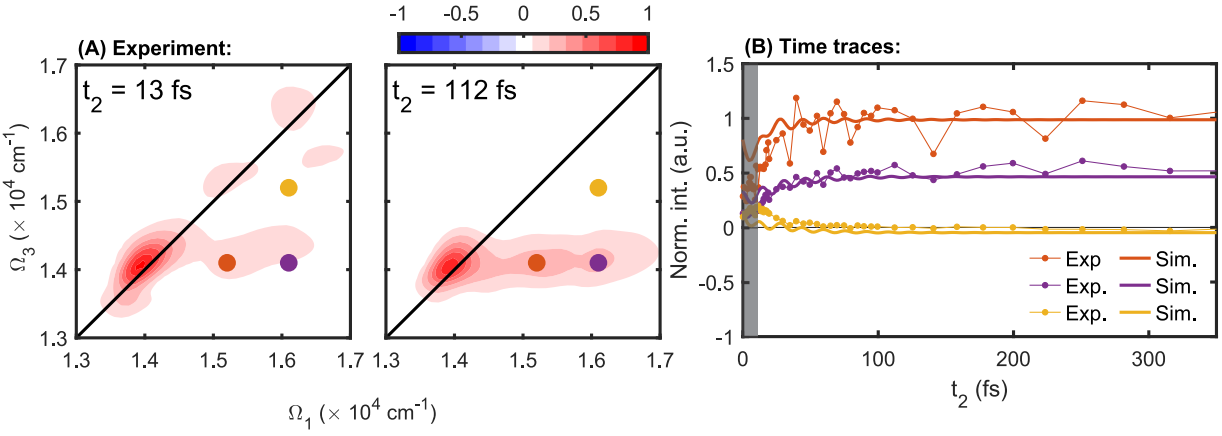

Figure S5: (A) Experimental R^3-2D spectra of tSQA for two different waiting times. The spectra show that there is ultrafast transfer between all three single exciton states of the trimer and that they share a common ground state. (B) Detailed temporal evolution of the intensity of peaks marked with their respective colour in (A). The shaded area marks the pulse overlap region. The simulations (solid lines) of the time traces, employing the Frenkel exciton model of the main text, capture the experimentally observed transport dynamics (connected dotted lines) with good agreement.

References

(1) Milota, F.; Lincoln, C. N.; Hauer, J. Precise phasing of 2D-electronic spectra in a fully non-collinear phase-matching geometry. *Opt. Express* **2013**, *21*, 15904–15911.

(2) Picchiotti, A.; Prokhorenko, V. I.; Miller, R. J. A closed-loop pump-driven wire-guided flow jet for ultrafast spectroscopy of liquid samples. *Rev Sci Instrum* **2015**, *86*, 093105.

(3) Heshmatpour, C.; Hauer, J.; Šanda, F. Interplay of exciton annihilation and transport in fifth order electronic spectroscopy. *Chem. Phys.* **2020**, *528*, 110433.

(4) Frenkel, J. On the Transformation of Light into Heat in Solids. II. *Phys. Rev.* **1931**, *37*, 1276–1294.

(5) Redfield, A. G. On the theory of relaxation processes. *IBM J. Res. Dev.* **1957**, *1*, 19 – 31.

(6) Casida, M. E.; Jamorski, C.; Casida, K. C.; Salahub, D. R. Molecular excitation energies to high-lying bound states from time-dependent density-functional response theory: Characterization and correction of the time-dependent local density approximation ionization threshold. *J. Chem. Phys.* **1998**, *108*, 4439–4449.

(7) Yanai, T.; Tew, D. P.; Handy, N. C. A new hybrid exchange–correlation functional using the Coulomb-attenuating method (CAM-B3LYP). *Chem. Phys. Lett.* **2004**, *393*, 51–57.

(8) Weigend, F.; Ahlrichs, R. Balanced basis sets of split valence, triple zeta valence and quadruple zeta valence quality for H to Rn: Design and assessment of accuracy. *Phys. Chem. Chem. Phys.* **2005**, *7*, 3297–3305.

(9) Iozzi, M. F.; Mennucci, B.; Tomasi, J.; Cammi, R. Excitation energy transfer (EET) between molecules in condensed matter: A novel application of the polarizable continuum model (PCM). *J. Chem. Phys.* **2004**, *120*, 7029–7040.

(10) Curutchet, C.; Mennucci, B. Quantum Chemical Studies of Light Harvesting. *Chem. Rev.* **2017**, *117*, 294–343.

(11) Frisch, M. J.; Trucks, G. W.; Schlegel, H. B.; Scuseria, G. E.; Robb, M. A.; Cheeseman, J. R.; Scalmani, G.; Barone, V.; Petersson, G. A.; Nakatsuji, H. et al. Gaussian 16 Revision B.01. 2016; Gaussian Inc. Wallingford CT.

(12) Kubo, R. Statistical-Mechanical Theory of Irreversible Processes. I. General Theory and Simple Applications to Magnetic and Conduction Problems. *J. Phys. Soc. Jpn.* **1957**, *12*, 570 – 586.

(13) S.Mukamel, *Principles of Nonlinear Optical Spectroscopy*; OUP, 1995.

(14) Fano, U. Description of States in Quantum Mechanics by Density Matrix and Operator Techniques. *Rev. Mod. Phys* **1957**, *29*, 570 – 586.

(15) Zwanzig, R. W. Statistical mechanics of irreversibility. *Lectures in Theoretical Physics (Boulder)* **1960**, *3*, 106 – 141.

(16) Andrews, D. L.; Thirunamachandran, T. On three-dimensional rotational averages. *J. Chem. Phys.* **1977**, *67*, 5026–5033.

C. Full Length Article of Section 3.3

Reproduced from C. Heshmatpour, J. Hauer, and F. Šanda. Correlated spectral fluctuations quantified by line shape analysis of fifth-order two-dimensional electronic spectra. *J. Chem. Phys.*, 156(8):084114, 2022, with the permission of AIP Publishing.

The Journal of Chemical Physics

Correlated spectral fluctuations quantified by line shape analysis of fifth-order two-dimensional electronic spectra

Cite as: J. Chem. Phys. **156**, 084114 (2022); https://doi.org/10.1063/5.0081053
Submitted: 06 December 2021 • Accepted: 01 February 2022 • Accepted Manuscript Online: 02 February 2022 • Published Online: 24 February 2022

Constantin Heshmatpour, Jürgen Hauer and František Šanda

The Journal of Chemical Physics ARTICLE scitation.org/journal/jcp

Correlated spectral fluctuations quantified by line shape analysis of fifth-order two-dimensional electronic spectra

Cite as: J. Chem. Phys. 156, 084114 (2022); doi: 10.1063/5.0081053
Submitted: 6 December 2021 • Accepted: 1 February 2022 •
Published Online: 24 February 2022

Constantin Heshmatpour,[1,2] Jürgen Hauer,[2] and František Šanda[1,a)]

AFFILIATIONS

[1] Institute of Physics, Faculty of Mathematics and Physics, Charles University, Ke Karlovu 5, Prague 121 16, Czech Republic
[2] Professur für Dynamische Spektroskopien, Fakultät für Chemie, Technische Universität München, Lichtenbergstr. 4, D-85748 Garching b. München, Germany

Note: This paper is part of the JCP Special Topic on Photosynthetic Light-Harvesting and Energy Conversion.
[a)] **Author to whom correspondence should be addressed:** sanda@karlov.mff.cuni.cz

ABSTRACT

Correlated spectral fluctuations were suggested to coordinate excitation transport inside natural light harvesting complexes. We demonstrate the capacities of 2D line shapes from fifth-order coherent electronic signals (R^5-2D) to report on such fluctuations in molecular aggregates and present a stochastic approach to fluctuations in correlated site and bi-exciton binding energies in the optical dynamics of Frenkel excitons. The model is applied to R^5-2D line shapes of a homodimer, and we show that the peak tilt dynamics are a measure for site energy disorder, inter-site correlation, and the strength of bi-exciton binding energy fluctuations.

I. INTRODUCTION

The remarkably high energy transfer efficiencies found in photosynthesis rests on pigment–protein complexes. In light harvesting antennas, the protein arranges strongly absorbing chromophores in close proximity with inter-pigment distances on the order of 10 Å. Upon photoexcitation, their specific steric arrangement leads to the formation of delocalized excitons. Their dynamics determine the observed high energy transfer efficiencies beyond standard transport theories.[1] The intricate role played by the pigment–protein interactions is at the heart of a long-lasting scientific debate. The theoretical approaches to this fascinating problem have been reviewed elsewhere[2] and can be categorized into theories focusing on the role of high-frequency underdamped vibrations facilitating transport via vibronic resonances[3,4] and theories emphasizing the role of the protein in coordinating low-frequency vibrational modulations of pigments. Such correlations between site frequencies[5] were suggested to prolong the excitonic coherence lifetime, and the effect of such protected coherent states on transfer efficiency is a topic of the current debate.[6] The experimental evidence for such correlated fluctuations is mainly derived from two-dimensional electronic spectroscopy or R^3-2D and relies heavily on the analysis of relatively weak beating features.[7] In this work, we show that fifth order or R^5-2D spectroscopy gives more direct access to site correlation effects in excitonic systems as well as spectral fluctuations of bi-exciton binding energies. The inclusion of the latter has been shown to be instrumental to obtain an agreement between simulated and measured non-linear line shapes of photosynthetic reaction centers at low temperatures.[8]

In general terms, R^5-2D electronic spectroscopy is a three pulse experiment measured along $\vec{K}_{R,NR} = \mp 2\vec{K}_1 \pm 2\vec{K}_2 + \vec{K}_3$ phase matching directions. Such signals were shown to specifically address the relaxation pathways of bi-excitons,[9,10] with emphasis on exciton–exciton annihilation[11] (EEA); this process is not directly accessible in experiments of lower orders. The alluring feature of R^5-2D is that—in homoaggregates with aligned transition dipoles—all inter-band transport contributions cancel by integrating the R^5-2D signal over excitation frequency Ω_1 and emission frequency Ω_3 for every waiting time t_2.[12] The integrated signal of aligned homoaggregates, thus, allows us to exclusively track and pinpoint annihilation dynamics. For non-aligned structures, annihilation and transport contributions are intertwined in

the integrated signal,[12] but the anisotropy in the integrated signal reports on the geometry of the aggregate.[13] However, annihilation dynamics in non-aligned aggregates can still be obtained from the R^5-2D signal by following the temporal evolution of specific peaks.[14]

First, R^5-2D experiments studied the diffusion limited annihilation processes in various large molecular J-aggregates to extract the picosecond exciton diffusion timescale controlling the rate of annihilation.[10,15] We have in contrast recently directly measured the ultrafast annihilation timescale of 30 fs inside a squaraine trimer.[14] The annihilation rate was extracted by following the peak volume dynamics of a single peak employing a Markovian master equation model.[12] We omitted a detailed line shape analysis as the employed model provides purely homogeneous line shapes despite the fact that the data showed interesting features such as a clearly recognizable nodal line tilt and signs of dynamic disorder, i.e., line shape dynamics. Such processes represent slow fluctuations of transition energies as studied extensively in 2D infrared spectroscopy (2D-IR)[16,17] and third order 2D electronic spectroscopy (R^3-2D). The said line shape changes—quantified by the center line (CL) slope, eccentricity, or nodal line of 2D line shapes—have been instrumental to evaluate environmental characteristics such as the system's frequency correlation function.[18]

In the present paper, we develop an accessible theoretical approach to address signatures of dynamic disorder in R^5-2D line shapes of small molecular aggregates and extend the developed master equation of Ref. 12—limited to fast environmental fluctuations—by slow spectral fluctuations responsible for line shape dynamics.[19] The latter are approximated by a classical stochastic Gaussian modulation[20,21] of site and bi-exciton binding energies. The developed model is employed to analyze R^5-2D line shape dynamics of molecular homodimers with H-type coupling (H-homodimer). We find that the inclusion of dynamic disorder introduces a tilt in the line shapes at $t_2 = 0$ fs, which we demonstrate to encode the sign and amount of correlations between on-site energies and additionally the fluctuation magnitude of the bi-exciton binding energy. We quantify and analyze the temporal evolution of the tilted line shapes by the means of center lines, introduced to extract frequency correlations from R^3-2D and 2D-IR spectra.[17,18]

II. MODEL

We consider a molecular aggregate consisting of N coupled two level molecules. The electronic level structure and transport dynamics within this system is described by the Frenkel exciton Hamiltonian[22]

$$\hat{H}(t) = \sum_{n=1}^{N} \hat{E}_n(t)\hat{B}_n^\dagger \hat{B}_n + \sum_{\substack{n,m=1 \\ n\neq m}}^{N} J_{nm}\hat{B}_n^\dagger \hat{B}_m + \sum_{\substack{n,m=1 \\ n\neq m}}^{N} \frac{\hat{\Delta}_{nm}(t)}{2}\hat{B}_n^\dagger \hat{B}_m^\dagger \hat{B}_n \hat{B}_m. \tag{1}$$

Site energies $\hat{E}_n(t)$ and bi-exciton binding energies $\hat{\Delta}_{nm}(t)$ are subject of stochastic bath induced modulations. The excitonic coupling J_{nm} is assumed to be constant as its modulations are usually quite weak and have negligible influence on line shapes.[23] $\hat{B}_n^\dagger$ and $\hat{B}_n$ are, respectively, the operators associated with excitation and de-excitation of site n obeying the Pauli commutation relation,[24]

$$\left[\hat{B}_n, \hat{B}_m^\dagger\right] = \delta_{mn}\left(1 - 2\hat{B}_m^\dagger \hat{B}_n\right). \tag{2}$$

We further assume that the stochastic modulation of $\hat{H}(t)$ around mean values $\bar{E}_n$ ($\bar{\Delta}_{nm}$) of on-site (bi-exciton binding) energies can be decomposed into slow classical $E_n(t)$ ($\Delta_{nm}(t)$) and fast quantum $\hat{Q}_n$ ($\hat{Q}_{nm}$) components. The slow classical components are Gaussian[25] and are thus fully characterized by the correlation matrices

$$\begin{aligned}
\Sigma^{(1)}_{n,m}(t) &\equiv \left\langle \left(E_n(t) - \bar{E}_n\right)\left(E_m(0) - \bar{E}_m\right)\right\rangle, \\
\Sigma^{(2)}_{nm,kl}(t) &\equiv \left\langle \left(\Delta_{nm}(t) - \bar{\Delta}_{nm}\right)\left(\Delta_{kl}(0) - \bar{\Delta}_{kl}\right)\right\rangle, \\
\Sigma^{(2-1)}_{nm,k}(t) &\equiv \left\langle \left(\Delta_{nm}(t) - \bar{\Delta}_{nm}\right)\left(E_k(0) - \bar{E}_k\right)\right\rangle.
\end{aligned} \tag{3}$$

For simulations, it is feasible to decompose the Gaussian processes $E_n(t)$ and $\Delta_{nm}(t)$,

$$E_n(t) = \bar{E}_n + \sum_{m=1}^{N_q} D_{nm} q_m(t), \tag{4}$$

$$\Delta_{nm}(t) = \bar{\Delta}_{nm} + \sum_{k=1}^{N_q} \tilde{D}_{nm,k} q_k(t), \tag{5}$$

into linear combinations of N_q independent Ornstein–Uhlenbeck[20] (OU) processes $q_n(t)$, characterized by the exponentially decaying correlation function

$$C_n^{(q)}(t) = \langle q_n(t) q_n(0)\rangle = \sigma_n^2 e^{-t/\tau_n}, \tag{6}$$

with timescale τ_n and magnitude σ_n. Correlations among site and bi-exciton binding energies or between the two are then encoded in coefficients D_{nm} and $\tilde{D}_{nm,k}$ as inserting Eqs. (4) and (5) into Eq. (3) leads to

$$\begin{aligned}
\Sigma^{(1)}_{n,m}(t) &= \sum_{j=1}^{N_q} D_{nj} D_{mj} C_j^{(q)}(t), \\
\Sigma^{(2)}_{nm,kl}(t) &= \sum_{j=1}^{N_q} \tilde{D}_{nm,j} \tilde{D}_{kl,j} C_j^{(q)}(t), \\
\Sigma^{(2-1)}_{nm,k}(t) &= \sum_{j=1}^{N_q} \tilde{D}_{nm,j} D_{kj} C_j^{(q)}(t).
\end{aligned} \tag{7}$$

The above decomposition of the matrices Σ combines a separation of timescales τ_n with the decomposition into products of the type DD^T, which can be numerically obtained employing the Cholesky factorization algorithm.[26]

In the calculation scheme of the non-linear response functions, presented below, the two point joint probability

$$P(q_n(t), q_n(0), t) = \frac{1}{2\pi\sigma_n^2\sqrt{\left(1 - e^{-2t/\tau_n}\right)}} \times \exp\left(-\frac{q_n^2(t) + q_n^2(0) - 2q_n(t)q_n(0)e^{-\frac{t}{\tau_n}}}{2\sigma_n^2\left(1 - e^{-2t/\tau_n}\right)}\right) \tag{8}$$

of the OU process [Eq. (6)] will be of special importance.

The fast coordinates $\hat{Q}_n$ and $\hat{Q}_{nm}$ induce transport and decoherence and are considered quantum to ensure thermodynamic consistence.[27] We take advantage of the timescale separation between the slow and fast coordinates and include the effect of $\hat{Q}_n$ and $\hat{Q}_{nm}$ by a quantum master equation whose derivation is well documented in the literature[27] and shortly summarized in Appendix A. The resulting excitonic master equation

$$\frac{\partial}{\partial t}|\rho(t)\rangle\rangle = \check{\mathscr{R}}(\{q(t)\})|\rho(t)\rangle\rangle \tag{9}$$

with relaxation tensor

$$\check{\mathscr{R}}(\{q(t)\}) = \check{\mathscr{L}}(\{q(t)\}) + \check{\mathscr{D}}(\{q(t)\}) + \check{\mathscr{A}} \tag{10}$$

depends on the collection of slow coordinates $\{q(t)\} = (q_1(t), q_2(t), \ldots, q_n(t))$ and consists out of three parts: Liouvillian of the free evolution

$$\check{\mathscr{L}}(\{q(t)\})|\rho(t)\rangle\rangle = -i[H(t), \hat{\rho}(t)] \tag{11}$$

generated by the slow (classical) part of Hamiltonian (1), i.e., by substituting solely Eqs. (4) and (5) for site $\hat{E}$ and bi-exciton binding energies $\hat{\Delta}$ into Eq. (1). Dissipative dynamics $\check{\mathscr{D}}(\{q(t)\})$ generated by the fast component is calculated in the Redfield[28] limit and induces homogeneous line broadening and population relaxation. $\check{\mathscr{A}}$ describes EEA as unidirectional transfer between manifolds differing in one quantum of excitation with phenomenological rates k_i^A $(i = 1, \ldots, N-1)$. Our model thus omits a detailed microscopic description of EEA via an additional transient local state[29–31] and represents the minimal model retaining only the most essential structure of the manifolds and transport processes required for simulating peak shapes of R^5-2D signals. The detailed equations can be found in Appendix A.

To calculate the fifth-order response emitted into rephasing $(\vec{K}_R = -2\vec{K}_1 + 2\vec{K}_2 + \vec{K}_3)$ and non-rephasing $(\vec{K}_{NR} = 2\vec{K}_1 - 2\vec{K}_2 + \vec{K}_3)$ phase matching directions, we employ Kubo theory and the impulsive limit.[32,33] The interaction between the aggregate and the electric field $\mathscr{E}(t) = \sum_{j=1}^{3}\mathscr{E}_j\delta(t-\tau_j)$ is described semiclassically,

$$\hat{H}_{int}(t) = -\hat{\mu}\mathscr{E}(t) + c.c, \tag{12}$$

where $\hat{\mu} = \sum_{n=1}^{N} d_n \hat{B}_n^\dagger$ is the total dipole operator and d_n is the transition dipole moment of molecule n. To include the stochastic dynamics of Eqs. (3)–(11) into the model, we adapt the calculation strategy of Ref. 34: First, we calculate the non-linear response functions along non-rephasing and rephasing phase matching directions for a specific trajectory $\{\phi(t)\}$, and later, we average over all possible trajectories. We employ the Liouville space notation,[35,36] with inner product $\langle\langle A||B\rangle\rangle \equiv \mathrm{Tr}\,\hat{A}^\dagger\hat{B}$. The excitonic density matrix element before the first light–matter interaction, with the system in its ground state, reads as $|gg\rangle\rangle$. By using Green's function superoperator technique,[24] one obtains

$$\begin{aligned} S_{NR}^{(5)}(t_1,t_2,t_3;\{\phi(\tau)\}) = (i)^5\langle\langle\mu|\check{\mathscr{G}}(t_1+t_2,t_1+t_2+t_3;\{\phi(\tau)\})\check{\mu}^{(+)} \\ \times\check{\mathscr{G}}(t_1,t_1+t_2;\{\phi(\tau)\})\check{\mu}^{(-)}\check{\mu}^{(-)} \\ \times\check{\mathscr{G}}(0,t_1;\{\phi(\tau)\})\check{\mu}^{(+)}\check{\mu}^{(+)}|gg\rangle\rangle \end{aligned} \tag{13}$$

for the non-rephasing signal and

$$\begin{aligned} S_{R}^{(5)}(t_1,t_2,t_3;\{\phi(\tau)\}) = (i)^5\langle\langle\mu|\check{\mathscr{G}}(t_1+t_2,t_1+t_2+t_3;\{\phi(\tau)\})\check{\mu}^{(+)} \\ \times\check{\mathscr{G}}(t_1,t_1+t_2;\{\phi(\tau)\})\check{\mu}^{(+)}\check{\mu}^{(+)} \\ \times\check{\mathscr{G}}(0,t_1;\{\phi(\tau)\})\check{\mu}^{(-)}\check{\mu}^{(-)}|gg\rangle\rangle \end{aligned} \tag{14}$$

for the rephasing signal. The dipole superoperators $\check{\mu}^{(+)} \equiv \sum_{n=1}^{N} d_n(\check{B}_{nl}^\dagger - \check{B}_{nr}^\dagger)$ and $\check{\mu}^{(-)} \equiv \sum_{n=1}^{N} d_n(\check{B}_{nl} - \check{B}_{nr})$ are defined employing left $\check{B}_l|A\rangle\rangle \equiv \hat{B}\hat{A}$ and right $\check{B}_r|A\rangle\rangle \equiv \hat{A}\hat{B}$ multiplication superoperators. The response functions (13) and (14) and Green's function solution to the excitonic master equation (9),

$$\check{\mathscr{G}}(t_a,t_b;\{\phi(\tau)\}) = \exp_+\left\{\int_{t_a}^{t_b} d\tau\,\check{\mathscr{R}}(\{q(\tau)\})\right\}, \tag{15}$$

depend on the entire stochastic trajectories, what we emphasized by the $\{\phi(t)\}$ notation. To calculate the final response functions, we have to perform as the next step an average over the complete collection of stochastic paths. To facilitate the non-trivial averaging procedure, we again employ the slow character of coordinates $q(t)$ and assume that they are stable during the short coherence intervals t_1 and t_3. Green's function (15) then parametrically depends on the value of $q(t)$ at single time. The explicit dependence of the superoperator exponential on both the initial (t_a) and final (t_b) time then reduces to a function of the interval $t_b - t_a$. In particular, in the t_1 interval, we have

$$\check{\mathscr{G}}(0,t_1;\{\phi(\tau)\}) \approx \check{\mathscr{G}}(t_1;\{q(0)\}) = \exp\{\check{\mathscr{R}}(\{q(0)\})t_1\} \tag{16}$$

and in the t_3 interval, we have

$$\begin{aligned} \check{\mathscr{G}}(t_1+t_2,t_1+t_2+t_3;\{\phi(\tau)\}) &\approx \check{\mathscr{G}}(t_3;\{q(t_2)\}) \\ &= \exp\{\check{\mathscr{R}}(\{q(t_2)\})t_3\}. \end{aligned} \tag{17}$$

In population interval t_2, we allow for the changes in q coordinates, but the associated relaxation dynamics will only be re-parameterized in the middle of the interval.[37] Green's function thus propagates half of the t_2 interval with $\check{\mathscr{R}}$ taken at $q(0)$ and the remaining part with $q(t_2)$. These assumptions lead to the non-rephasing signal

$$\begin{aligned} S_{NR}^{(5)}(t_1,t_2,t_3;\{\phi(\tau)\}) \\ \approx (i)^5\langle\langle\mu|\check{\mathscr{G}}(t_3;\{q(t_2)\})\check{\mu}^{(+)}\check{\mathscr{G}}\left(\frac{t_2}{2};\{q(t_2)\}\right)\check{\mathscr{G}}\left(\frac{t_2}{2};\{q(0)\}\right) \\ \times\check{\mu}^{(-)}\check{\mu}^{(-)}\check{\mathscr{G}}(t_1;\{q(0)\})\check{\mu}^{(+)}\check{\mu}^{(+)}|gg\rangle\rangle \end{aligned} \tag{18}$$

and the rephasing signal

$$\begin{aligned} S_{R}^{(5)}(t_1,t_2,t_3;\{\phi(\tau)\}) \\ \approx (i)^5\langle\langle\mu|\check{\mathscr{G}}(t_3;\{q(t_2)\})\check{\mu}^{(+)}\check{\mathscr{G}}\left(\frac{t_2}{2};\{q(t_2)\}\right)\check{\mathscr{G}}\left(\frac{t_2}{2};\{q(0)\}\right) \\ \times\check{\mu}^{(+)}\check{\mu}^{(+)}\check{\mathscr{G}}(t_1;\{q(0)\})\check{\mu}^{(-)}\check{\mu}^{(-)}|gg\rangle\rangle \end{aligned} \tag{19}$$

Equations (18) and (19) now depend on q at time zero and a single t_2 value at a later time, and the final averaging $\langle\cdots\rangle$ of rephasing and non-rephasing signals of the fifth-order response over stochastic trajectories is then performed with the two time joint probabilities introduced in Eq. (8), resulting in

$$\begin{aligned} R^{(5)}_{R;NR}(t_1,t_2,t_3) &= \langle S^{(5)}_{R;NR}(t_1,t_2,t_3;\{q(\tau)\})\rangle \\ &\approx \prod_{n=1}^{N_q}\left(\int_{-\infty}^{\infty} dq_n(t_2)\int_{-\infty}^{\infty} dq_n(0)\right) \\ &\quad\times S^{(5)}_{R;NR}(t_1,t_2,t_3;\{q(t_2)\},\{q(0)\}) \\ &\quad\times \prod_{n=1}^{N_q} P(q_n(t_2),q_n(0),t_2). \end{aligned} \tag{20}$$

The purely absorptive line shapes of the R^5-2D signal

$$\tilde{R}_{2D}(\Omega_1,t_2,\Omega_3) \equiv \tilde{R}_R(\Omega_1,t_2,\Omega_3) + \tilde{R}_{NR}(\Omega_1,t_2,\Omega_3) \tag{21}$$

are obtained by adding the non-rephasing signal

$$\tilde{R}_{NR}(\Omega_1,t_2,\Omega_3) \equiv -\mathrm{Im}\left\{\int_0^{\infty} dt_1\int_0^{\infty} dt_3 e^{i\Omega_1 t_1} e^{i\Omega_3 t_3} R^{(5)}_{NR}(t_1,t_2,t_3)\right\} \tag{22}$$

and the rephasing signal

$$\tilde{R}_{R}(\Omega_1,t_2,\Omega_3) \equiv -\mathrm{Im}\left\{\int_0^{\infty} dt_1\int_0^{\infty} dt_3 e^{-i\Omega_1 t_1} e^{i\Omega_3 t_3} R^{(5)}_{R}(t_1,t_2,t_3)\right\} \tag{23}$$

transformed into the mixed time–frequency domain.

III. RESULTS AND DISCUSSION

We demonstrate the capacity of the presented calculation scheme to simulate R^5-2D line shapes of a strongly coupled molecular H-homodimer ($J > 0$) with average site energies $\tilde{E}_1 = \tilde{E}_2 \equiv \tilde{E}$ and transition dipole moments $d_1 = d_2 \equiv d$. Similarly, the slow site energy fluctuations have the same fluctuation magnitudes σ_E and decorrelation timescale τ_E,

$$\Sigma^{(1)}_{11}(t) \equiv \Sigma^{(1)}_{22}(t) \equiv \sigma_E^2 e^{-t/\tau_E}, \tag{24}$$

but may have a variable degree of correlation $\beta \in [-1,1]$ between the two on-site fluctuations, i.e.,

$$\Sigma^{(1)}_{12}(t) \equiv \Sigma^{(1)}_{21}(t) \equiv \beta\sigma_E^2 e^{-t/\tau_E}. \tag{25}$$

The fluctuations of the bi-exciton binding energy

$$\Sigma^{(2)}(t) \equiv \sigma_\Delta^2 e^{-t/\tau_\Delta} \tag{26}$$

have magnitude σ_Δ and timescale τ_Δ and are chosen to be independent of single exciton fluctuations [$\Sigma^{(2-1)}(t) \equiv 0$]. We will often compare magnitudes of single exciton and bi-exciton fluctuations by the ratio

$$\gamma \equiv \frac{\sigma_\Delta}{\sigma_E}. \tag{27}$$

The optical line shapes are best analyzed in terms of transition frequencies,

$$\begin{aligned} \omega_{a_1 g}(t) &= \frac{E_1(t)+E_2(t)}{2} - \frac{1}{2}\sqrt{(E_1(t)-E_2(t))^2+4J^2}, \\ \omega_{a_2 g}(t) &= \frac{E_1(t)+E_2(t)}{2} + \frac{1}{2}\sqrt{(E_1(t)-E_2(t))^2+4J^2}, \\ \omega_{\alpha a_1}(t) &= \omega_{a_2 g}(t) + \Delta(t), \\ \omega_{\alpha a_2}(t) &= \omega_{a_1 g}(t) + \Delta(t), \\ \omega_{\alpha g}(t) &= E_1(t) + E_2(t) + \Delta(t), \end{aligned} \tag{28}$$

between instantaneous eigenstates (see Fig. 1) consisting of the collective ground state $|g\rangle$, the bi-exciton state

$$|\alpha\rangle = \hat{B}_1^\dagger \hat{B}_2^\dagger |g\rangle \tag{29}$$

and two delocalized single exciton states

$$\begin{aligned} |a_1(t)\rangle &= -\sin(\theta)\hat{B}_1^\dagger|g\rangle + \cos(\theta)\hat{B}_2^\dagger|g\rangle, \\ |a_2(t)\rangle &= \cos(\theta)\hat{B}_1^\dagger|g\rangle + \sin(\theta)\hat{B}_2^\dagger|g\rangle, \end{aligned} \tag{30}$$

with mixing angle

$$\theta(t) = \frac{1}{2}\mathrm{arccot}\left(\frac{E_1(t)-E_2(t)}{2J}\right). \tag{31}$$

Transition dipoles between excitonic states are given by

$$\begin{aligned} \mu_{a_1 g}(t) &= \mu_{\alpha a_1}(t) = d[\cos(\theta) - \sin(\theta)], \\ \mu_{a_2 g}(t) &= \mu_{\alpha a_2}(t) = d[\cos(\theta) + \sin(\theta)]. \end{aligned} \tag{32}$$

In the following simulations, we further simplified the transport dynamics and consider the gap between the single exciton

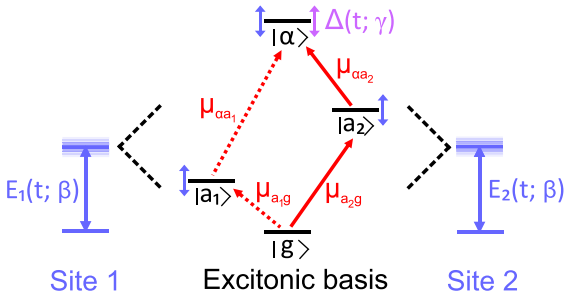

FIG. 1. Electronic energy level structure of the strongly coupled fluctuating dimer model discussed in the main text. The fluctuations inside the excitonic basis induced by site energies $E_n(t)$ and the bi-exciton binding energy $\Delta(t)$ are depicted with blue and violet arrows, respectively. The two dominant transitions of the homodimer are depicted with full red arrows, whereas transitions possible due to strong fluctuations (with respect to the coupling) are depicted with dashed arrows.

states to be much larger than the thermal energy so that the upward transport is negligible. Population dynamics are thus determined by two parameters: the rate constant k_R for population relaxation from the energetically higher lying single exciton state $|a_2\rangle$ to the lower lying single exciton state $|a_1\rangle$ and the rate k_A depleting population from bi-exciton state $|\alpha\rangle$.

In Secs. III A and III B, we compare R^5-2D line shapes of homodimers from which bi-exciton fluctuations are fully derived from on-site frequencies and have no autonomous spectral motions ($\gamma = 0$) with the case including additional autonomous bi-exciton fluctuations ($\gamma \neq 0$).

A. Non-autonomous bi-exciton fluctuations ($\gamma = 0$)

We start the discussion of the R^5-2D signals with a H-homodimer from which bi-exciton fluctuations are built up entirely from site energy fluctuations and have no independent (autonomous) component ($\gamma = 0$). The simulated R^5-2D line shapes in the slow annihilation limit ($k_A \ll k_R$) are depicted in Fig. 2 assuming uncorrelated [$\beta = 0$, (a)], correlated [$\beta = 1$, (b)], and anticorrelated [$\beta = -1$, (c)] on-site fluctuations.

We first recapitulate[12] the overall structure of the H-homodimer R^5-2D signal based on the inspection of double-sided Feynman diagrams depicted in Fig. 2(d): All diagrams evolve with coherence $|\alpha g\rangle\rangle$ during t_1 (i.e., with frequency $\omega_{\alpha g}$) corresponding to the observed peak positions at $\Omega_1 = 30\,000$ cm^{-1}. During t_3, the coherences oscillate with frequencies $\omega_{a_2 g} \approx 15\,800$ cm^{-1} [high-frequency negative peak, contributions are represented by the following pathways in Fig. 2(d): ground state bleach (GSB), single-quantum stimulated emission (1Q-SE), and EEA stimulated emission (EEA-SE)] and $\omega_{\alpha a_2} \approx 14\,200$ cm^{-1} [low-frequency positive peak, contributions are represented by the following pathways in Fig. 2(d): single-quantum excited state absorption (1Q-ESA), double-quantum stimulated emission (2Q-SE) and EEA excited state absorption (EEA-ESA)]. Their interference yields the observed two-peak structure at $t_2 = 0$ fs. The signal of the H-homodimer becomes dominated by the GSB diagram at long waiting times (panels of the second column from the left), and it reveals certain differences in the overall structure between the three panels when all transport and annihilation dynamics are finished ($k_R t_2 \gg 1$ and $k_A t_2 \gg 1$) and the lower, positive peak is damped. In the anticorrelated case, another negative low [magnified by 20% in Fig. 2(c)] frequency peak becomes apparent at $(\omega_{\alpha g}, \omega_{a_1 g})$. The feature appears due to the transient redistribution of the dipole moment strength toward the dark state[34] $|a_1\rangle$ as the fluctuations ($\sigma_E = 600$ cm^{-1}) are comparable to the excitonic coupling ($J = 800$ cm^{-1}). This effect also leads to the slightly asymmetric long time line shape of the uncorrelated case. Such a feature cannot be seen in the case of correlated fluctuations as the on-site energies are always identical, and no redistribution of the dipole moment strength is possible.

Having understood the overall peak structure, we next focus on the influence of dynamic disorder on the line shapes. To gain a deeper understanding of the relation between line shapes and disorder, we compare the line shapes [two leftmost panels of Figs. 2(a)–2(c)] with correlation statistics [two rightmost panels of Figs. 2(a)–2(c)] of the initial double (2Q) frequency $\omega_{\alpha g}(0)$ with delayed single (1Q) frequencies $\omega_{a_2 g}(t_2)$ relevant for the negative peak (blue points),

$$\tilde{P}_-(\Omega_1, t_2, \Omega_3) \equiv \langle \delta(\Omega_1 - \omega_{\alpha g}(0)) \delta(\Omega_3 - \omega_{a_2 g}(t_2)) \rangle, \tag{33}$$

and $\omega_{\alpha a_2}(t_2)$ relevant for the positive peak (orange points),

$$\tilde{P}_+(\Omega_1, t_2, \Omega_3) \equiv \langle \delta(\Omega_1 - \omega_{\alpha g}(0)) \delta(\Omega_3 - \omega_{\alpha a_2}(t_2)) \rangle, \tag{34}$$

obtained by diagonalizing 5000 sample trajectories [Eqs. (4) and (5)] of the Frenkel exciton Hamiltonian (1). Gaussian approximations to these 1Q-2Q statistics are given analytically in Appendix B for the general dimer model allowing for difference $E_\delta \equiv \tilde{E}_1 - \tilde{E}_2$ between site energies and general correlation matrix elements (3). The results of Appendix B are used in the main text in the homodimer limit: Eqs. (24) and (25) and $E_\delta = 0$ [except Eq. (39)].

The $t_2/\tau_E = 0$ R^5-2D maps of both the uncorrelated [Fig. 2(a)] and correlated [Fig. 2(b)] cases show that disorder induces elliptical and tilted line shapes. The magnitude of the tilt at zero delay time is quite similar for both peaks. After bath decorrelation at longer times ($t_2/\tau_E = 5$), the peak loses its tilt but remains elliptical.

The 1Q-2Q statistics of Figs. 2(a) and 2(b) resembles well the line shapes, differences between the two are largely ascribed to homogeneous broadening of the line shapes induced by the fast quantum coordinates. We can qualitatively understand the tilt's dynamics by calculating the principal axis of the elliptical contours [depicted in Figs. 2(a) and 2(b)] of the Gaussian approximation [see Eq. (B8) in Appendix B]. We find that the $t_2/\tau_E = 0$ line shapes and 1Q-2Q statistics are centered around lines,

$$\Omega_{3,\mp} = 0.5\Omega_1 \pm J, \tag{35}$$

as both single exciton $\omega_{a_2 g}(0) \propto \omega_{\alpha a_2}(0) \propto (E_1(0) + E_2(0))/2$ and bi-exciton $\omega_{\alpha g}(0) = E_1(0) + E_2(0)$ energies reflect the same combination of site energies. The general delay dependent angle between the principal and Ω_1 axis is given by

$$\tan(2\Phi_\pm(t_2)) = \frac{4}{3} C_E(t_2) \tag{36}$$

for both the positive (Φ_+) and negative (Φ_-) peaks with normalized correlation function

$$C_E(t) \equiv \frac{\Sigma_{11}^{(1)}(t)}{\Sigma_{11}^{(1)}(0)} = \frac{\Sigma_{22}^{(1)}(t)}{\Sigma_{22}^{(1)}(0)}. \tag{37}$$

The time dependence of the above tilts is a substantial difference to the GSB peak of R^3-2D, where $\tan(\Phi) = 1$ holds at all t_2 times.[18]

The case of anticorrelated sites ($\beta = -1$) depicted in Fig. 2(c) is vastly different compared to the above discussed cases: Both the negative and the positive peaks are not tilted and remain rather homogeneous. The reason is that the 2Q-energy $\omega_{\alpha g}(t) \equiv \omega_{\alpha g} \equiv 2\tilde{E}$ is stabilized by the anticorrelated motion of the sites for all waiting times and fluctuations of 1Q-energies are quadratic in $(E_1 - E_2)$ such that negligible inhomogeneous broadening occurs exclusively toward higher (lower) values of the mean frequencies of the negative (positive) peak along Ω_3.

Changing the type of on-site correlations affects the line shapes and the 1Q-2Q statistics (see Fig. 2). The latter is unfortunately not a direct spectroscopic observable, and the above characterization of dynamics by the principal axis (36) is limited to elliptic contours of Gaussian peaks. Next, we will thus inquire how the correlated spectral dynamics can be quantitatively extracted from the R^5-2D line shapes. To step beyond the limit of the elliptical line shapes, we adopt the concept of the center line[16–18] (CL) that quantifies the line shape

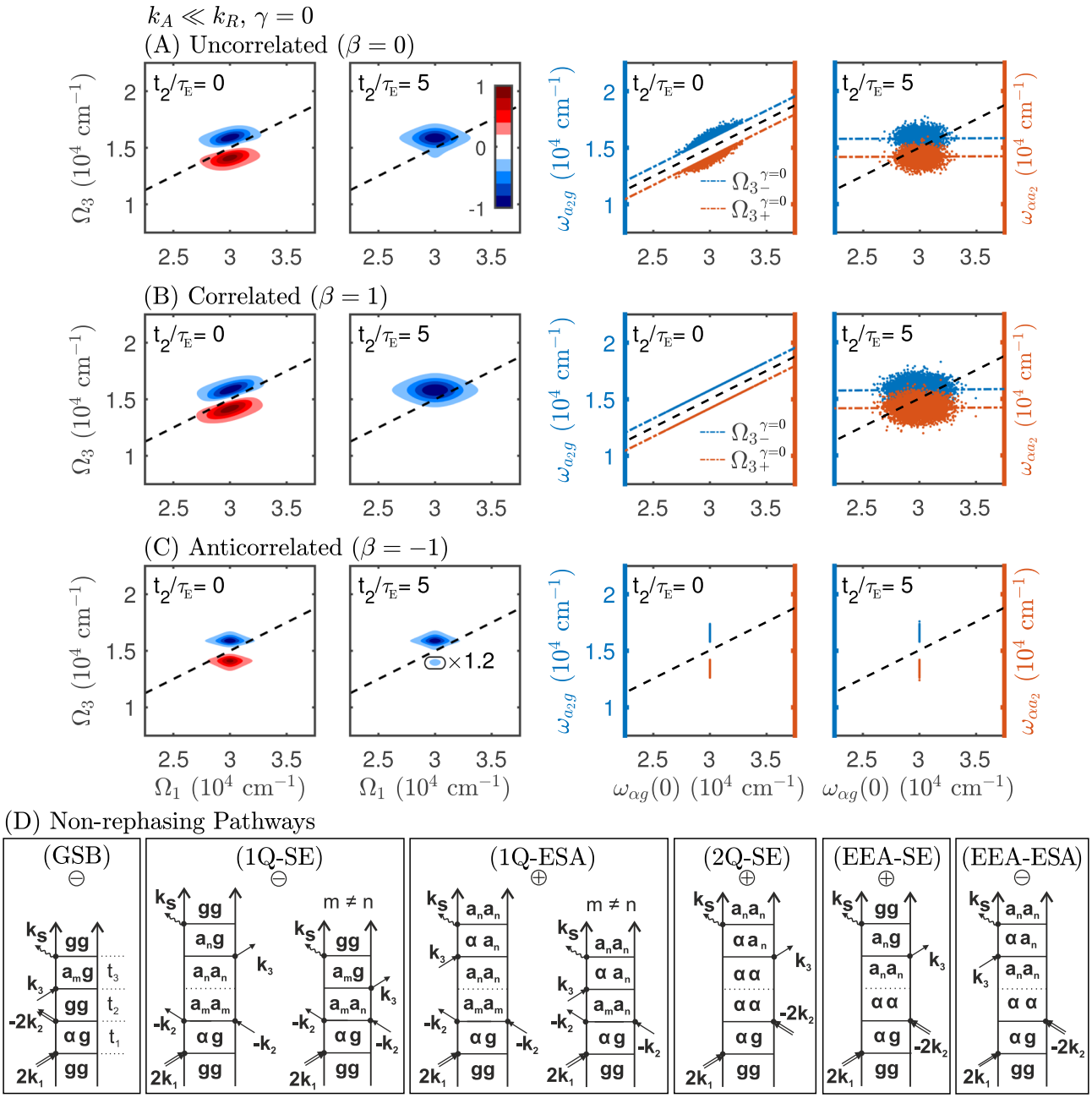

(D) Non-rephasing Pathways

FIG. 2. The first two panels (from left to right) in (a)–(c) depict R^5-2D line shapes of a homodimer for two different waiting times assuming slow annihilation dynamics ($k_A \ll k_R$). We chose $\bar{E}$ = 15 000 cm^{-1}, J = 800 cm^{-1}, $\bar{\Delta}$ = 0 cm^{-1}, σ_E = 600 cm^{-1}, $\gamma = 0$, τ_E = 100 fs, k_A^{-1} = 100 fs, and k_R^{-1} = 30 fs, and all line shapes are averaged over 40 000 realizations of the OU process. Fluctuations on the two sites are assumed to be (top to bottom) uncorrelated, correlated, and anticorrelated. R^5-2D signals are normalized to their minimum value at each waiting time. The minor negative feature below the main peak in the $t_2/\tau_E = 5$ map of the anticorrelated case is magnified by 20%. The two panels on the right map the process of dynamic disorder by correlating frequencies $\omega_{\alpha a_2}(t_2)$ (orange) and $\omega_{a_2 g}(t_2)$ (blue) with frequency $\omega_{\alpha g}(0)$ obtained from the OU trajectories. The dashed black line depicts the line $\Omega_3 = 0.5\Omega_1$. (d) Non-rephasing double-sided Feynman diagrams contributing to the dimer signal. The rephasing pathways can be found in Ref. 12.

variability without any reference to a specific line shape type. The forward center line (FCL) [backward center line (BCL)] obtained by maximizing the signal along Ω_3 (Ω_1) for fixed Ω_1 (Ω_3) is depicted in Fig. 3(a). Their slopes around the peak center of the negative peak are further analyzed as a function of t_2 in Figs. 3(b) and 3(c) for the three correlation cases. The value of the FCL and inverse of the BCL slope at $t_2/\tau_E = 0$ shows a clear dependence on β as it is increased (decreased) with the amount of positive (negative) correlation with respect to the uncorrelated case as can be seen from Figs. 3(b) and 3(c).

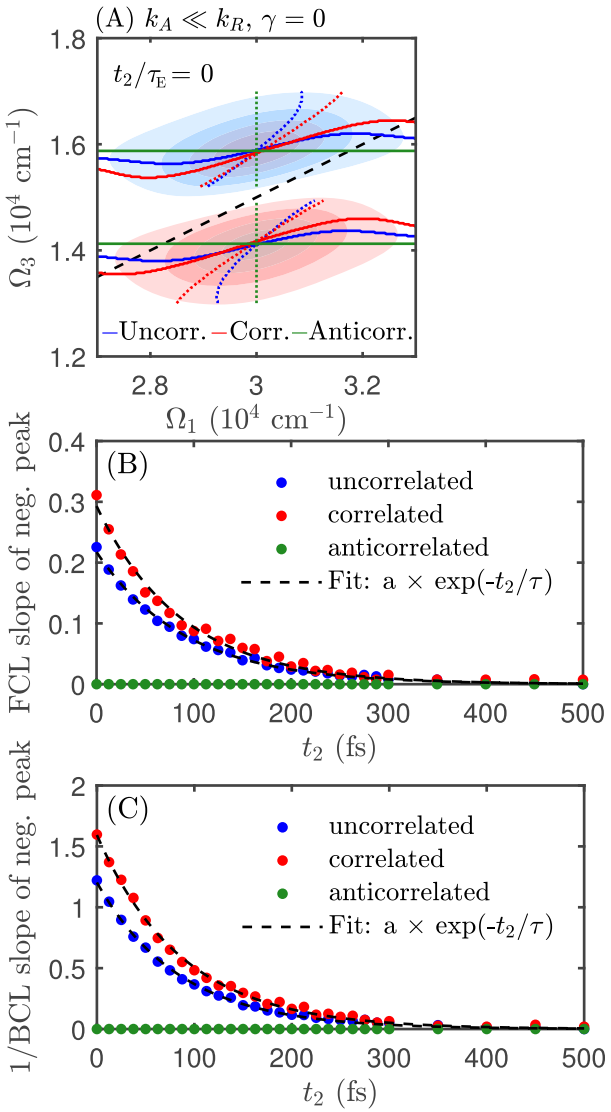

FIG. 3. (a) FCL (full lines) and BCL (dashed lines) for uncorrelated (blue), correlated (red), and anticorrelated (green) on-site fluctuations. The transparent R^5-2D line shapes in the background serve as a reference and are the same as in Fig. 2(a), i.e., uncorrelated and slow annihilation. (b) and (c) Slope of the FCL/BCL vs the waiting time t_2 for all correlation cases. The fit of the center line dynamics with a single exponential decay is depicted with dashed black lines.

The general temporal evolution of the negative peak's FCL and BCL slope is readily understood from analyzing the Gaussian approximation to the underlying statistics. We obtain

$$\left[\frac{\Omega_3 - \bar{\omega}_{a_2 g}}{\Omega_1^{BCL} - \bar{\omega}_{ag}}\right]^{-1} = 2C_E(t_2), \qquad \frac{\Omega_3^{FCL} - \bar{\omega}_{a_2 g}}{\Omega_1 - \bar{\omega}_{ag}} = \frac{1}{2}C_E(t_2), \tag{38}$$

for the time profile of the BCL and FCL, respectively. The evolution is thus governed by the correlation function $C_E(t_2)$, which describes an exponential decay with timescale τ_E. Fitting the FCL/BCL values obtained from the line shapes with a mono-exponential decay, we obtain a timescale of 90 fs ($\beta = 0$) or 85 fs ($\beta = 1$). Both values reflect well the relevant model input parameter, namely, the correlation timescale $\tau_E = 100$ fs. The center lines can thus be used to measure decorrelation similarly to R^3-2D.[18] Both the simulations depicted in Fig. 3 and the Gaussian analysis [symmetry Eq. (38)] additionally suggest that BCL and FCL report similarly on the tilts dynamics. However, in contrast to 2D-IR spectroscopy where a similar mirror symmetry is underlied by fundamental time reversal symmetry of stochastic dynamics at equilibrium [see Eq. (8) in Ref. 18], this observation here is approximate and limited to the present $\gamma = 0$ case (see Sec. III B).

While the Gaussian approximation to the CLs explains the observed decorrelation behavior, it is less successful to explain the sensitivity of the line shapes to inter-site correlation at zero, where vanishing sensitivity is predicted at $E_\delta = 0$, contrary to our simulations. The main problem with the analysis is that the approximate 1Q-2Q statistics does not capture the finite width of the distribution at $t_2/\tau_E = 0$ and more importantly has a singularity at that point in time. To remove the singularity, we investigate the 1Q-2Q statistics for finite but small site energy difference $E_\delta \neq 0$. The time profile of the FCL [Eq. (38)] is unchanged for the homodimer, but we obtain

$$\left[\frac{\Omega_3 - \bar{\omega}_{a_2 g}}{\Omega_1^{BCL} - \bar{\omega}_{ag}}\right]^{-1} = \frac{2(1+\beta)}{1+\varepsilon^2+(1-\varepsilon^2)\beta}C_E(t_2), \tag{39}$$

with

$$\varepsilon = \frac{E_\delta}{\sqrt{E_\delta^2 + 4J^2}}, \tag{40}$$

for the BCL. The degree of on-site correlation β thus changes the BCL dynamics directly by changing the underlying 1Q-2Q statistics [see Eq. (39)], but the observed β-dependence of the FCL rests in an interference effect between the various homogeneous contributions as the width of the 1Q-2Q distribution is increased with increasing β [see Eq. (B11)]. One is tempted to conclude from this result that there is a degeneracy between the FCL of the correlated and a rescaled uncorrelated model with the same amount of homogeneous broadening; the general scaling factor between the models is $\sqrt{1+\beta}$. However, comparing the CLS-values from the correlated model ($\beta = 1$) to a rescaled uncorrelated model (scaling factor $\sqrt{2}$), we find appreciable differences between the two scenarios for the

negative R^5-2D peak. Specifically, there is a 3% difference between the FCLs and an 8% difference between the BCLs for the correlated and uncorrelated model. Hence, CLS analysis in R^5-2D gives access to the site energy correlations quantified by β. These results are appealing as they suggest that having experimental data at hand, one can only find agreement between experimental and theoretical FCL (BCL) slope dynamics if the correlation between the sites is taken into account, implying that the slope of the CLs can be used to parameterize the type and amount of inter-site correlation β and also the fluctuation timescales.

At long waiting times ($t_2/\tau_E \gg 1$), the line shapes are decorrelated (zero slope of FCL) and asymmetrically stretched, as the 2Q statistics seen along Ω_1 is broader than 1Q along Ω_3. The standard deviation along Ω_1 and Ω_3 for both negative and positive peaks satisfies the relation

$$\sigma^2_{\pm,\Omega_1} = 4\sigma^2_{\pm,\Omega_3}. \tag{41}$$

The anticorrelated line shapes remain homogeneous at all t_2 times as the 1Q-2Q statistics is stable.

The previous discussion of Figs. 2 and 3 was worked out for slow annihilation dynamics, which is not always the case in small molecular aggregates.[14,38] In the following, we check the sensitivity of the line shapes to inter-site correlations also for fast annihilation ($k_A^{-1} \gg k_R^{-1}$). This parameter setting modifies substantially the underlying homogeneous broadening of coherences $|\alpha g\rangle\rangle$ and $|\alpha a_2\rangle\rangle$, but not coherence $|a_2 g\rangle\rangle$. The negative peak is thus broadened along Ω_1 and the positive peak along Ω_1 and Ω_3 axis, as depicted in Figs. 4(a) and 4(b). The case of anticorrelated fluctuations is again special: A higher degree of localization and redistribution of dipole strength lifts the clear separation between GSB, 1Q-SE, 1Q-ESA, and 2Q-SE pathways. Additional pathways in coherence $|\alpha a_2\rangle\rangle$ or $|a_1 g\rangle\rangle$ in t_3 thus contribute to the positive peak. The interference between narrow/negative (GSB, 1Q-SE) and broad/positive (1Q-ESA, 2Q-SE) contributions along Ω_3 leads to a split peak that is positive at the edges and negative in its center. We reported similar features for weakly coupled homodimers and heterodimers in Ref. 12.

We will in the following focus on the FCL, which will be shown in Sec. III B to be sensitive to both parameters of interest, i.e., β and γ. The FCLs obtained from the simulations are depicted in Fig. 5. The slope values are generally decreased compared to the case of slow annihilation but have a similar β-dependence. The initial FCL value is thus a complex function of the degree and sign of the on-site correlation and also the model parameter defining the (in)homogeneous width.

B. Autonomous bi-exciton fluctuations ($\gamma \neq 0$)

Our conclusions so far were derived from a model that neglects bi-exciton binding energy fluctuations. This is a common assumption made to reduce the number of independent model parameters for the fluctuations of the second excitonic manifold. R^5-2D is, however, a promising candidate to indicate shortcomings of this assumption, as fluctuations of frequency $\omega_{\alpha g}$ are tracked vs the waiting time t_2. In this section, we will thus give the bi-exciton state more freedom to fluctuate, i.e., $\gamma \neq 0$; otherwise, the line shapes and

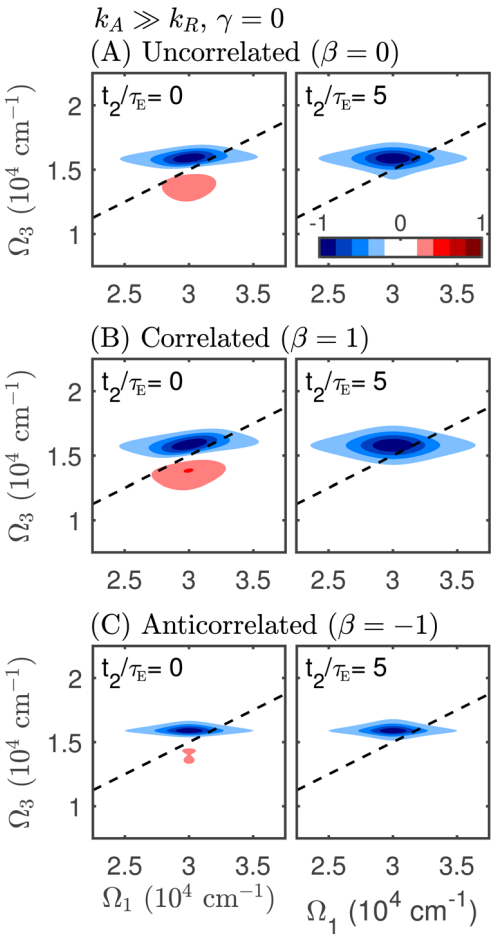

FIG. 4. R^5-2D line shapes of a homodimer assuming fast annihilation. We chose k_A^{-1} = 5 fs; other parameters are the same as in Fig. 2. The two sites are assumed to be (top to bottom) uncorrelated, correlated, and anticorrelated.

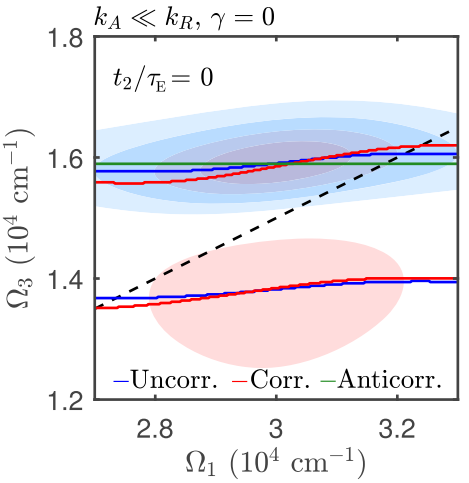

FIG. 5. FCL in the case of uncorrelated (blue), correlated (red), and anticorrelated (green) fluctuations. The transparent R^5-2D line shapes in the background are the same as in Fig. 4(a), i.e., uncorrelated fluctuations and fast annihilation.

1Q-2Q plots displayed in Fig. 6 are plotted for the same parameters as Fig. 2. Upon first inspection, we find that the tilts of the negative and positive peaks at $t_2/\tau_E = 0$ are quite different compared to the $\gamma = 0$ case for all values of β and still follow well the 1Q-2Q statistics plots shown on the right. To estimate the tilt, we again use the Gaussian approximation to the 1Q-2Q statistics and obtain

$$\tan[2\Phi_-(t_2)] = \frac{2(1+\beta)}{\gamma^2 + \frac{3}{2}(1+\beta)} C_E(t_2),$$
$$\tan[2\Phi_+(t_2)] = \frac{\gamma^2 C_\Delta(t_2) + (1+\beta) C_E(t_2)}{\frac{3}{4}(1+\beta)}, \tag{42}$$

for the negative and positive peak, respectively, with the normalized correlation function of the bi-exciton fluctuations,

$$C_\Delta(t) \equiv \frac{\Sigma^{(2)}(t)}{\Sigma^{(2)}(0)}. \tag{43}$$

The timescale of the bi-exciton fluctuations τ_Δ is thus encoded in the evolution of the positive peak, which disappears for the H-homodimer. The lines $\Omega_{3,\pm}^{\beta,\gamma}$ are depicted in the 1Q-2Q plots of Figs. 6(a) and 6(b) for the respective β value and $\gamma = 2$ and follow well the tilt of the correlation plots. For uncorrelated fluctuations ($\beta = 0$) with the same decorrelation time profile [$C_E(t) = C_\Delta(t)$], we can directly relate γ to the ratio

$$\frac{\tan[2\Phi_+(t_2)]}{\tan[2\Phi_-(t_2)]} \approx \left(\frac{2}{3}\gamma^2 + 1\right)\left(\gamma^2 + 1\right) \tag{44}$$

of angles (42). The differences in slopes $\Phi_\pm(t_2)$ are, thus, a direct indication of finite γ.

The anticorrelated site energies are again special: The negative peak is inhomogeneously broadened along Ω_1 by σ_Δ and along Ω_3 by the quadratic site energy difference similar to the $\gamma = 0$ model. The positive peak displays a tilt as peaks are shifted along the lines,

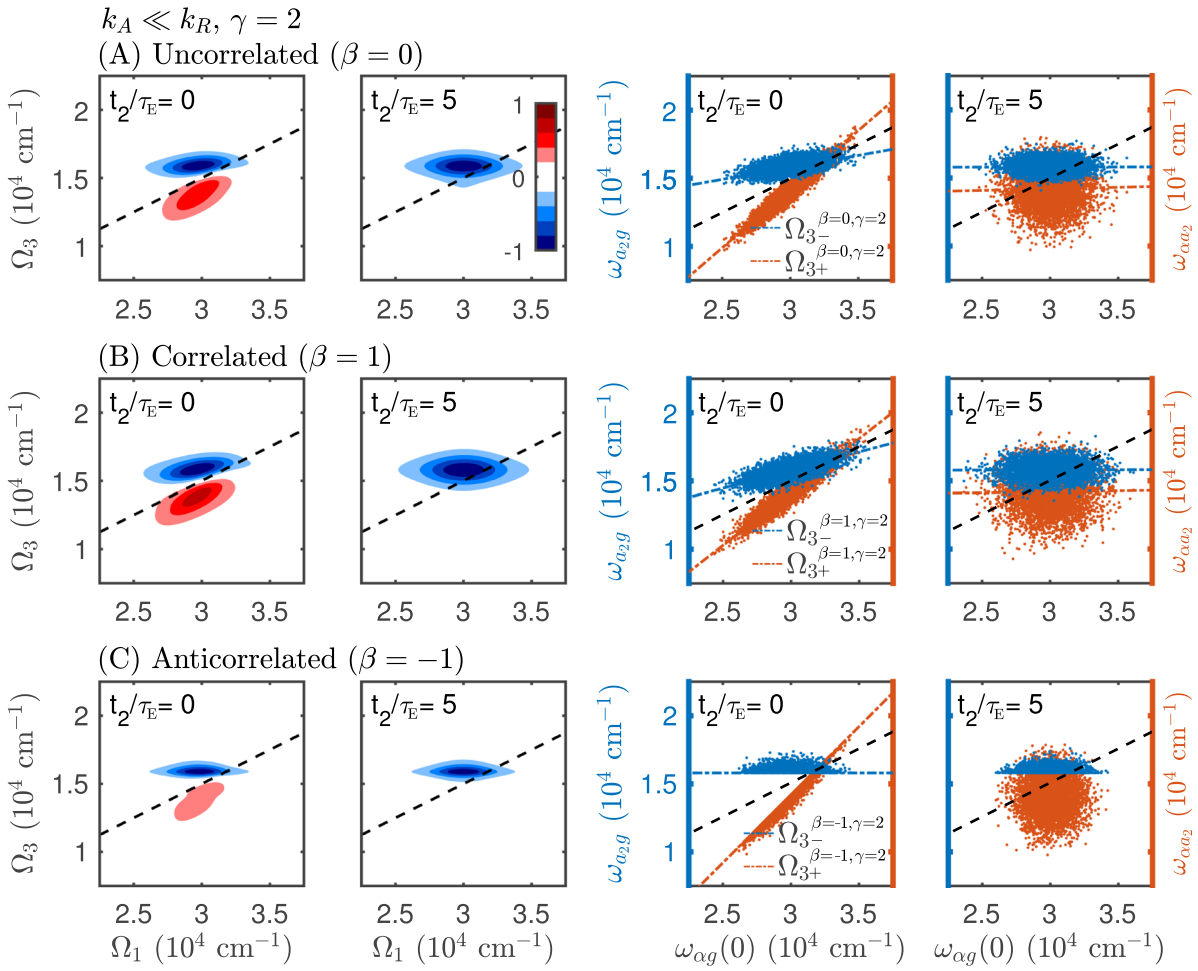

FIG. 6. Same as Figs. 2(a)–2(c), but $\gamma = 2$ and $\tau_E = \tau_\Delta = 100$ fs.

$$\Omega_{3,-}^{\beta=-1,\gamma\neq 0} = \bar{E} + J,$$
$$\Omega_{3,+}^{\beta=-1,\gamma\neq 0} = \Omega_1 - \bar{E} - J, \tag{45}$$

which leads to a slightly more homogeneous spectrum compared to the $\gamma = 0$ model.

The $t_2/\tau_E = 0$ line shapes depicted in Fig. 6 follow well their corresponding 1Q-2Q statistics, but the actual tilt (FCL/BCL slope) of the line shapes is again modified by model parameters defining homogeneous broadening. The degree of correlation β is again seen in the increasingly strict alignment of the negative peak's tilt, as depicted in Fig. 7. The positive peak shows a different behavior, as the FCL slope of the correlated case is smaller than the uncorrelated case, and the FCL slope of the anticorrelated case is not defined as the FCL displays a step due to the double-peak structure, similar to the discussed case of fast annihilation. The positive peak's slope of the H-homodimer should thus be analyzed carefully as it is not always well defined.

For the temporal evolution of the FCL and BCL of the negative peak, we find

$$\left[\frac{\Omega_3 - \tilde{\omega}_{a_2 g}}{\Omega_1^{BCL} - \tilde{\omega}_{ag}}\right]^{-1} = 2C_E(t_2),$$
$$\frac{\Omega_3^{FCL} - \tilde{\omega}_{a_2 g}}{\Omega_1 - \tilde{\omega}_{ag}} = \frac{1+\beta}{\gamma^2 + 2(1+\beta)} C_E(t_2), \tag{46}$$

highlighting the sensitivity of the FCL to both β and γ. The case of $\beta = -1$ is again special as the negative peak displays no line shape dynamics. The changes in the 1Q-2Q statistics of the positive peak are not visible in the line shapes as this peak disappears for the H-homodimer.

At long waiting times ($t_2/\tau_E \gg 1$), the line shapes are decorrelated [zero FCL, see Eq. (46)] and again asymmetrically stretched.

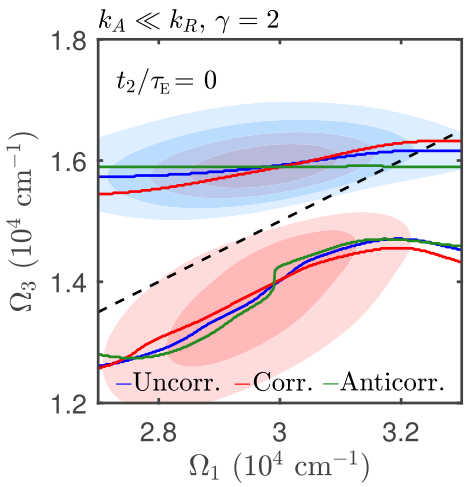

FIG. 7. FCL in the case of uncorrelated (blue), correlated (red), and anticorrelated (green) fluctuations. The transparent R^5-2D line shapes in the background are the same as in Fig. 6(a), i.e., uncorrelated and slow annihilation.

The standard deviations along Ω_1 and Ω_3 are, however, different for the negative

$$\sigma^2_{-,\Omega_1} \equiv 2(1+\beta)\sigma_E^2 + \sigma_\Delta^2,$$
$$\sigma^2_{-,\Omega_3} \equiv \frac{1}{2}(1+\beta)\sigma_E^2 \tag{47}$$

and positive

$$\sigma^2_{+,\Omega_1} = \sigma^2_{-,\Omega_1},$$
$$\sigma^2_{+,\Omega_3} \equiv \sigma^2_{-,\Omega_3} + \sigma_\Delta^2, \tag{48}$$

peak. From Eqs. (47) and (48), we can understand the observed additional stretching along Ω_1 as a result from the bi-exciton fluctuation magnitude σ_Δ^2.

IV. CONCLUSION

We present a model of spectral fluctuations in fifth-order spectroscopy of an excitonically coupled system and demonstrated that R^5-2D line shapes are able to quantify correlations between site energies, without the need to analyze beatings in R^3-2D signals. Hence, the methods discussed here can contribute to the discussion on the suggested role of site energy correlations in energy transport through biological light harvesting systems.[5,6]

In particular, we accounted for the effect of dynamic disorder in R^5-2D line shapes of a molecular H-homodimer. We based the model on the master equation formalism of Ref. 12, which ensures a thermodynamically consistent transport description and added a slow stochastic classical coordinate to address the peak tilt and its delay time dynamics. The timescale separation between the fast bath fluctuations responsible for transport and slow fluctuations inducing line-shaping effects is a key assumption for the present strategy and avoids the shortcomings of the individual components: purely homogeneous line shapes of a master equation approach and high temperature equilibrium between excitons set by stochastic quantum dynamics.[21] Justified alternatives to the present approach exist, but they are less feasible from a computational point of view: Stochastic quantum dynamics can be brought to finite temperatures by the hierarchical equations of motion (HEOM),[39] but procedures to calculate line shapes of multi-excitonic systems[34] or attempts to untangle HEOM into stochastic trajectories are numerically challenging even for the simplest aggregates.

In an extension of the strategy presented in Appendix B to approximate statistics of transition frequencies, the Gaussian character of typical noise can also justify a treatment of the diagonal fluctuations by the second cumulant,[33,37] while the effects of slow off-diagonal fluctuations on line shapes (beyond their contribution to transport rates) is omitted. Such an alternative strategy thus ignores, e.g., possible dipole redistribution, as discussed below Fig. 2(c) or in Ref. 34, and is not recommendable before more sophisticated accounts of off-diagonal disorder are included into the cumulant approach.[40]

Within our presented model, we found a tilt—quantified with the aid of CLS—of the R^5-2D line shapes and connected its waiting time dynamics with autocorrelation timescales of on-site fluctuations τ_E and bi-exciton binding energy fluctuations τ_Δ. We additionally found that the negative peak of the H-homodimer—related

TABLE I. Comparison of the correlation statistics of coherent 2D techniques (R^5-2D: $\pm 2\vec{K}_1 \mp 2\vec{K}_2 + \vec{K}_3$, R^3-2D: $\pm\vec{K}_1 \mp \vec{K}_2 + \vec{K}_3$, and 2Q-$R^3$-2D: $+\vec{K}_1 + \vec{K}_2 - \vec{K}_3$) measured on a homodimer. All signals display a two-peak structure reflecting transition frequencies ω_{ag} and $\omega_{\alpha a}$ along Ω_3, and both peaks are centered either at ω_{ag} or $\omega_{\alpha g}$ along Ω_1. Their line shapes, however, represent different types of correlation functions as summarized in this table.

Signal type	Correlation statistics related to the observed peaks
R^5-2D	$\langle\delta(\Omega_1 - \omega_{\alpha g}(0))\delta(\Omega_3 - \omega_{ag}(t_2))\rangle$
	$\langle\delta(\Omega_1 - \omega_{\alpha g}(0))\delta(\Omega_3 - \omega_{\alpha a}(t_2))\rangle$
R^3-2D	$\langle\delta(\Omega_1 - \omega_{ag}(0))\delta(\Omega_3 - \omega_{ag}(t_2))\rangle$
	$\langle\delta(\Omega_1 - \omega_{ag}(0))\delta(\Omega_3 - \omega_{\alpha a}(t_2))\rangle$
2Q-R^3-2D	$\langle\delta(\Omega_2 - \omega_{\alpha g}(0))\delta(\Omega_3 - \omega_{ag}(0))\rangle$
	$\langle\delta(\Omega_2 - \omega_{\alpha g}(0))\delta(\Omega_3 - \omega_{\alpha a}(0))\rangle$

to frequency pairs $(\omega_{\alpha g}(0), \omega_{a_2 g}(t_2))$—is generally better suited to extract CLS dynamics than the positive peak. A CLS analysis of the negative peak showed that the FCL of the peak is sensitive to both the amount of inter-site correlation β and the magnitude γ of independent bi-exciton binding energy fluctuations. As a rule of thumb, we find that the bi-exciton binding energies are fluctuating independently if the peaks of the H-dimer are asymmetrically tilted [see Eq. (44)] at $t_2/\tau_E = 0$.

Information about inter-site correlation is challenging to obtain from steady state[41–44] or third order time resolved spectroscopic techniques such as pump probe[45–47] or R^3-2D.[48,49] The main advantage of R^5-2D over these methods is that two-exciton fluctuations can be tracked over the waiting time period unlike linear and third-order techniques, as can be seen from Table I where we summarized the different correlation functions of various non-linear techniques to highlight this point.

These results shed new light on the R^5-2D technique as experimental and theoretical studies focused so far on the temporal evolution of specific peaks or the integrated signal to extract annihilation or diffusion timescales in molecular aggregates, but a line shape analysis—beyond pulse related artifacts[50]—has been omitted. We showed that R^5-2D line shapes are rich in information and are essential to analyze the coordination between spectral fluctuations of nearby molecules and bi-exciton binding energies.

ACKNOWLEDGMENTS

J.H. and C.H. acknowledge support by the Deutsche Forschungsgemeinschaft (DFG, German Research Foundation) through TUM International Graduate School of Science and Engineering (IGSSE), GSC 81, and funding by DFG under Germany's Excellence Strategy—EXC 2089/1-390776260. Mobility is supported by project "Exciton–exciton annihilation probed by non-linear spectroscopy" (MSMT Grant No. 8J19DE009, DAAD-Project No. 57444962).

AUTHOR DECLARATIONS

Conflict of Interest

The authors have no conflicts to disclose.

DATA AVAILABILITY

The data that support the findings of this study are available from the corresponding author upon reasonable request.

APPENDIX A: QUANTUM MASTER EQUATION FOR EXCITON TRANSPORT AND ANNIHILATION

In this appendix, we summarize for the reader's convenience the master equation model for exciton transport and annihilation. We follow closely our derivation presented in Ref. 12 for the stochastic version of the model in this work. We work in natural units where the Planck constant $\hbar$, the speed of light c, and the Boltzmann constant k_B are set to one, i.e., $\hbar = c = k_B = 1$.

We shall start with the time scale separation where the slow classical fluctuations are singled out from Eq. (1) and the free Hamiltonian[22]

$$\hat{H}_0(\{q\}) = \sum_{n=1}^{N} \hat{E}_n(\{q\})\hat{B}_n^\dagger \hat{B}_n + \sum_{\substack{n,m=1 \\ n\neq m}}^{N} J_{nm}\hat{B}_n^\dagger \hat{B}_m + \sum_{\substack{n,m=1 \\ n\neq m}}^{N} \frac{\hat{\Delta}_{nm}(\{q\})}{2}\hat{B}_n^\dagger \hat{B}_m^\dagger \hat{B}_n \hat{B}_m \tag{A1}$$

is considered at a fixed value of q. In contrast, the fast bath coordinates $\hat{Q}_n$ affecting the site energies are quantum and dynamical. Their time-dependent (Dirac) picture is defined with respect to the bath Hamiltonian, i.e., $\hat{Q}_n(t) \equiv e^{i\hat{H}_B t}\hat{Q}_n e^{-i\hat{H}_B t}$. We standardly assume $\hat{H}_B$ to be harmonic and, additionally, that coordinates $\hat{Q}_n$ are mutually uncorrelated and overdamped, i.e., the correlation function

$$C_n^{(Q)}(t) = \langle \hat{Q}_n(t)\hat{Q}_n \rangle \tag{A2}$$

assumes the form

$$\tilde{C}_n^{(Q)}(\omega) = \left[1 + \coth\left(\frac{\omega}{2T}\right)\right] 2\lambda_n \frac{\omega\Lambda_n}{\omega^2 + \Lambda_n^2} \tag{A3}$$

in the frequency domain $(\tilde{C}_n^{(Q)}(\omega) \equiv \int_{-\infty}^{\infty} C_n^{(Q)}(t)e^{-i\omega t}dt)$.[51] The reorganization energy λ_n measures the magnitude of fluctuations, Λ_n is the bath relaxation rate ($\Lambda \gg \lambda$ defines the assumed fast bath limit), and T is the temperature.

The Redfield master equation (9) is a perturbative expansion in $\lambda \ll J$, and the dissipative (transport) dynamics thus appear between delocalized eigenstates $|\varepsilon_i(\{q\})\rangle$ of the Frenkel exciton Hamiltonian (A1) and the dissipative part of Eq. (10), thus, reads

$$\check{\mathcal{D}}(\{q\})|\rho(t)\rangle\rangle = \sum_{i,j=1;i\neq j}^{2^N} \left[k_{\varepsilon_i\to\varepsilon_j}\left(|\varepsilon_j\rangle\langle\varepsilon_i|\hat{\rho}(t)|\varepsilon_i\rangle\langle\varepsilon_j| - \frac{1}{2}\{|\varepsilon_i\rangle\langle\varepsilon_i|, \hat{\rho}(t)\}\right) - \gamma_{\varepsilon_i\varepsilon_j}^{pd}|\varepsilon_i\rangle\langle\varepsilon_i|\hat{\rho}(t)|\varepsilon_j\rangle\langle\varepsilon_j| \right], \tag{A4}$$

where $\{\hat{A}, \hat{B}\} \equiv \hat{A}\hat{B} + \hat{B}\hat{A}$. We omitted for readability the q dependence of the excitonic states, transport rates, and pure dephasing

rates on the right-hand side of Eq. (A4). Transport rates from the excitonic state $|\varepsilon_i(\{q\})\rangle$ to $|\varepsilon_j(\{q\})\rangle$ are given by

$$k_{\varepsilon_i\to\varepsilon_j}(\{q\}) = \sum_{n=1}^{N} \tilde{C}_n^{(Q)}(\omega_{\varepsilon_i\varepsilon_j})\left|\langle\varepsilon_i|\hat{B}_n^\dagger\hat{B}_n|\varepsilon_j\rangle\right|^2, \tag{A5}$$

where $\omega_{\varepsilon_i\varepsilon_j}(\{q\})$ is the electronic energy gap between eigenstates $|\varepsilon_i(\{q\})\rangle$ and $|\varepsilon_j(\{q\})\rangle$.

The pure dephasing rates $\gamma^{pd}_{\varepsilon_i\varepsilon_j}(\{q\})$ are given by

$$\gamma^{pd}_{\varepsilon_i\varepsilon_j}(\{q\}) = \frac{1}{2}\sum_{n=1}^{N}\tilde{C}_n^{(Q)}(0)\left[\langle\varepsilon_i|\hat{B}_n^\dagger\hat{B}_n|\varepsilon_i\rangle - \langle\varepsilon_j|\hat{B}_n^\dagger\hat{B}_n|\varepsilon_j\rangle\right]^2, \tag{A6}$$

where the limit $\omega \to 0$ of Eq. (A3) reads

$$\tilde{C}_n^{(Q)}(0) = \frac{4T\lambda_n}{\Lambda_n}. \tag{A7}$$

The fast bi-exciton bath coordinates $\hat{Q}_{nm}$ induce transport and fluctuations in complete analogy with Eqs. (A1)–(A7) (see Ref. 8). No bi-exciton transport is, however, possible for the presented dimer with a single bi-exciton state, and they thus solely induce trivial pure dephasing. The latter makes no appreciable difference to the line shapes and has thus been set to zero in the presented simulations of Figs. 2–7.

EEA is added to the model phenomenologically as unidirectional transport between excitonic manifolds differing in one quantum of excitation when adjacent chromophores are occupied,

$$\check{\mathscr{A}}|\rho(t)\rangle\rangle = \sum_{i=1}^{N-1} k_i^A\left(\left[\hat{L}_i^{(-)}\hat{\rho}\hat{L}_i^{(-)\dagger} - \frac{1}{2}\left\{\hat{L}_i^{(-)\dagger}\hat{L}_i^{(-)},\hat{\rho}(t)\right\}\right] + \left[\hat{L}_i^{(+)}\hat{\rho}\hat{L}_i^{(+)\dagger} - \frac{1}{2}\left\{\hat{L}_i^{(+)\dagger}\hat{L}_i^{(+)},\hat{\rho}(t)\right\}\right]\right). \tag{A8}$$

The operators

$$\hat{L}_i^{(-)} \equiv B_{i+1}^\dagger B_{i+1} B_i \tag{A9}$$

and

$$\hat{L}_i^{(+)} \equiv B_i^\dagger B_i B_{i+1} \tag{A10}$$

describe, respectively, EEA with rate k_i^A at site i ($\hat{L}_i^{(-)}$) or $i+1$ ($\hat{L}_i^{(+)}$), if two excitons are present at sites i and $i+1$.

APPENDIX B: GAUSSIAN APPROXIMATION TO 1Q-2Q STATISTICS

The 1Q-2Q statistics defined in Eqs. (33) and (34) can be approximated by a bivariate Gaussian distribution for small fluctuations. To obtain analytical expressions, we expand eigenenergies (28) linearly in stochastic coordinates $\{q(t)\}$,

$$\begin{aligned}
\omega_{\alpha g}(t) &= \bar{\omega}_{\alpha g} + \delta E_1(t) + \delta E_2(t) + \delta\Delta(t),\\
\omega_{a_2 g}(t) &\approx \bar{\omega}_{a_2 g} + \frac{\delta E_1(t)+\delta E_2(t)}{2} + \frac{E_\delta}{2}\frac{\delta E_1(t)-\delta E_2(t)}{\sqrt{E_\delta^2+4J^2}},\\
\omega_{\alpha a_2}(t) &= \omega_{\alpha g}(t) - \omega_{a_2 g}(t)\\
&\approx \bar{\omega}_{\alpha a_2} + \frac{\delta E_1(t)+\delta E_2(t)}{2}\\
&\quad - \frac{E_\delta}{2}\frac{\delta E_1(t)-\delta E_2(t)}{\sqrt{E_\delta^2+4J^2}} + \delta\Delta(t).
\end{aligned} \tag{B1}$$

We allow for the general dimer model with small site energy difference

$$E_\delta \equiv \tilde{E}_1 - \tilde{E}_2, \tag{B2}$$

with fluctuation profiles

$$\begin{aligned}
\delta E_{1,2}(t) &= E_{1,2}(t) - \tilde{E}_{1,2},\\
\delta\Delta(t) &= \Delta(t) - \tilde{\Delta},
\end{aligned} \tag{B3}$$

and mean transition energies

$$\begin{aligned}
\bar{\omega}_{\alpha g} &\equiv \tilde{E}_1 + \tilde{E}_2 + \tilde{\Delta},\\
\bar{\omega}_{a_2 g} &\equiv \frac{\tilde{E}_1+\tilde{E}_2}{2} + \sqrt{\left(\frac{E_\delta}{2}\right)^2 + J^2},\\
\bar{\omega}_{\alpha a_2} &\equiv \frac{\tilde{E}_1+\tilde{E}_2}{2} - \sqrt{\left(\frac{E_\delta}{2}\right)^2 + J^2} + \tilde{\Delta}.
\end{aligned} \tag{B4}$$

This general dimer model with small site energy difference E_δ provides insight into certain line shape singularities treated in Eq. (39).

As the Gaussian character of the distributions is maintained under linear transformations (B1), we finally arrive at the following bivariate Gaussian distributions for the 1Q-2Q statistics:

$$\tilde{P}_\pm(\Omega_{1,\pm}, t_2, \Omega_{3,\pm}) \approx \frac{1}{2\pi b_\pm(t_2)}(\exp) - \frac{\Omega_{1,\pm}^2\sigma_{\pm,\Omega_3}^2 + \Omega_{3,\pm}^2\sigma_{\pm,\Omega_1}^2 - 2\Omega_{1,\pm}\Omega_{3,\pm}\xi_\pm(t_2)}{2b_\pm^2(t_2)}, \tag{B5}$$

with the definitions for the negative

$$
\begin{aligned}
\Omega_{1,-} &\equiv \Omega_1 - \tilde{\omega}_{\alpha g},\\
\Omega_{3,-} &\equiv \Omega_3 - \tilde{\omega}_{a_2 g},\\
\sigma^2_{-,\Omega_1} &\equiv \Sigma^{(2)}(0) + \Sigma^{(1)}_{11}(0) + 2\Sigma^{(1)}_{12}(0) + \Sigma^{(1)}_{22}(0),\\
\sigma^2_{-,\Omega_3} &\equiv \frac{1}{4}\left(\left[1+\frac{E_\delta}{\sqrt{E_\delta^2+4J^2}}\right]^2\Sigma^{(1)}_{11}(0)+2\Sigma^{(1)}_{12}(0)\left(1-\frac{E_\delta^2}{E_\delta^2+4J^2}\right)\right.\\
&\quad\left.+\left[1-\frac{E_\delta}{\sqrt{E_\delta^2+4J^2}}\right]^2\Sigma^{(1)}_{22}(0)\right),\\
\xi_-(t_2) &\equiv \frac{1}{2}\left(\left[1+\frac{E_\delta}{\sqrt{E_\delta^2+4J^2}}\right]\Sigma^{(1)}_{11}(t_2)+2\Sigma^{(1)}_{12}(t_2)\right.\\
&\quad\left.+\left[1-\frac{E_\delta}{\sqrt{E_\delta^2+4J^2}}\right]\Sigma^{(1)}_{22}(t_2)\right),\\
b^2_-(t_2) &\equiv \sigma^2_{-,\Omega_1}\sigma^2_{-,\Omega_3} - \xi^2_-(t_2)
\end{aligned}
\tag{B6}
$$

and positive

$$
\begin{aligned}
\Omega_{1,+} &\equiv \Omega_1 - \tilde{\omega}_{\alpha g},\\
\Omega_{3,+} &\equiv \Omega_3 - \tilde{\omega}_{\alpha a_2},\\
\sigma^2_{+,\Omega_1} &= \sigma^2_{-,\Omega_1},\\
\sigma^2_{+,\Omega_3} &\equiv \frac{1}{4}\left(\left[1-\frac{E_\delta}{\sqrt{E_\delta^2+4J^2}}\right]^2\Sigma^{(1)}_{11}(0)+2\Sigma^{(1)}_{12}(0)\left(1-\frac{E_\delta^2}{E_\delta^2+4J^2}\right)\right.\\
&\quad\left.+\left[1+\frac{E_\delta}{\sqrt{E_\delta^2+4J^2}}\right]^2\Sigma^{(1)}_{22}(0)\right)+\Sigma^{(2)}(0),\\
\xi_+(t_2) &\equiv \frac{1}{2}\left(\left[1-\frac{E_\delta}{\sqrt{E_\delta^2+4J^2}}\right]\Sigma^{(1)}_{11}(t_2)+2\Sigma^{(1)}_{12}(t_2)\right.\\
&\quad\left.+\left[1+\frac{E_\delta}{\sqrt{E_\delta^2+4J^2}}\right]\Sigma^{(1)}_{22}(t_2)\right)+\Sigma^{(2)}(t_2),\\
b^2_+(t_2) &\equiv \sigma^2_{+,\Omega_1}\sigma^2_{+,\Omega_3} - \xi^2_+(t_2)
\end{aligned}
\tag{B7}
$$

2D peaks. Equation (B5) can be formally identified with the absorptive line shapes if the slow ($\sigma\tau \gg 1$) diagonal spectral fluctuations are the only relevant dynamical process, i.e., when transport and annihilation dynamics are neglected. The time-dependent angle of the principal axis of elliptic contours (B5) reads

$$
\tan[2\Phi_\pm(t_2)] = \frac{2\xi_\pm(t_2)}{\sigma^2_{\pm,\Omega_1} - \sigma^2_{\pm,\Omega_3}}. \tag{B8}
$$

The FCL and BCL of the positive and negative peak are obtained with

$$
\begin{aligned}
\frac{\partial}{\partial\Omega_1}\tilde{P}_\pm(\Omega_1,t_2,\Omega_3)\Big|_{\Omega_1=\Omega_1^{BCL}} &= 0,\\
\frac{\partial}{\partial\Omega_3}\tilde{P}_\pm(\Omega_1,t_2,\Omega_3)\Big|_{\Omega_3=\Omega_3^{FCL}} &= 0,
\end{aligned}
\tag{B9}
$$

and read

$$
\begin{aligned}
\left[\frac{\Omega_{3,\pm}}{\Omega^{BCL}_{1,\pm}}\right]^{-1} &= \frac{\xi_\pm(t_2)}{\sigma^2_{\pm,\Omega_3}},\\
\left[\frac{\Omega^{FCL}_{3,\pm}}{\Omega_{1,\pm}}\right] &= \frac{\xi_\pm(t_2)}{\sigma^2_{\pm,\Omega_1}}.
\end{aligned}
\tag{B10}
$$

The diagonal (major) and anti-diagonal (minor) semidiameter of elliptical contours (B5) are given by

$$
\begin{aligned}
\sigma^2_{\mathrm{diag},\pm} &= \frac{\sigma^2_{\pm,\Omega_1}+\sigma^2_{\pm,\Omega_3}}{2} + \sqrt{\left(\frac{\sigma^2_{\pm,\Omega_1}-\sigma^2_{\pm,\Omega_3}}{2}\right)^2+\xi^2_\pm(t_2)},\\
\sigma^2_{anti-\mathrm{diag},\pm} &= \frac{\sigma^2_{\pm,\Omega_1}+\sigma^2_{\pm,\Omega_3}}{2} - \sqrt{\left(\frac{\sigma^2_{\pm,\Omega_1}-\sigma^2_{\pm,\Omega_3}}{2}\right)^2+\xi^2_\pm(t_2)},
\end{aligned}
\tag{B11}
$$

respectively.

The limit of $E_\delta = 0$ is used to derive Eqs. (35), (36), (38), (41), (42), and (46)–(48) of the main text. The full $\tilde{E}_\delta \neq 0$ form is helpful to approach the line shape singularity for $\gamma = 0$ at $t_2 = 0$ fs [see Eq. (39)].

REFERENCES

[1] T. Renger, V. May, and O. Kühn, Phys. Rep. **343**, 137 (2001).
[2] S. F. Huelga and M. B. Plenio, Contemp. Phys. **54**, 181 (2013).
[3] V. Perlík, J. Seibt, L. J. Cranston, R. J. Cogdell, C. N. Lincoln, J. Savolainen, F. Šanda, T. Mančal, and J. Hauer, J. Chem. Phys. **142**, 212434 (2015).
[4] J. C. Dean, T. Mirkovic, Z. S. D. Toa, D. G. Oblinsky, and G. D. Scholes, Chem **1**, 858 (2016).
[5] B. S. Rolczynski, H. Zheng, V. P. Singh, P. Navotnaya, A. R. Ginzburg, J. R. Caram, K. Ashraf, A. T. Gardiner, S.-H. Yeh, S. Kais, R. J. Cogdell, and G. S. Engel, Chem **4**, 138 (2018).
[6] J. Cao, R. J. Cogdell, D. F. Coker, H.-G. Duan, J. Hauer, U. Kleinekathöfer, T. L. C. Jansen, T. Mančal, R. J. D. Miller, J. P. Ogilvie, V. I. Prokhorenko, T. Renger, H.-S. Tan, R. Tempelaar, M. Thorwart, E. Thyrhaug, S. Westenhoff, and D. Zigmantas, Sci. Adv. **6**, eaaz4888 (2020).
[7] L. Wang, M. A. Allodi, and G. S. Engel, Nat. Rev. Chem. **3**, 477 (2019).
[8] O. Rancova, R. Jankowiak, and D. Abramavicius, J. Phys. Chem. B **122**, 1348 (2018).
[9] B. Brüggemann and T. Pullerits, New J. Phys. **13**, 025024 (2011).
[10] J. Dostál, F. Fennel, F. Koch, S. Herbst, F. Würthner, and T. Brixner, Nat. Commun. **9**, 2466 (2018).
[11] V. May, J. Chem. Phys. **140**, 054103 (2014).
[12] C. Heshmatpour, J. Hauer, and F. Šanda, Chem. Phys. **528**, 110433 (2020).
[13] J. Lüttig, T. Brixner, and P. Malý, J. Chem. Phys. **154**, 154202 (2021).
[14] C. Heshmatpour, P. Malevich, F. Plasser, M. Menger, C. Lambert, F. Šanda, and J. Hauer, J. Phys. Chem. Lett. **11**, 7776 (2020).
[15] P. Malý, J. Lüttig, A. Turkin, J. Dostál, C. Lambert, and T. Brixner, Chem. Sci. **11**, 456 (2020).
[16] S. T. Roberts, J. J. Loparo, and A. Tokmakoff, J. Chem. Phys. **125**, 084502 (2006).
[17] K. Kwak, S. Park, I. J. Finkelstein, and M. D. Fayer, J. Chem. Phys. **127**, 124503 (2007).

[18]F. Šanda, V. Perlík, C. N. Lincoln, and J. Hauer, J. Phys. Chem. A **119**, 10893 (2015).
[19]F. Šanda and S. Mukamel, Phys. Rev. Lett. **98**, 080603 (2007).
[20]G. E. Uhlenbeck and L. S. Ornstein, Phys. Rev. **36**, 823 (1930).
[21]R. Kubo, J. Phys. Soc. Jpn. **9**, 935 (1954).
[22]J. Frenkel, Phys. Rev **37**, 1276 (1931).
[23]V. Sláma, V. Perlík, H. Langhals, A. Walter, T. Mančal, J. Hauer, and F. Šanda, Front. Chem. **8**, 579166 (2020).
[24]D. Abramavicius, B. Palmieri, D. V. Voronine, F. Šanda, and S. Mukamel, Chem. Rev. **109**, 2350 (2009).
[25]M. D. Donsker, Mem. Am. Math. Soc. **6**, 1 (1951).
[26]N. J. Higham, Wiley Interdiscip. Rev.: Comput. Stat. **1**, 251 (2009).
[27]V. May and O. Kuhn, *Charge and Energy Transfer Dynamics in Molecular Systems* (Wiley-VCH Verlag, 2011).
[28]A. G. Redfield, IBM J. Res. Dev. **1**, 19 (1957).
[29]T. Pullerits, M. Chachisvilis, and V. Sundström, J. Phys. Chem. **100**, 10787 (1996).
[30]B. Brüggemann, J. L. Herek, V. Sundström, T. Pullerits, and V. May, J. Phys. Chem. B **105**, 11391 (2001).
[31]B. Brüggemann, N. Christensson, and T. Pullerits, Chem. Phys. **357**, 140 (2009).
[32]R. Kubo, J. Phys. Soc. Jpn. **12**, 570 (1957).
[33]S. Mukamel, *Principles of Nonlinear Optical Spectroscopy* (Oxford University Press, 1995).
[34]F. Šanda and S. Mukamel, J. Phys. Chem. B **112**, 14212 (2008).
[35]U. Fano, Rev. Mod. Phys. **29**, 74 (1957).
[36]R. W. Zwanzig, *Lectures in Theoretical Physics* (Interscience, New York, NY, 1960), Vol. 3, p. 106.
[37]V. Perlík and F. Šanda, J. Chem. Phys. **147**, 084104 (2017).
[38]P. Malý, S. Mueller, J. Lüttig, C. Lambert, and T. Brixner, J. Chem. Phys. **153**, 144204 (2020).
[39]Y. Tanimura, J. Chem. Phys. **153**, 020901 (2020).
[40]D. Abramavicius, L. Valkunas, and S. Mukamel, Europhys. Lett. **80**, 17005 (2007).
[41]F. Domínguez-Adame, Phys. Rev. B **51**, 12801 (1995).
[42]V. A. Malyshev, A. Rodríguez, and F. Domínguez-Adame, Phys. Rev. B **60**, 14140 (1999).
[43]E. W. Knapp, Chem. Phys. **85**, 73 (1984).
[44]M. Bednarz and P. Reineker, J. Lumin. **119–120**, 482 (2006).
[45]J. Knoester, J. Lumin. **58**, 107 (1994).
[46]J. Knoester, J. Chem. Phys. **99**, 8466 (1993).
[47]J. R. Durrant, J. Knoester, and D. A. Wiersma, Chem. Phys. Lett. **222**, 450 (1994).
[48]D. Abramavicius and S. Mukamel, J. Chem. Phys. **134**, 174504 (2011).
[49]J. Lim, D. J. Ing, J. Rosskopf, J. Jeske, J. H. Cole, S. F. Huelga, and M. B. Plenio, J. Chem. Phys. **146**, 024109 (2017).
[50]T. N. Do, L. Chen, A. K. Belyaev, H.-S. Tan, and M. F. Gelin, Chem. Phys. **515**, 119 (2018).
[51]A. O. Caldeira and A. J. Leggett, Physica A **121**, 587 (1983).